Doctor of Philosophy

FRICTION STIR WELDING OF METALS ALLOYS:

MICROSTRUCTURAL CHANGES RELATED TO

MECHANICAL PROPERTIES

The Graduate School of the University of Ulsan

School of Mechanical Engineering

Kun Gao

FRICTION STIR WELDING OF SIMILAR AND DISSIMILAR METALS ALLOYS: MICROSTRUCTURAL CHANGES RELATED TO MECHANICAL PROPERTIES

Advisor: **Professor Sung-Tae Hong**

A Dissertation

Submitted to the Graduate School of the University of Ulsan

in Partial Fulfillment of the Requirements

for the Degree of

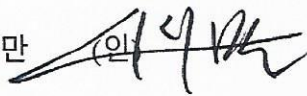Doctor of Philosophy

by

Kun Gao

School of Mechanical Engineering

University of Ulsan, Republic of Korea

June 2022

Kun Gao 의

공학박사 학위 논문을 인준함

심사위원 천두만   (인)

심사위원 홍성태   (인)

심사위원 지창욱   (인)

심사위원 정구현   (인)
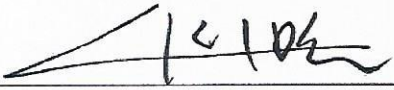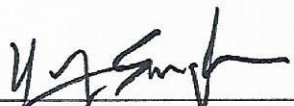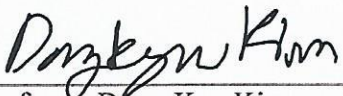
심사위원 김동규

울 산 대 학 교 대 학 원
기계자동차공학과
2022 년 6 월

FRICTION STIR WELDING OF SIMILAR AND DISSIMILAR METALS ALLOYS: MICROSTRUCTURAL CHANGES RELATED TO MECHANICAL PROPERTIES

The certifies that the dissertation of

Kun Gao is approved

Committee Chair	Professor Doo-Man Chun
Committee member	Professor Sung-Tae Hong
Committee member	Doctor Chang wook Ji
Committee member	Professor Koo-Hyun Chung
Committee member	Professor Dong-Kyu Kim

School of Mechanical Engineering

University of Ulsan, South Korea

June 2022

ABSTRACT

Lightweight alloys have attracted significant attention in the automotive industry to reduce environmental pollution and unnecessary energy waste. Among various lightweight materials, using aluminum (Al) alloys to replace steels is a popular way to achieve lightweight automobiles. Traditional fusion welding technologies, including resistance spot welding and gas tungsten arc welding, can induce various technical difficulties for welding Al alloys. Friction stir welding (FSW), which is a solid-state joining technology, can be considered as a promising substitute to replace the traditional fusion welding technologies. In this dissertation, the feasibility and effectiveness of friction stir spot welding (FSSW) on dissimilar metal materials are investigated. Besides, the effect of microstructure on the tensile properties and fatigue failure mechanism of FSW and friction stir lap welding (FSLW) of similar/dissimilar metal materials is studied.

Firstly, FSSW of dissimilar S45C steel and 6061-T6 aluminum alloy in a butt configuration is experimentally investigated. In this study, butt spot welding is performed using a convex scrolled shoulder tool at different tool rotational speeds. The microstructures of the joints without significant defects are characterized using scanning electron microscopy and energy dispersive spectrometry. Microstructural analysis shows the presence of intermetallic compounds (IMCs) along the steel/aluminum interface. The results of tensile tests show that the tensile strength of the joint increase with increasing the tool rotational speed. The tensile performance of joints is strongly affected by the IMCs at the joint interface, such as the thickness or type of IMCs.

Secondly, the microstructure, tensile properties, and fatigue behavior of FSW joints of multilayer AA3003-clad AA6013 are experimentally investigated. Linear butt welding is performed using a concave tool equipped with a columnar threaded pin at a rotating speed of 600 rpm and a transverse speed of 200 mm/min. The microstructures of FSW joints were

i

observed using a field emission scanning electron microscope equipped with an electron backscatter diffraction system and an energy dispersive spectrometer. The microstructural characterization in the stir zone (SZ) reveals grain refinement, precipitate refinement, zigzag line, and the AA3003-clad layer fragments due to material mixing. The tensile test result of all-weld joints shows that the tensile strength of the SZ is significantly higher than that of base metal, while the cross-weld joints show a typical ductile fracture in the base metal. The result of fatigue tests shows that all the cross-weld joints fracture from the SZ. Analysis of the fatigue failure mechanism indicates that the crack causing the fatigue fracture originates from the AA3003-clad layer fragments in the advancing side of the SZ.

Finally, the microstructural characteristics and mechanical properties of FSLW of Al-clad Al and Al-clad mild steel sheets are experimentally investigated. Optical microscopic observation confirms that the FSLW joints are successfully fabricated without noticeable joining defects, including cracks and hooks. The material flow is correlated with silicon (Si) element distribution in the stir zone (SZ). The tensile test result shows that all the FSLW joints fracture from the Al-clad Al sheet side. The fatigue test result shows that the fatigue life of the AS-loaded lap joint is lower than that of the RS-loaded lap joint. The tip of the non-bonding region on the AS, which is the fatigue failure initiation position of the AS-loaded lap joint, is located in the junction of the SZ and thermo-mechanically affected zone (TMAZ). The significant differences in the grain size and texture between the TMAZ and SZ are responsible for the poor fatigue performance of the AS-loaded lap joint. Besides, the higher dislocation value and smaller grain misorientation angle on the junction of SZ and TMAZ accelerate the degradation of fatigue performance. The fatigue failure of the RS-loaded lap joint occurs at the bottom of SZ due to the residual AA1050 layer cladded on the surface of the mild steel core.

ACKNOWLEDGMENTS

TABLE OF CONTENTS

LIST OF FIGURES

LIST OF TABLES

CHAPTER Ⅰ

INTRODUCTION

As a result of more stringent requirements for improved fuel economy and emissions, battery electric vehicles (BEVs) have obtained considerable attention. However, BEVs are unable to meet the demand for long-distance driving due to the low energy density of battery. Application of lightweight materials, such as carbon fiber reinforced polymer (CFRP), magnesium alloy, and aluminum alloy, is one basic approach to reduce the weight of BEVs. These lightweight materials have lower density, higher specific strength and specific stiffness, which can further reduce the weight of automobiles. However, due to the higher cost of CFRPs and poor plasticity of magnesium alloys, their large-scale application in the automotive industry is limited (Campbell, 2012). By contrast, Al alloys are preferences and widely used in the BEVs industry due to their cost-effectiveness, formability, and higher specific strength (Stojanovic *et al*. 2018). On the premise of guaranteeing automobile performance, there is a growing trend to completely or partially substitute aluminum alloys for conventional steel and cast irons.

Joining technology of lightweight materials, such as joining of Al alloys, joining of Al alloy and steel, plays an important role in modern BEVs manufacturing industry, since it is hardly conceivable to manufacture lightweight products without some sort of joining due to functional requirements and technological limitations. Generally, the related joining processes can be classified into two methods: conventional fusion welding and solid-state joining.

Conventional fusion welding methods, such as resistance spot welding (Qiu *et al*., 2010), tungsten inert gas brazing (Lin *et al*., 2009), and laser welding (Chen *et al*., 2011),

have been utilized to join lightweight materials. However, technical difficulties, including the formation of complex weld pool structures, inhomogeneous solidification microstructures, and segregation, hinder their practical applications. Therefore, in order to ensure the welding quality, it is necessary to strictly control the temperature and humidity of the workshop. Besides, debugging welding process parameters and correcting related processes greatly increase the manufacturing process and increase the manufacturing cost. A qualified lightweight material welder needs long-term training. The strong arc light and smoke in the welding process have great harm to workers.

Solid-state joining includes friction stir welding (FSW) and diffusion joining (pressure joining, forge joining, roll joining, friction joining, explosion joining) and so on. Solid-state diffusion joining processes generally use the same bonding mechanism of pressure joining, which generates joints by establishing diffusion bonding between metal surfaces under great pressure (Mohamed *et al*., 1975). However, metal surfaces are covered with oxide layers. In order to joining the metals by metallic bonding between two contacting surfaces, the covered oxide layer should be broken by applying great pressure. At the same time, the joining processes are accompanied by large deformation of metal, which greatly limit the metal joining of sheet metal with thin thickness [Mahabunphachai *et al*., 2009].

FSW is one kind of new solid-state welding technology invented by the British Welding Research Institute in 1991 (Thomas *et al*., 1991). FSW is a welding method that uses the friction heat generated by the shoulder of the stirring head and the metal surface and the deformation heat generated by the plastic deformation of the metal after being acted by the stirring pin as the heat source to realize the joining. Friction stir spot welding (FSSW), which originated from FSW, is a spot joining process and lateral movement of tool is not involved (Badarinarayan *et al*., 2009). The heat generated in FSW/FSSW process is much less than that of traditional welding. Therefore, the softening, deformation, and residual stress

2

of the welded joint can be effectively reduced. Also the welding efficiency and joint strength can be greatly improved. On the other hand, there is no need to use welding wire in the FSW/FSSW process. Therefore, FSW/FSSW can be considered as a kind of energy saving and environment-friendly joining technology.

Numerous research has been done in FSW/FSSW so far. The IMC layer associated with the FSSW process parameters such as tool rotational speed and weld offset is a significant issue. Therefore, it is of great significance to study the influence of IMCs on mechanical properties of the FSSW joint. Fereiduni *et al.* (2015) investigated that rotational speed and dwell time were related with the formation of IMCs during the FSSW of Al-5083 and St-12 alloy sheets. Coelho *et al.* (2012) reported 6181-T4 aluminum alloy was joined to dual-phase (DP) 600 and HC 260 LA, respectively. Bozzi *et al*. (2010) reported that the thickness of the IMC layer at the joint interface in FSSW of Aluminum alloy 6016 and interstitial free steel. Pourali *et al*. (2017) studied IMCs at friction stir welding joints of Al 1100 and St 37 steel plates. Piccini *et al*. (2017) studied the FSSW joints of aluminum alloy 5052 and LCS (Low Carbon Steel) joints. And they analyzed that the effect of tool geometry on the IMC layer evolution and failure load.

Elangovan *et al*. (2008) implemented the FSW of AA6061 aluminum alloy using five different tool pin profiles with three different shoulder diameters. Biswas *et al*. (2011) studied the effect of the geometry of the tool pin on the strength of the welded joints. They found that the FSW joint of aluminum alloys fabricated using the tool with tapered pins had superior mechanical properties. Kumar *et al.* (2020) explored the effect of transverse speed on friction stir welding of aluminum (AA6351-T6) sheets. Cavaliere *et al*. (2006) studied microstructural properties of AA6056 joints produced by FSW at different welding parameters, and they reported that the grain appeared fine and equiaxed in the nugget zone

due to dynamic recrystallization caused by the stirred action and the heat input of the rotating tool.

Watanabe et al. (2005) discussed the effect of changing the process parameters (such as the rotational, traverse speed, and the tool plunge depth) on the friction stir lap welding (FSLW) joint of Al alloys. The successful lap weld of a thin aluminum sheet with the thickness of 0.4 mm to a thin stainless steel sheet with the thickness of 0.2 mm was obtained by Yoshikawa *et al*. (2003). Wang *et al*. (2014) studied the effect of tool pin length on joint strength and indicated that the hook length on the AS exhibited an 'M' shaped pattern with increasing tool pin length. Yazdanian *et al*. (2012) analysed AS hooking characteristic at different spindle and weld speeds. Dubourg *et al*. (2010) also validated this while indicating that hook size reduced with decreased spindle /increased weld speed for FSLW of AA7075-T6 and AA2024-T3 alloys. Loading of a lap joint can be designed for either the top plate AS or the RS side to be loaded during testing and operations, the differing hook characteristics on AS and RS results in differences in joint strength for these two types of joint loadings.

It is well known that the microstructure characteristics are closely related to the mechanical properties of FSW joints. Thus, evaluation of the effect of microstructure characteristics on mechanical properties of FSW joints could provide a reference for further improvement of joint strength. Tensile strength and strain hardening behavior of the FSWed joints play a prominent part in the load bearing capacity of structure. Tan *et al*. (2017) carried out the FSW of AA 3003 aluminum alloy with different initial microstructures under different welding conditions, and they characterized the relationship between the yield strength and microstructure. Niu *et al*. (2018) reported strain hardening behavior and fracture mechanisms of FSW of Al-Cu alloy and Al-Zn and Al-Mg alloys, respectively. Ni *et al*. (2014) studied the work hardening behavior of base metals and FSW joints at different strain

rates; they reported that the finer grain contributed to enhance the strain hardening rate FSW joint.

Since under the cyclic stress or strain, local permanent damage of FSW joints occurs, accumulates, and fractures suddenly, it is important for the assessment of their fatigue performance and failure mechanism. Several investigations revealed that the fatigue strength of the FSW joint of aluminum alloys was higher compared with that of fusion welding, such as TIG welds (Wang et al., 2008) and MIG welds (Moreira et al., 2007). Salih *et al*. (2019) investigated the low-cycle fatigue properties of FSW joints and reported that the grain refinement in the welding nugget zone could significantly improve the fatigue life of the FSW joints. After the FSW of aluminum alloys, the oxide layer on the initial butt surface maintains in the welding zone, which results in the formation of the zigzag line. Di *et al*. (2007) reported that the effect of the zigzag line on the fatigue properties of the FSW of AA7075-T6. They considered that the zigzag line was detrimental to fatigue performance. Zhang *et al*. (2019) studied the transverse speed on the zigzag feature and mechanical properties of an FSWed Al-Zn-Mg aluminum alloy. They found that under the welding condition of a higher transverse speed of 300 mm/min, the formation of a relatively ambiguous zigzag line was not detrimental to mechanical performance. Besel *et al*. (2017) studied the local strain evolution under fatigue loading in a friction stir welded Al-Mg-Sc alloy. The results showed that the local plastic strain straining was the main cause of fatigue crack initiation.

In the present study, FSSW of steel and aluminum alloy (chapter II), FSW of AA3003-clad AA6013 thin sheets (chapter III) and FSLW of AA4343-clad AA6013 and AA1050-clad mild steel are experimentally investigated. Chapter II, III and Ⅳ are presented as two independent journal papers which have been published. In chapterII, the feasibility of FSSW of dissimilar S45C steel and 6061-T6 aluminum alloy in a butt configuration is

experimentally investigated. The cross-sectional microstructure of FSSW joints with optimized parameters was characterized by OM and SEM. The effect of IMCs along the steel/aluminum interface on the mechanical properties was analyzed. The tensile failure mechanism of FSSW joint was studied by observation of the cross section of fracture joint.

In chapter III, FSW of multilayer AA3003-clad AA6013 are experimentally investigated. The cross sectional microstructure of FSW joint was analyzed by OM, SEM, and EBSD. The tensile strength of the base metal, cross-weld joint, and all-weld joint was evaluated. The effect of zigzag line, surface roughness, and material mixing on the fatigue behavior was studied.

In chapter Ⅳ, FSLW of AA4343-clad AA3003 and AA1050-clad mild steel is experimentally investigated. In this study, the mechanical behaviors of FSLW joints were studied. The fatigue failure mode and tensile failure mode of AS-loaded joint and RS-loaded joint were analysed. The mechanical properties of FSLW is decided by the microstructure and morphology of FSLW.

Reference

Campbell, FC (2012) Introduction and uses of lightweight materials. Lightweight materials: understanding the basics, 4.

Stojanovic, B, Epler, I (2018) Application of aluminum and aluminum alloys in engineering. Applied Engineering Letters.

Qiu R, Shi H, Zhang K, Tu Y, Iwamoto C, Satonaka S (2010) Interfacial characterization of joint between mild steel and aluminum alloy welded by resistance spot welding. Materials Characterization 61(7): 684-688.

Lin SB, Song JL, Ma GC, Yang CL (2009) Dissimilar metals TIG welding-brazing of aluminium alloy to galvanized steel. Frontiers of Materials Science in China 3(1):78-83.

Chen HC, Pinkerton AJ, Li L, Liu Z, Mistry AT (2011) Gap-free fibre laser welding of Zn-coated steel on Al alloy for light-weight automotive applications. Materials & design 32(2):495-504.

Mohamed HA, Washburn J (1975) Mechanism of solid state pressure welding. Weld Journal 302-310.

Mahabunphachai S, Koc M, Ni J (2009) Pressure Welding of Thin Sheet Metals: Experimental Investigations and Analytical Modeling. Journal of Manufacturing Science and Engineering 131(4):1-9.

Thomas WM, Nicholas ED, Needham JC, Murch MG, Temple-Smith P, Dawes CJ. (1991) GB Patent application no.9125978.8[J]. International patent application no. PCT/GB92/02203.

Badarinarayan H, Yang Q, Zhu S (2009) Effect of tool geometry on static strength of friction stir spot-welded aluminum alloy. International Journal of Machine Tools and Manufacture 49:142-149.

Fereiduni E, Movahedi M, Kokabi AH (2015) Aluminum/steel joints made by an alternative friction stir spot welding process. Journal of material Processing Technology 224:1-10.

Coelho RS, Kostka A, Dos Santos JF, Kaysser-Pyzalla A (2012) Friction-stir dissimilar welding of aluminum alloy to high strength steels: mechanical properties and their relation to microstructure. Material Science and Engineering: A 556:175-183.

Bozzi S, Helbert-Etter AL, Baudin T, Criqui B, Kerbiguet JG (2010) Intermetallic compounds in Al 6016/IF-steel friction stir spot welds," Material Science and Engineering: A 527:4505-4509.

Pourali M, Abdollah-zadeh A, Saeid T, Kargar F (2017) Influence of welding parameters on intermetallic compounds formation in dissimilar steel/aluminum friction stir welds. Journal of Alloys and compounds 715:1-8.

Piccini M, Svoboda G, Tool geometry optimization in friction stir spot welding of Al-steel joints. Journal of Manufacturing Processes 26:142-154.

Elangovan K, Balasubramaniam V (2008) Influences of tool pin profile and tool shoulder diameter on the formation of friction stir processing zone in AA6061 aluminium alloy. Materials and Design 29:362-373.

Biswas P, Kumar DA, Mandal NR (2011) Friction stir welding of aluminum alloy with varying tool geometry and process parameters. SAGE Journals 226:641-648.

Kumar P, Kumar R, Hembram BK, Murugan M, Arif A, Veerababu, M (2020) Study of microstructure and mechanical properties of aluminum alloy (AA-6351-T6) using friction stir welding. Materials today: Proceedings 27:1733-1737.

Cavaliere P, Campanile G, Panella F, Squillacec A (2006) Effect of welding parameters on mechanical and microstructural properties of AA6056 joints produced by Friction Stir Welding Author links open overlay panel, Journal of Materials Processing Technology. 180: 263-270.

Kimapong K, Watanabe T (2005) Effect of Welding Process Parameters on Mechanical Property of FSW Lap Joint between Aluminum Alloy and Steel. Materials transactions 46(10):2211-2217.

Yoshikawa Y, Harano T (2003) Numerically Controlled Friction Stir Welding in Layered Dissimilar Metal Materials of Aluminum and Steel, Proceedings of the 43rd International Symposium on Friction Stir Welding, Park City, Utah, May 14–16,

Wang M, Zhang H, Zhang J, Zhang X, Yang L (2014) Effect of pin length on hook size and joint properties in friction stir lap welding of 7B04 aluminum alloy. Journal of materials engineering and performance 23(5):1881-6.

Yazdanian S, Chen Z, Littlefair G (2012) Effects of friction stir lap welding parameters on weld features on advancing side and fracture strength of AA6060-T5 welds. Journal of materials science 47(3):1251-1261.

Dubourg L, Merati A, Jahazi M (2010) Process optimisation and mechanical properties of friction stir lap welds of 7075-T6 stringers on 2024-T3 skin. Materials & Design 31(7):3324-3330.

Tan YB, Wang XM, Ma M, Zhang JX, Liu WC, Fu RD, Xiang S (2017) A study on microstructure and mechanical properties of AA 3003 aluminum alloy joints by underwater friction stir welding, Materials Characterization 127:41-52

Niu PL, Li WY, Chen DL (2018) Strain hardening behavior and mechanisms of friction stir welded dissimilar joints of aluminum alloys, Materials Letters 231:68-71.

Ni DR, Chen DL, Wang D, Xiao BL, Ma ZY (2014) Tensile properties and strain-hardening behaviour of friction stir welded SiCp/AA2009 composite joints, Materials Science and Engineering: A 608:1-10

Wang X, Wang K, Shen Y, Hu K (2008) Comparison of fatigue property between friction stir and TIG welds, Journal of University of Science and Technology Beijing, 15(3):280-284.

Moreira PMGP, de Figueiredo MAV, de Castro PMST (2017) Fatigue behaviour of FSW and MIG weldments for two aluminium alloys. Theoretical and Applied Fracture Mechanics, 48:169-177.

Salih OS, Ou H, Wei X, Sun W (2019) Microstructure and mechanical properties of friction stir welded AA6092/SiC metal matrix composite. Materials Science and Engineering: A 742:78-88.

Di S, Yang X, Fang D, Luan G (2007) The influence of zigzag-curve defect on the fatigue properties of friction stir welds in 7075-T6 Al alloy. Materials Chemistry and Physics 104:244-248

Zhang H, Luo S, Xu W (2019) Influence of Welding Speed on Zigzag Line Feature and Tensile Property of a Friction-Stir-Welded Al-Zn-Mg Aluminum Alloy. Journal of Materials Engineering and Performance 28:1790-1800.

Besel Y, Besel M, Mercado UA, Kakiuchi T, Hirata T, Uematsu Y (2017) Influence of local fatigue damage evolution on crack initiation behavior in a friction stir welded Al-Mg-Sc alloy. International Journal of Fatigue 99(1):151-162.

CHAPTER Ⅱ

FRICTION STIR SPOT BUTT WELDING OF DISSIMILAR S45C STEEL AND 6061-T6 ALUMINUM ALLOY

ABSTRACT:

Friction stir spot welding (FSSW) of dissimilar S45C steel and 6061-T6 aluminum alloy in a butt configuration is experimentally investigated. Butt spot welding is performed using a convex scrolled shoulder tool at different tool rotational speeds. FSSW butt joints are successfully fabricated by offsetting the tool to the steel side. The microstructures of the joints fabricated at three different tool rotational speeds are characterized using scanning electron microscopy and energy dispersive spectrometry. Microstructural analysis shows the presence of intermetallic compounds (IMCs) along the steel/aluminum interface. The thickness of the IMC layer and the tensile strength of the joint increase with increasing the tool rotational speed. The results of tensile tests and microstructural analysis show that the joint performance is closely related with the IMCs at the joint interface.

Keywords: Friction stir spot butt welding; aluminum alloy; steel; dissimilar joint; intermetallic compounds

2.1 Introduction

Incorporation of lightweight materials for manufacturing various automotive components has been increasing to meet regulations of less emissions and better fuel efficiency, while simultaneously resolving safety issues (Cole *et al*., 1995). Among various lightweight materials, aluminum alloys are widely used for their formability and cost-effectiveness (Schubert *et al*., 2001). Although aluminum alloys provide various advantages, they are not able to replace steels completely. In many industrial applications, it is very difficult or nearly impossible for lightweight aluminum alloys alone to fulfill imposed structural or mechanical requirements. As a result, steels, which have superior mechanical properties and cheaper prices than aluminum alloys, still have wide applications in the automobile, aerospace, and railway industries. Therefore, to achieve weight reduction while satisfying the structural or mechanical requirements, the joining of dissimilar steel and aluminum alloys is unavoidable in many industrial applications (Hussein *et al*., 2015).

However, the joining of these two alloys imposes complications due to the vast differences in their thermo-mechanical properties and their tendency to form brittle intermetallic compounds (IMCs) (Liu *et al*., 2014). Researchers have attempted to join steels and aluminum alloys using two different joining methods: conventional fusion welding and solid-state joining. Conventional fusion welding methods, such as resistance spot welding (Qiu *et al*., 2010), tungsten inert gas brazing (Lin *et al*., 2009), and laser welding (Chen *et al*., 2011), have been utilized to join steels and aluminum alloys. However, technical difficulties, including the formation of complex weld pool structures, inhomogeneous solidification microstructures, and segregation, hinder their practical applications. Also, most conventional fusing welding techniques involve relatively high heat input, resulting in the formation of a thick layer of brittle IMCs (Liu *et al*., 2014; Peyre *et al*., 2007; Mathieu *et al*., 2007). Since fatigue cracks generally originate inside the brittle IMC layer, researchers have recommended

limiting the thickness of the IMC layer to less than 10 μm to achieve mechanically sound joints (Arghavani *et al*., 2016; Chen et al., 2017; Miyamoto *et al*., 2009).

In contrast, solid-state joining methods, such as explosion welding, friction welding, brazing, and electrically assisted pressure joining, avoid melting of the alloys and thereby avert most solidification defects (Mustafa *et al*., 2008; Xue *et al*., 2018; Meshram *et al*., 2007; Zhang *et al*., 2021). Nevertheless, due to the need for high pressure to induce large deformation of materials and also to comply with safety restrictions, explosion welding (Findik 2011) and friction welding (Meshram *et al*., 2007) are generally limited to welding components made of highly ductile materials with simple shapes. Electrically assisted pressure joining products joints by establishing diffusion bonding under the joining conditions of plastic deformation and elevated temperature, which is generally necessary to extend the longer diffusion time to enhance the bonding strength (Zhang *et al*., 2021). With respect to brazing, the solidification process of melted filler may lead to porosity and slag inclusions in the interlayer (Milani *et al*., 2016; Niu *et al*., 2016).

Friction stir welding (FSW), which is a solid-state joining technology (Thomas *et al*., 1991), uses a rotating tool that contacts the workpiece and generates frictional heat to plasticize the material. The rotating tool establishes material flow to accomplish the joining. FSW is generally used to produce butt or lap joints along the length of the workpieces. However, depending on the geometry of a complex target structure, spot welding (friction stir spot welding, FSSW) in a butt configuration can be more effectively used since traverse motion of the tool is not required in spot welding.

In FSW or FSSW of aluminum alloy and steel in a butt configuration, due to the drastically different mechanical and thermo-mechanical properties of the joining materials, the joining process is usually conducted with an offset to the aluminum alloy side or the steel side. In other words, the initial contact point of the pin of the rotation tool is not at the joining

line of the butt configuration. Therefore, in addition to conventional process parameters such as tool rotational speed, welding speed, plunge depth, and tilt angle, the tool offset can also profoundly affect the quality of aluminum/steel joints in FSW/FSSW butt joining (Wang *et al*., 2018). Watanabe *et al*. (2006) studied the influence of tool offset on joint strength of SS400 mild steel and 5083 aluminum alloy, and obtained the highest joining strength by offsetting the tool to by 0.2 mm toward the steel sheet side. In a study by Kimapong and Watanabe (2005), increasing the temperature of the steel by offsetting the tool to the steel side increased the atomic diffusion in the interface of the aluminum/steel to form the IMC layer.

In FSW/FSSW butt joining, the formation of the IMC layer can significantly affect the performance of the joint. Fereiduni *et al*. (2015) reported that the tool rotational speed and dwell time influenced the formation of IMCs during the FSSW of 5083 aluminum and St-12 alloy sheets, and they obtained the maximum tensile strength with the formation of a 2.3-μm-thick IMC layer. Coelho *et al*. (2012) studied the joining of 6181-T4 aluminum alloy to DP600 and HC260LA high-strength steels; they found that heat input and high shear strain played a crucial role in the formation of IMCs. Bozzi *et al*. (2010) reported that the critical thickness of the IMC layer at the FSSWed joint interface of 6016 aluminum alloy and interstitial free steel influenced the shear strength of the joint. Pourali *et al*. (2017) studied IMCs in FSW of 1100 aluminum alloy and St-37 steel plates. They concluded that Fe-rich IMCs with a certain thickness, like FeAl and Fe_3Al, were not detrimental to the shear strength of the joint. Piccini *et al*. (2017) studied the effect of tool geometry on the IMC layer evolution during FSSW of 5052 aluminum alloy and low-carbon steel.

Previous works related to the FSW of aluminum alloy and steel generally reported on linear welding at the butt or lap position and spot welding (FSSW) at the overlapped position. To our knowledge, research works to date have rarely reported on FSSW of aluminum alloy

and steel in a butt configuration. Therefore, based on the specific need for the manufacture of bimaterial automotive components, the FSSW of aluminum alloy and steel in a butt configuration is studied here.

2.2 Experimental set-up

Commercially available S45C steel and 6061-T6 aluminum alloy (AA6061-T6) sheets were selected as the subject materials of the present study (chemical compositions in Table 2.1). These materials were cut to a cuboid shape with dimensions (in mm) of 100 (length) $\times$ 40 (width) $\times$ 2 (thickness), and were used as base materials (BMs) for the proposed butt FSSW.

Table 2.1 Chemical compositions of AA6061-T6 and S45C steel (alloy elements, wt%)

Alloy elements	C	P	S	Al	Si	Mn	Fe	Mg	Cu	Cr	Zn
S45C	0.04	0.01	0.003	0.02	0.002	0.15	Bal.	-	-	-	-
AA6061-T6	-	-	-	Bal.	0.6	0.11	0.4	0.9	0.23	0.17	0.04

Prior to joining, the BMs were carefully ground and thoroughly degreased with ethanol and acetone. A custom-made FSW machine (RM1A; Bond Technologies, Elkhart, IN, USA) was used to perform FSSW using a spark plasma sintered tungsten carbide (WC) tool (tool geometry in Table 2.2) on the designated materials in a butt configuration, as depicted in Figures 2.1(a) and (b). As described in (Jeon *et al*., 2012; Yuan *et al*., 2011), alterations of the tool rotational speed and the tool offset significantly influence the material flow and formation of IMCs between the steel and aluminum alloy by varying the heat input and straining of materials during joining. Therefore, the FSSW was performed here by varying these two process parameters (in Table 2.3), while other parameters, including feed rate, depth of penetration, and dwell time, were kept constant.

After FSSW, the quality of the joints was first visually inspected. Subsequently, the weld spots were cut through the joint center (red dotted line in Figure 2.1(b)), and were ground and polished for microstructural observation by optical microscopy (OM) (A1M Axio Imager; Carl Zeiss, Göttingen, Germany). The cross sections of the joints were also examined using a field emission scanning electron microscope (FE-SEM) (SU-70; Hitachi, Tokyo,

Japan) equipped with an energy dispersive spectrometer (EDS) (X-Max50; Horiba, Kyoto, Japan).

Table 2.2 Geometry of the FSW tool

Tool geometry	Dimension
Shoulder diameter (mm)	14.3 mm
Pin height (mm)	0.6 mm
Pin diameter (mm)	2.0 mm
Shoulder type	Convex scrolled shoulder
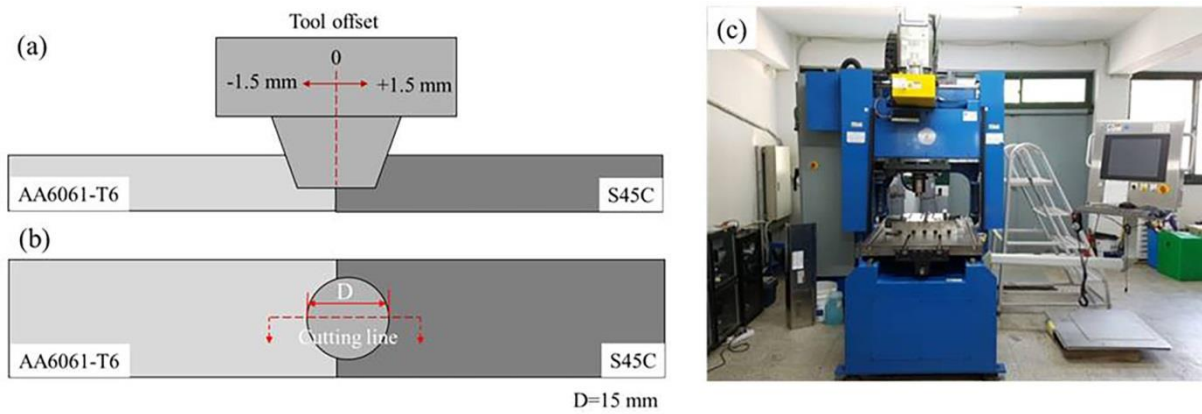
Figure 2.1 Schematics of specimen configuration: (a) side and (b) top views; (c) FSSW machine

Table 2.3 Process parameters for FSSW of AA6061-T6 and S45C steel

No.	Penetration depth (mm)	Dwell Time (s)	Feed rate (mm/min)	Tool offset	Rotational speed (rpm)
1					1400
2				-1.5 mm	1550
3					1700
4					1400
5	1.7	3	10	0	1550
6					1700
7					1400
8				+1.5 mm	1550
9					1700
10					1850

The FSSWed specimens were commonly notched at both sides, as the welding was performed at the butt position. To avoid the stress concentration by the notch effect during quasi-static tensile testing to evaluate the mechanical properties of the joints, the FSSWed joints were machined to the dimensions of (in mm) 120 (length) $\times$ 10 (width) $\times$ 2 (thickness) before tensile testing, as shown in Figure 2.2. The tensile strength of each joint was evaluated by using a universal testing machine with a constant displacement rate of 0.5 mm/min. Fracture surfaces of the tensile-tested joint specimens were investigated by SEM and were also detailed with EDS elemental analysis.
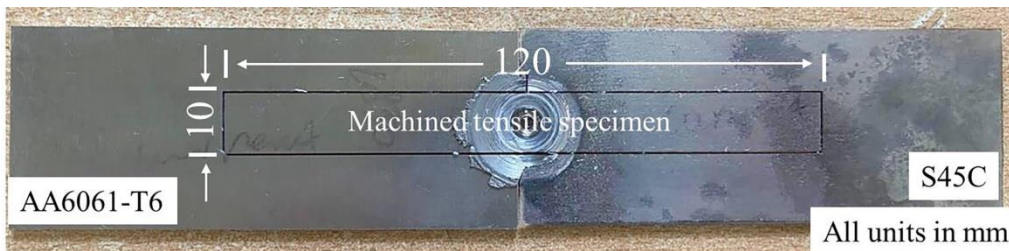
Figure 2.2 Dimensions for a tensile specimen from a butt FSSW joint

2.3 Results and discussion

The appearance (top view) of the FSSWed dissimilar joints of S45C steel and AA6061-T6 with different process parameters is shown in Figure 2.3. As summarized in Table 4, visual inspection of the joints confirmed that the tool position and tool rotational speed affected the shape and appearance of the weld surfaces.

When the tool was offset by 1.5 mm toward the AA6061-T6 side, evident defects, including surface cracks and partial fusion, were observed, as shown in Figures 2(a)-(c). At relatively low tool rotational speeds (1,400 rpm and 1,550 rpm) the AA6061-T6 was fused, which suggests that excessive heat was applied to the aluminum alloy during FSSW. Naturally, with increasing the tool rotational speed to 1,700 rpm (Figure 2.3(b)), partial melting of the AA6061-T6 was aggravated.

Next, the tool position was shifted to the center of the weld between the S45C steel and the AA6061-T6 to diminish the excessive heating of the aluminum alloy. Unfortunately, the final results (Figures 2.3(d)-(f)) were similar to those when the tool was offset to the AA6061-T6 side. Crack defects were still observed near the AA6061-T6/S45C joint interface. However, reducing the heat input to the aluminum alloy by shifting the tool position to the center of the weld certainly diminished the tendency of the AA6061-T6 to partially melt, as clearly shown in comparison to the results with the relatively low tool rotational speed of 1,400 rpm (Figures 2.3(a) and (d)). This suggests that properly distributing the heat input to the AA6061-T6 and the S45C steel by adjusting the tool offset can be helpful to prevent fusion defects in the joint.

Based on the trends observed in the experimental results shown in Figures 2.3(a)-(f), the tool position was further offset (1.5 mm) to the S45C steel side. At the relatively low tool rotational speed of 1,400 rpm (Figure 2.3(g)), obvious crack defects occurred at the interface between the S45C steel and the AA6061-T6 due to the insufficient heat input. However, with

this tool offset position, it was encouraging that the quality of the surface morphology improved (i.e., the crack defects disappeared) by increasing the tool rotational speeds to 1,550, 1,700, and 1,850 rpm without the occurrence of fusion defects, as presented in Figures 2.3(h)-(j). This shows that for the given material combination of S45C steel and the AA6061-T6, offsetting the tool to the steel side was beneficial to produce a sound joint without surface cracks and fusion defects. By offsetting the tool to the steel side, more heat input could be applied to the steel without inducing fusion defects in the aluminum side.
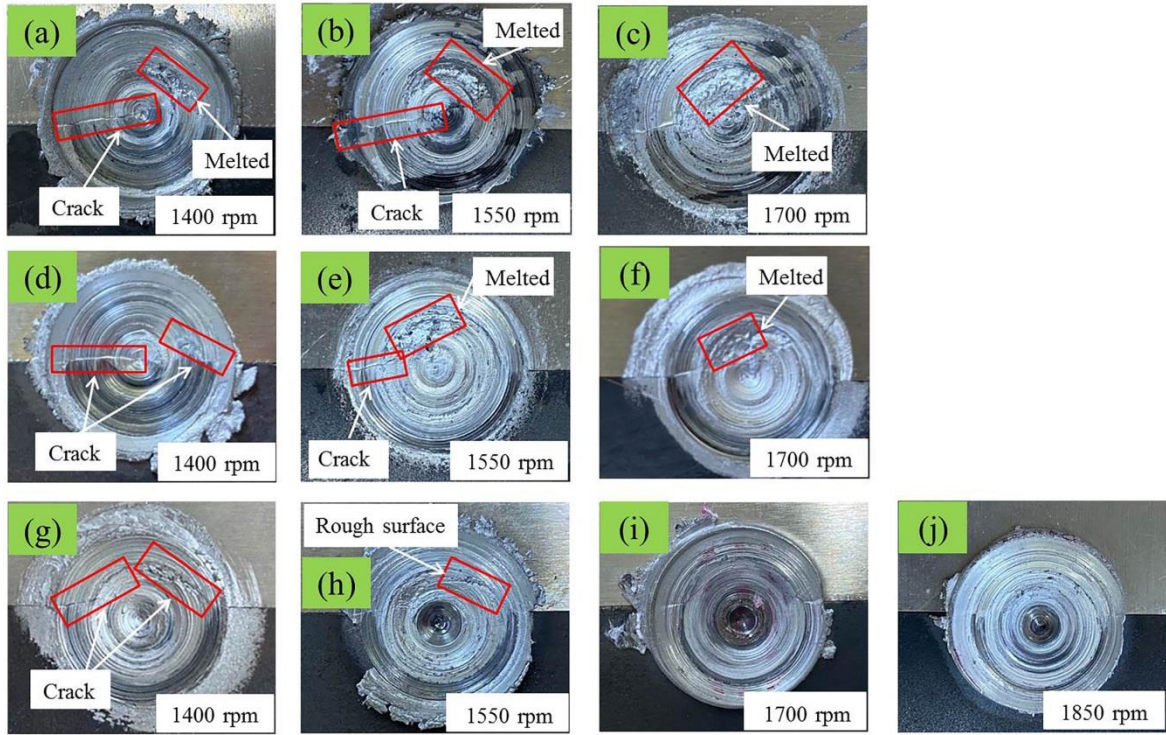
Figure 2.3 FSSW joints: (a-c) tool offset 1.5 mm toward the AA6061-T6 side, (d-f) no offset,

and (g-j) tool offset 1.5 mm toward the S45C steel side

Table 2.4 Observations of the weld surfaces under different parameter combinations

No.	Tool offset	Tool rotational speed (rpm)	Weld quality
1		1400	Defective & melted
2	1.5 mm toward Al side	1550	melted
3		1700	melted
4		1400	Defective & melted
5	0	1550	Defective & melted
6		1700	Melted
7		1400	Defective
8	+1.5 mm toward steel side	1550	Good
9		1700	Good
10		1850	Good

The FSSWed joints without cracks or fusion defects on the surface (Figures 2.3(h)-(j)) were further subjected to microstructural analysis. No significant difference in the OM results (Figure 2.4) was observed among the cross sections of the joints made with three different FSSW parameter combinations except that the FSSW joint developed crack defects during welding at 1,550 rpm (Figure 2.5(a)), but no significant defects were observed at the rotational speeds of 1,700 rpm and 1,850 rpm, as shown in Figures 2.5(b) and (c), respectively.
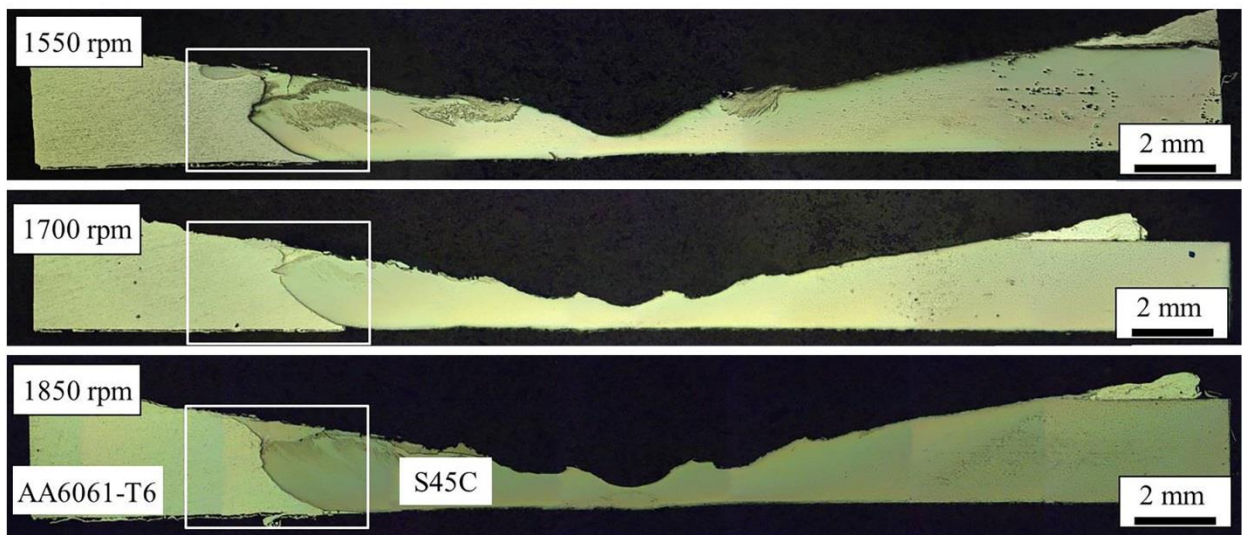
Figure 2.4 Optical macrographs of the weld cross-sections at three different tool rotational

speeds (tool offset 1.5 mm toward the S45C steel side)
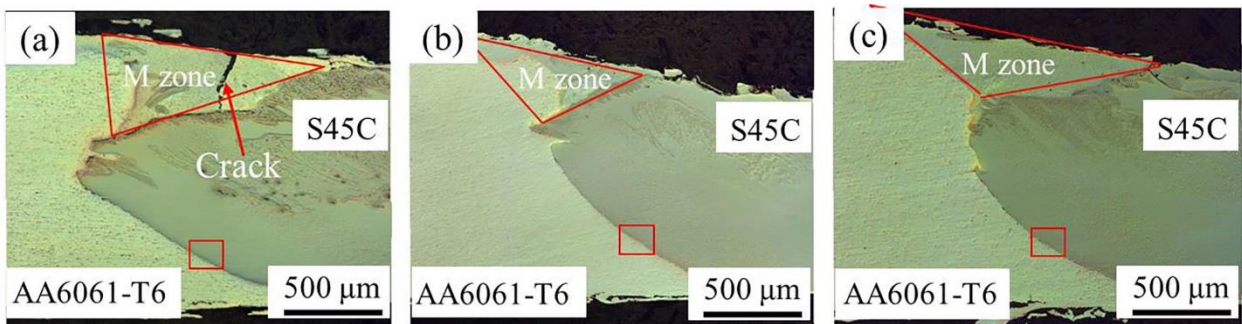
Figure 2.5 Magnified views of the regions marked by a white rectangle in Figure 4: (a) 1,550

rpm, (b) 1,700 rpm, and (c) 1,850 rpm

The regions marked with the red triangles (M zones = mixed zones) in Figures 2.5(a)-

(c) exhibit a slightly different color compared with the S45C steel and AA6061-T6. The

typical SEM image (Figure 2.6(a)) and the results of the EDS area scan (Figures 2.6(b) and

(c)) suggest that the M zones were a mixture of aluminum alloy (green color) and steel

particles (blue color). This suggests that the plasticized aluminum alloy and numerous steel

fragments peeled from the base metal were mechanically mixed into the M zone by the

rotating tool. Further detailed characterization was carried out to observe the interdiffusion of Al and Fe between the AA6061-T6 and the S45C steel at the joint interface.
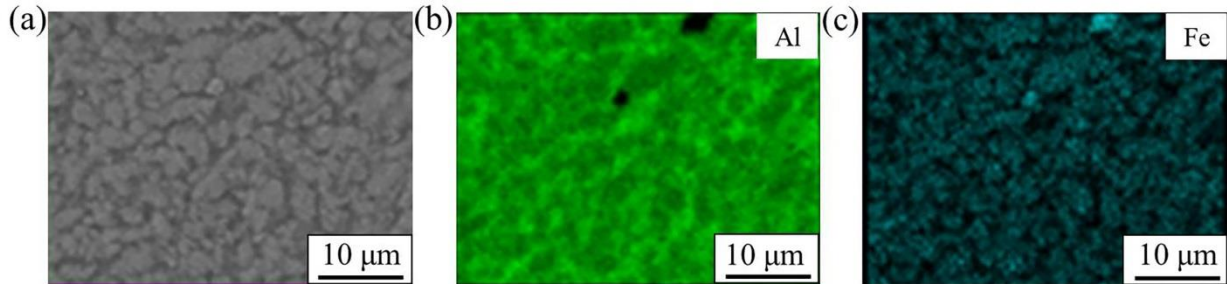
Figure 2.6 From Figure 5(c): (a) SEM image of M zone, (b) Al distribution, and (c) Fe distribution

As shown in Figures 2.4 and 2.5, an obvious boundary between the AA6061-T6 and the S45C steel was observed (except for the M zone at the top of the joint) for all three of the FSSW parameter combinations. The SEM results at the interface of the joints revealed a distinct layer with different colors between the S45C steel (bright region) and the AA6061-T6 (dark region) that was produced during welding at 1,550 rpm (Figures 2.7(a) and (b)), 1,700 rpm (Figures 2.8(a) and (b)), and 1,850 rpm (Figures 2.9(a) and (b)).

The results of the EDS elemental line scan (Figures 2.7(c), 2.8(c), and 2.9(c)) confirmed that the layers were composed of Al and Fe elements, which can be regarded as Al/Fe IMCs. Previous researches have suggested that atomic diffusion across the joint interface causes the formation of Al/Fe IMCs (Zhang *et al*., 2021; Fereiduni *et al*., 2015). Further, in the present study, steel particles were observed at the Al side, as clearly shown in Figures 2.8(b) and 2.9(b). Those steel particles could have been the result of the detachment of steel fragments from the steel edges by high shear stress caused by the severe stirring motion of the tool at higher rotational speeds (Zandsalimi *et al*., 2018).

24

According to the Al-Fe phase diagram (Sina *et al*., 2015) and analysis of the EDS elemental compositions (in Table 2.5), the possible IMCs at the three different welding conditions can be deduced. As summarized in Table 2.5, the IMC layers in Figures 2.8(b) and 2.9(b) may have consisted of FeAl (Fe-rich IMCs) and $FeAl_3$ (Al-rich IMCs). In contrast, at the relatively lower rotational speed of 1,550 rpm (Figure 2.7(b)), the IMC layer mainly included $FeAl_3$ and Fe_2Al_5 (Al-rich IMCs). With the increase of tool rotational speed, more Fe-rich IMCs (FeAl) were formed at the joint interface, which is not detrimental to the joint strength compared with Al-rich IMCs (Pourali *et al*., 2017).

The thickness of the IMC layer was approximated by the distribution of the major alloying elements across the interface through the EDS line scan, as shown in Figures 2.7(c), 2.8(c), and 2.9(c). With increasing the rotational speed from 1,550 rpm to 1,850 rpm, a significant increase in the IMC layer thickness (from 2.7 to 4.6 µm) was observed. That indicates that a sufficient energy input can promote the formation and growth of an Al/Fe IMC at the joint interface (Fereiduni *et al*., 2015; Sundman *et al*., 2009). Still, in all of the FSSW conditions, the IMC layers formed at the joint interfaces were very thin.
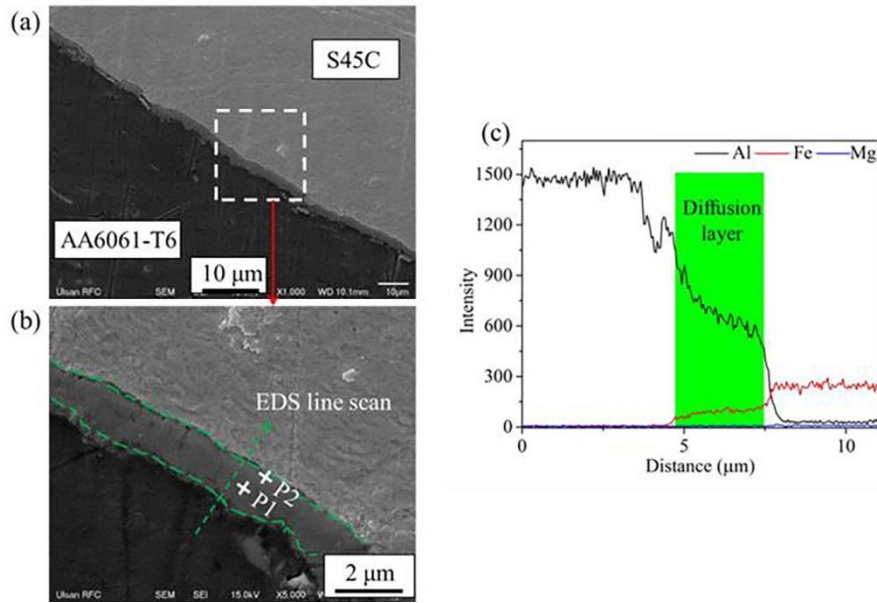
Figure 2.7 (a) SEM image of the region marked by a red rectangle in Figure 2.5(a), (b) magnified SEM image of the joint interface (a white rectangle in Figure 2.7(a)), and (c) elemental line scan across the joint interface
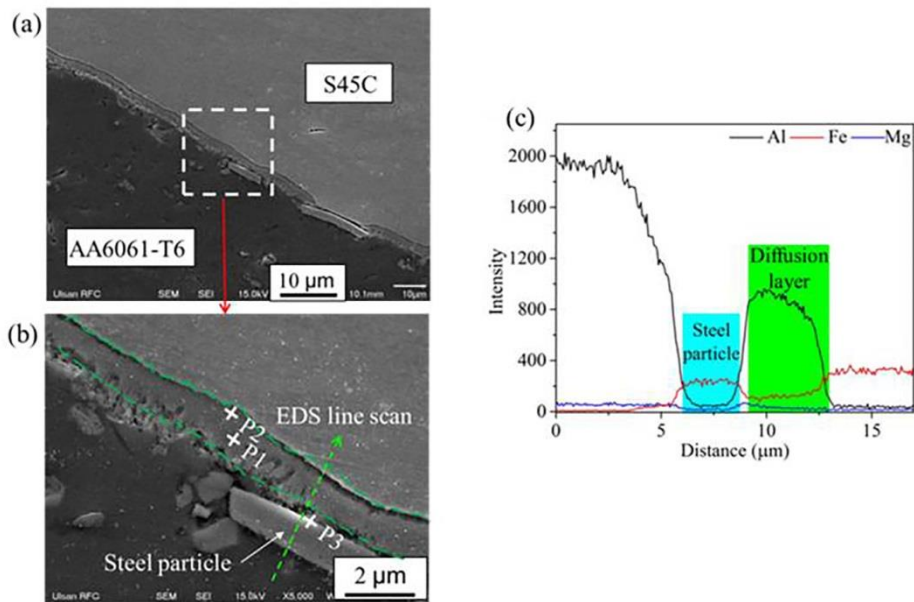
Figure 2.8 (a) SEM image of the region marked by a red rectangle in Figure 2.5(b), (b) magnified SEM image of the joint interface (a white rectangle in Figure 2.8(a)), and (c) elemental line scan across the joint interface
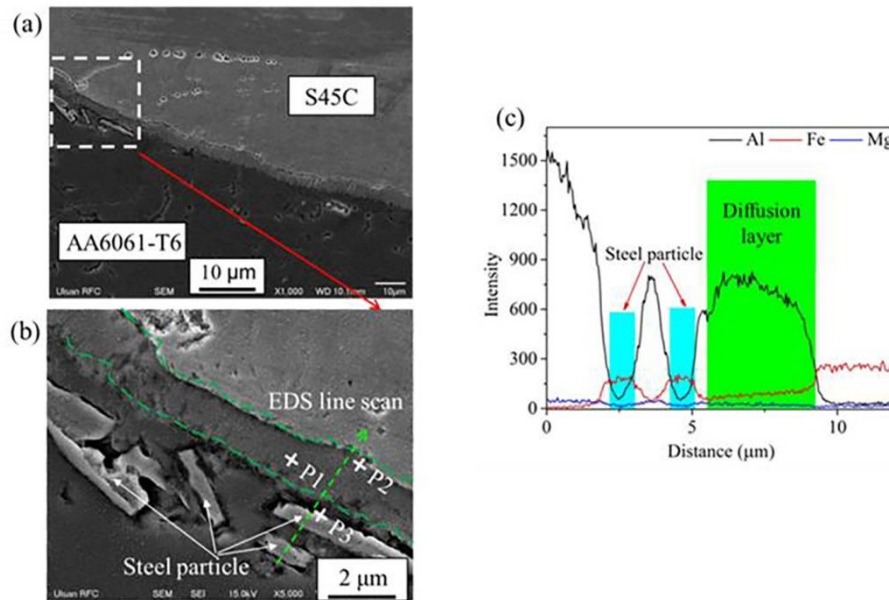
Figure 2.9 (a) SEM image of the region marked by a red rectangle in Figure 2.5(c), (b) magnified SEM image of the joint interface (a white rectangle in Figure 2.9(a)), and (c) elemental line scan across the joint interface

Table 2.5 Chemical compositions of IMC and possible phases in Figures 2.7-2.9

Tool rotational speed (rpm)	Location	Composition (at.%)			Possible phases	IMC layer thickness (μm)*
		Al	Fe	Mg		
1550	P1	74.46	23.91	1.63	$FeAl_3$	2.7 ($\pm$0.8)
	P2	69.68	29.46	0.86	Fe_2Al_5	
1700	P1	72.75	25.29	1.96	$FeAl_3$	3.3 ($\pm$1.0)
	P2	50.28	49.28	0.44	FeAl	
	P3	48.43	50.28	1.29	FeAl	
1850	P1	72.90	26.07	1.03	$FeAl_3$	4.1 ($\pm$2.0)
	P2	49.75	48.57	1.68	FeAl	
	P3	46.25	52.67	1.08	FeAl	

*Average value at three different locations

Studies have shown that a thin IMC layer (less than 10 μm (Arghavani *et al*., 2016; Miyamoto *et al*., 2009) might not be detrimental to the mechanical properties of joints [Chen *et al*., 2017; Fereiduni *et al*., 2015]. Here, the fractures in all of the FSSWed joints occurred

at the joining interface between the S45C steel and the AA6061-T6 after the tensile test (Figure 2.10(b)). As shown in the results of tensile tests (Figure 2.11), the maximum tensile strength of the FSSWed joints (2,830 $\pm$ 150 N) was obtained under the welding conditions of 1,850 rpm. Note that the IMC layer of the FSSWed joint created at the rotational speed of 1,850 rpm was extremely thin (approximately 4.4 μm maximum thickness) compared with that of conventional fusion welding.
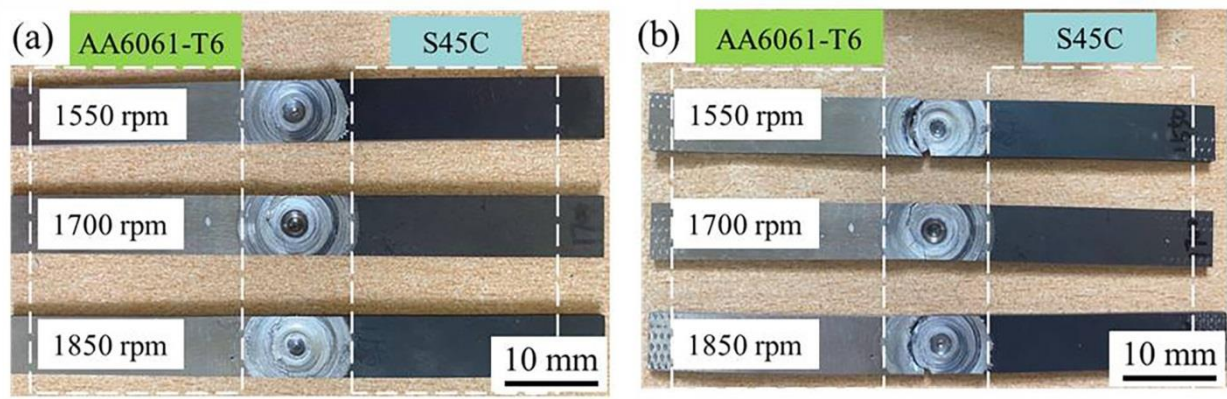
Figure 2.10 (a) Machined joint specimens and (b) tensile fractured specimens
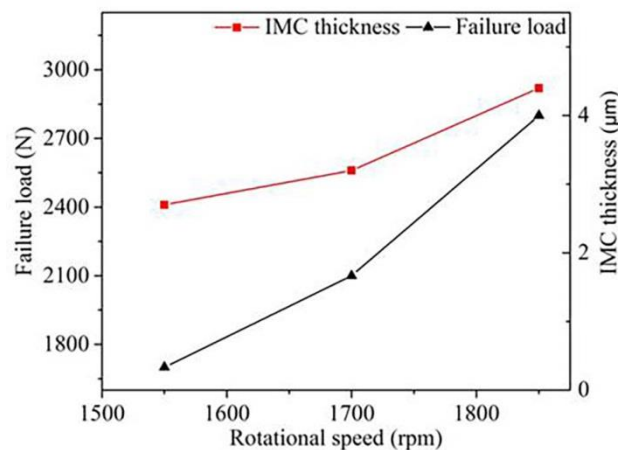
Figure 2.11 Thickness of IMC and joint failure load as functions of tool rotational speed

The IMC layer and the failure load simultaneously increased with the increase of the tool rotational speed, as presented in Figure 2.11. The correlation of the tensile strength of the

joint and the thickness of the IMC layer in Figure 2.11 confirms that in a certain range of thickness, a thicker IMC layer seems to improve the strength of the joint (Fereiduni *et al*., 2015; Tanaka *et al*., 2015). Bozzi *et al*. (2010) agreed with this view that an IMC layer may be necessary to improve the FSSWed weld strength of aluminum alloy and steel joints. Here, fracture during tensile tests occurred along the interface of the S45C steel and the AA6061-T6, and crossed over the M zone of the steel and the aluminum for all the FSSW joints (Figure 2.12(a)). Figure 2.12(b) shows that the thickness of the remaining IMC layer on the AA6061-T6 side was approximately 2 μm; in contrast, the fracture surface at S45C steel side showed almost no remaining IMC, as shown in Figure 2.12(c). To summarize, the tensile fracture failure of FSSWed joints mainly occurred in the top Al/Fe mixing zone and in the interface between the S45C steel and the IMC layer.
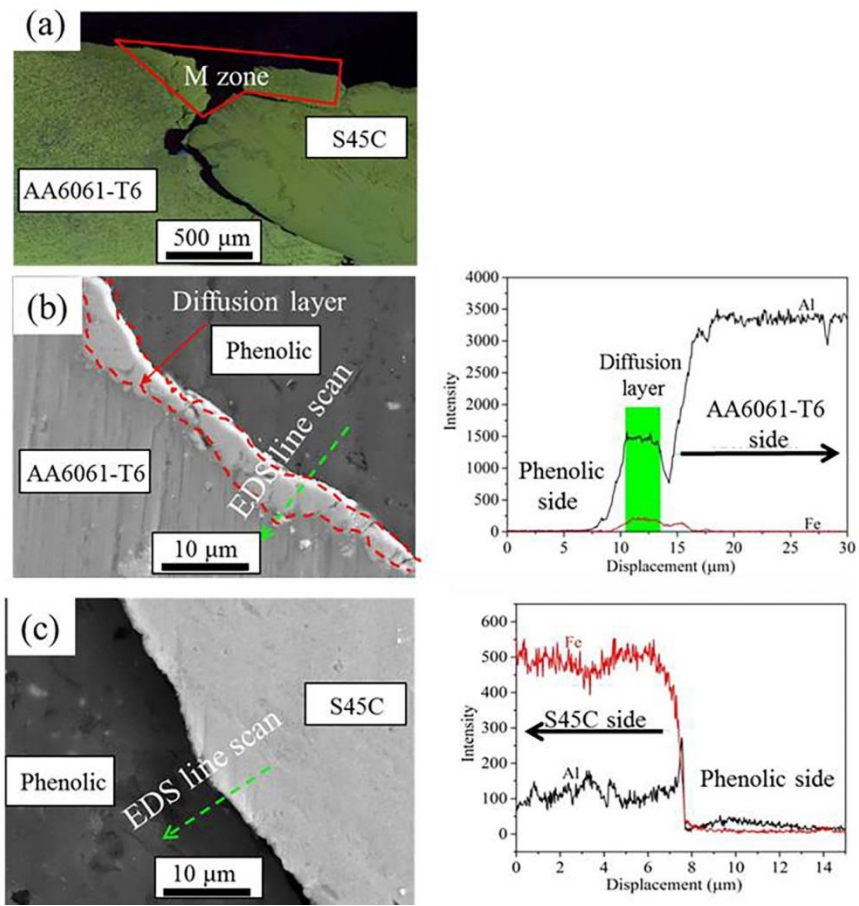
Figure 2.12 (a) A cross-sectional image of FSSW joints after tensile test (the tool rotational speed of 1550 rpm); SEM images and elemental line scans at (b) AA6061-T6 side (c) S45C side

2.4 Conclusion

In the present work, FSSW of S45C steel and 6061-T6 aluminum alloy was conducted with different tool rotational speeds and tool positions. The experimental results showed that the FSSWed butt joints of the dissimilar steel and the aluminum alloy were successfully fabricated by offsetting the tool by 1.5 mm toward the steel side. Microstructure analysis using SEM-EDS showed that an IMC layer was formed, and three possible IMCs (FeAl, FeAl$_3$, and Fe$_2$Al$_5$) were identified at the joint interface. Increasing the tool rotational speed increased the thickness of the IMC layer. The results of point and line analysis suggested that a thicker IMC layer and Fe-rich IMCs seemed to be beneficial to improve the strength of the FSSW joints. The quasi-static tensile tests showed that fractures occurred along the joint interface and in the top Al/Fe mixing zone.

References

Cole GS, Sherman AM (1995) Light weight materials for automotive applications. Materials characterization 35(1): 3-9.

Schubert E, Klassen M, Zerner I, Walz C, Sepold G (2001) Light-weight structures produced by laser beam joining for future applications in automobile and aerospace industry. Journal of Materials Processing Technology 115(1):2-8.

Hussein SA, Tahir ASM, Hadzley AB (2015) Characteristics of Aluminum-to-Steel Joint Made by Friction Stir Welding: A review. Materials Today Communications 5:32-49.

Liu X, Lan SH, Ni J (2014) Analysis of process parameters effects on friction stir welding of dissimilar aluminum alloy to advanced high strength steel. Materials and Design 59:50-62.

Qiu R, Shi H, Zhang K, Tu Y, Iwamoto C, Satonaka S (2010) Interfacial characterization of joint between mild steel and aluminum alloy welded by resistance spot welding. Materials characterization 61:684-688.

Lin SB, Song JL, Ma GC, Yang CL (2009) Dissimilar metals TIG welding-brazing of aluminium alloy to galvanized steel. Frontiers of Materials Science in China 3(1):78-83.

Chen HC, Pinkerton AJ, Li L, Liu Z, Mistry AT (2011) Gap-free fibre laser welding of Zn-coated steel on Al alloy for light-weight automotive applications. Materials and Design 32(2):495-504.

Peyre P, Sierra G, Deschaux-Beaume F, Stuart D, Fras G (2007) Generation of aluminium-steel joints with laser-induced reactive wetting. Materials Science and Engineering: A 444(1-2):327-338.

Mathieu A, Shabadi R, Deschamps A, Suery M, Mattei S, Grevey D, Cicala E (2007) Dissimilar material joining using laser (aluminum to steel using zinc-based filler wire). Optics & Laser Technology, 39(3):652-661.

Arghavani MR, Movahedi M, Kokabi AH (2016) Role of zinc layer in resistance spot welding of aluminium to steel. Materials & Design 102:106-114.

Chen N, Wang HP, Carlson BE, Sigler DR, Wang M (2017) Fracture mechanisms of Al/steel resistance spot welds in lap shear test. Journal of Materials Processing Technology 243:347-354.

Miyamoto K, Nakagawa S, Sugi C, Sakurai H, Hirose A (2009) Dissimilar joining of aluminum alloy and steel by resistance spot welding. SAE Technical Paper.

Mustafa A, Bilge D (2008) An investigation of mechanical and metallurgical properties of explosive welded aluminum-dual phase steel. Materials letters 62(25):4158-4160

Xue JY, Li YX, Chen H, Zhu ZT (2018) Wettability, microstructure and properties of 6061 aluminum alloy/304 stainless steel butt joint achieved by laser-metal inert-gas hybrid welding-brazing. Transactions of Nonferrous Metals Society of China 28(10):1938-1946.

Meshram SD, Mohandas T, Reddy GM (2007) Friction welding of dissimilar pure metals. Journal of Materials Processing Technology 184(1-3):330-337.

Zhang S, Gao K, Hong S.-T, Ahn H, Choi Y, Lee S, Han HN (2021) Electrically assisted solid state lap joining of dissimilar steel S45C and aluminum 6061-T6 alloy. Journal of Materials Research and Technology 12:271-282.

Findik F (2011) Recent developments in explosive welding. Materilas & Design 32:1081-1193.

Milani AM, Paidar M, Khodabandeh A, Nategh S (2016) Influence of filler wire and wire feed speed on metallurgical and mechanical properties of MIG welding-brazing of

automotive galvanized steel/5754 aluminum alloy in a lap joint configuration. The International Journal of Advanced Manufacturing Technology, 82(9):1495-1506.

Niu S, Chen S, Dong H, Zhao D, Zhang X, Guo X, Wang G (2016) Microstructure and properties of lap joint between aluminum alloy and galvanized steel by CMT. Journal of Materials Engineering and Performance 25(5):1839-1847.

Thomas WM, Nicholas ED, Needham JC, Murch MG (1991) Temple-Smith, P.; Dawes, C.J. GB Patent application no.9125978.8[J]. International patent application no. PCT/GB92/02203.

Wang L, Huang YX (2018) Friction stir welding of dissimilar aluminum alloys and steels: a review. The International Journal of Advanced Manufacturing Technology 99(5):1781-1811.

Watanabe T, Takayama H, Yanagisawa A (2006) Joining of aluminum alloy to steel by friction stir welding. Journal of Materials Processing Technology 178(1-3):342-349.

Kimapong K, Watanabe T (2005) Lap Joint of A5083 aluminum alloy and SS400 steel by friction stir welding. Materials transactions 46(4):835-841.

Fereiduni E, Movahedi M, Kokabi AH (2015) Aluminum/steel joints made by an alternative friction stir spot welding process. Journal of materials processing technology 224:1-10.

Coelho RS, Kostka A, Dos Santos JF, Kaysser-Pyzalla A (2012) Friction-stir dissimilar welding of aluminum alloy to high strength steels: mechanical properties and their relation to microstructure. Materials Science and Engineering: A 556: 175-183.

Bozzi S, Helbert-Etter AL, Baudin T, Criqui B, Kerbiguet JG (2010) Intermetallic compounds in Al 6016/IF-steel friction stir spot welds. Materials Science and Engineering: A 527:4505-4509.

Pourali M, Abdollah-zadeh A, Saeid T, Kargar F (2017) Influence of welding parameters on intermetallic compounds formation in dissimilar steel/aluminum friction stir welds. Journal of Alloys and Compounds 715:1-8.

Piccini JM, Svoboda HG (2017) Tool geometry optimization in friction stir spot welding of Al-steel joints. Journal of Manufacturing Processes 26:142-154.

Jeon CS, Hong S.-T, Kwon YJ, Cho HH, Han HN (2012) Material properties of friction stir spot welded joints of dissimilar aluminum alloys. Transactions of Nonferrous Metals Society of China 22:s605-s613.

Yuan W, Mishra RS, Webb S, Chen YL, Carlson B, Herling DR, Grant GJ (2011) Effect of tool design and process parameters on properties of Al alloy 6016 friction stir spot welds. Journal of Materials Processing Technology 211(6):972-977.

Zandsalimi S, Heidarzadeh A, Saeid T (2018) Dissimilar friction-stir welding of 430 stainless steel and 6061 aluminum alloy: Microstructure and mechanical properties of the joints. Proceedings of the Institution of Mechanical Engineers, Part L: Journal of Materials: Design and Applications 233(9):1791-1801.

Sina H, Corneliusson J, Turba K, Iyengar S (2015) A study on the formation of iron aluminide (FeAl) from elemental powders. Journal of Alloys and Compounds 636:261-269.

Sundman B, Ohnuma I, Dupin N, Kattner UR, Fries SG (2009) An assessment of the entire Al-Fe system including D03 ordering. Acta Materialia 57(10):2896-2908.

Tanaka T, Hirata T, Shinomiya N, Shirakawa N (2015) Analysis of material flow in the sheet forming of friction-stir welds on alloys of mild steel and aluminum. Journal of Materials Processing Technology 226:115-124.

CHAPTER Ⅲ

FRICTION STIR WELDING OF AA3003-CLAD AA6013 THIN SHEETS: MICROSTRUCTURAL CHANGES RELATED TO TENSILE PROPERTIES AND FATIGUE FAILURE MECHANISM

ABSTRACT

The microstructure, tensile properties, and fatigue behavior of friction stir welding (FSW) joints of multilayer AA3003-clad AA6013 are experimentally investigated. Linear butt welding is performed using a concave tool equipped with a columnar threaded pin at a rotating speed of 600 rpm and a transverse speed of 200 mm/min. The microstructures of FSW joints were observed using a field emission scanning electron microscope equipped with an electron backscatter diffraction system and an energy dispersive spectrometer. The microstructural characterization in the stir zone (SZ) reveals grain refinement, precipitate refinement, zigzag line, and the AA3003-clad layer fragments due to material mixing. The tensile test result of all-weld joints shows that the tensile strength of the SZ is significantly higher than that of base metal, while the cross-weld joints show a typical ductile fracture in the base metal. The result of fatigue tests shows that all the cross-weld joints fracture from the SZ. Analysis of the fatigue failure mechanism indicates that the crack causing the fatigue fracture originates from the AA3003-clad layer fragments in the advancing side of the SZ. The fatigue analysis also confirms that surface roughness and zigzag line are not the cause of the final fatigue fracture of the cross-weld joint for the present study.

3.1 Introduction

Lightweight alloys have attracted significant attention in the automotive industry to reduce environmental pollution and unnecessary energy waste. Among various lightweight materials, using aluminum (Al) alloys to replace steels is a popular way to achieve lightweight automobiles. At the same time, substantial growth of battery-driven electric vehicles demands more advanced materials that can represent different properties in a single structure. The concept of multilayer clad sheets, for example, Al-clad Al sheets, can be effectively used to represent different properties in a single structure. In the design of Al-clad Al sheets, an Al alloy with excellent corrosion-resistance can be placed on the surface as the clad layer while a high-strength Al alloy is used as the core (Chen et al., 2005). In this way, Al-clad Al sheets can be employed to make up for the shortcomings of traditional aluminum alloys in the automobile industry, without losing the lightweight benefit. Roll cladding is a typical commercial way to produce Al-clad Al sheets without any filler or adhesive agent; this process is even more beneficial due to its sizeable reduction in material thickness (Basak. et al., 2022).

Just like conventional monolithic Al alloys, joining of Al-clad Al sheets using traditional fusion welding technologies, including resistance spot welding and gas tungsten arc welding, can induce various technical difficulties, such as poor weld consistency, eutectic formation, and the presence of porosity in the fusion zone (Gao et al., 2021; AMucino, 2010; Marzoli et al., 2006; Murugan et al., 2008; Hasanniah et al., 2018). To overcome the drawbacks of traditional fusion welding processes for Al alloys or Al-clad Al sheets, FSW can be considered as a promising substitute (Meng et al., 2021; Jabraeili et al., 2021; Wang et al., 2008; Tan et al., 2017; Khan et al., 2017). Previously, a few researchers have carried out work in the FSW of Al alloys and Al-clad Al sheets. Fallu et al. (2014) achieved the joining of an AA3025-clad AA5083 sheet using a two-flat pin tool by FSW. Xiao et al. (2010)

produced defect-free joints of 6 mm thick SiCp/2009Al composite and 2024Al-T351 alloy successfully by FSW with and without the tool pin. Wert (2003) reported the microstructural evolution of a FSW joint of AA2024 and AA2014 reinforced with 20 vol.% Al_2O_3. However, the formation of a complex inhomogeneous microstructure by mixing materials in FSW of Al clad Al sheets and the effect of microstructure on the mechanical properties of the joint call for further study. In the present study, for a newly developed Al-clad Al sheet for a structural component of battery-driven electric vehicles, the complicated microstructure caused by the material intermixing of the surface clad layer into the core during FSW was analyzed. Additionally, the effect of the complicated microstructure on the tensile properties and fatigue behavior of the joint was discussed.

3.2 Experimental setup

A multilayer clad sheet (1.5 mm thick) was chosen as a base metal (BM). The BM was composed of a 1.20 mm thick Al alloy 6013 (AA6013) core with 0.15 mm thick Al alloy 3003 (AA3003) clad layers at the top and bottom of the core, as shown in Figure 3.1(a). The multilayer-clad sheet was heat treated at 450 ℃ for 18 hours after roll cladding of AA6013 core and AA3003 clad layers. Before FSW, the multilayer-clad sheet was cut to 150 mm (length) x 100 mm (width). The length direction of the clad sheet for FSW corresponded to the rolling direction of the sheet. The chemical composition of the BM is presented in Table 3.1.

Table 3.1 The nominal chemical compositions of base metals (alloying elements, wt.%).

Alloys	Al	Mg	Si	Cu	Mn	Fe	Zn	Cr	Ti
AA6013	Rem.	0.80-1.2	0.60-1.0	0.6-1.1	0.2-0.8	≤0.5	≤0.25	≤0.10	≤0.10
AA3003	Rem.	-	0.6	0.05-0.2	1.0-1.5	0.7	0.10	-	-

Before FSW, the joining edges of the sheets were ground with 320-grit sandpaper to remove the oxide layer, and then cleaned with acetone to remove impurities. The clad sheets were butt friction stir welded along the length (corresponding to the rolling direction of the sheet) using a custom-made FSW machine (RM1A, TTI, USA), as schematically shown in Figure 3.1(a). The FSW tool was made of H13 tool steel and equipped with a columnar threaded pin. The parameters and detailed dimensions of the tool geometry used in the FSW process are listed in Table 3.2. The tool tilt angle between the tool rotation axis and the normal direction of the sheet was 1.5 °, as shown in Figure 3.1(a).

Table 3.2 Dimensions of the FSW tool and process parameters

FSW Tool	Shoulder Diameter	Shoulder type	Probe length	Pin diameter
	10 mm	Concave	1.2 mm	3 mm
Parameters	Rotating Speed	Transverse Speed	Penetration Depth	Tilt Angle
	600 rpm	200 mm/min	1.3 mm	1.5°

Metallographic specimen was prepared according to ASTM E3-11. After FSW, the cross section of the joint was cut along the perpendicular direction of the joining direction for microstructural observation (Figure 3.1(b)). Subsequently, the specimens were ground with 320-1200 grit papers, polished with a 1.0 μm diamond paste suspension. The specimen was etched using Keller's reagent for 15 sec and then washed with alcohol (dried by forced air). The macrostructure of the FSW joint was firstly observed by optical microscopy (OM) (GX41, Olympus Corp., Tokyo, Japan) to identify macroscopic defects of the joint. The microstructures of FSW joints were further observed using a field emission scanning electron microscope (FE-SEM: JSM7600F, JEOL Ltd., Tokyo, Japan) equipped with an electron backscatter diffraction system (EBSD: EDAX-TSL Hikari, USA). Chemical analysis was performed using FE-SEM equipped with an energy dispersive spectrometer (EDS: X-Max50, Horiba, Japan) at 15 kV with a working distance of 14.8 mm. The inverse pole figure (IPF) and kernel average misorientation (KAM) were obtained to understand the microstructural changes.

To evaluate the mechanical properties, the Vickers hardness profiles of the FSW joint were measured along the four horizontal lines, which were 0.3, 0.6, 0.9, and 1.2 mm from the top of the joint, using a fully calibrated Vickers indenter (A-1170, Leica, Germany) with a load of 0.49 N for 10 sec. Cross-weld tensile specimens (Figure 3.1(b)) were extracted perpendicular to the joining direction to confirm successful joining based on the occurrence of BM fracture. All-weld tensile specimens (Figure 3.1(c)) were also extracted along the

joining direction of the joint to evaluate the mechanical properties of the SZ. The detailed dimensions of a tensile sample are shown in Figure 3.1(d). For comparison, tensile samples of BM with dimensions identical to those of the all-weld tensile specimens were prepared along the rolling direction of the sheet. At least three specimens for each BM, all-weld joint, and cross-weld joint were used for tensile test at room temperature at a strain rate of 1×10^{-3} s^{-1}. The fractured surfaces of all-weld and BM tensile specimens were observed using SEM. Finally, the cross sections of fractured all-weld and BM tensile specimens were observed by OM.

The fatigue tests of cross-weld specimens (Figure 3.1(b)) were performed to evaluate the fatigue performance of the FSW joint at room temperature. Since the surface of a welded component is not polished in general practical applications, the cross-weld specimens were used in fatigue test without surface polishing (Lee et al., 2020; As et al., 2008). Prior to the fatigue test, the surface roughness of the FSW joint was measured perpendicular to the welding direction by a 3D laser scanning microscope (VK-X210, Keyence, Japan). In fatigue tests, a sinusoidal waveform loading was used at a constant frequency of 20 Hz with the stress ratio R = 0.1. To ensure the reliability of the fatigue test, at least three specimens were selected for each stress amplitude level. After fatigue tests, the cross section of the fatigue-tested specimen was observed by OM. Besides, the fatigue fractured surface of the specimen was investigated by SEM and analyzed by EDS.
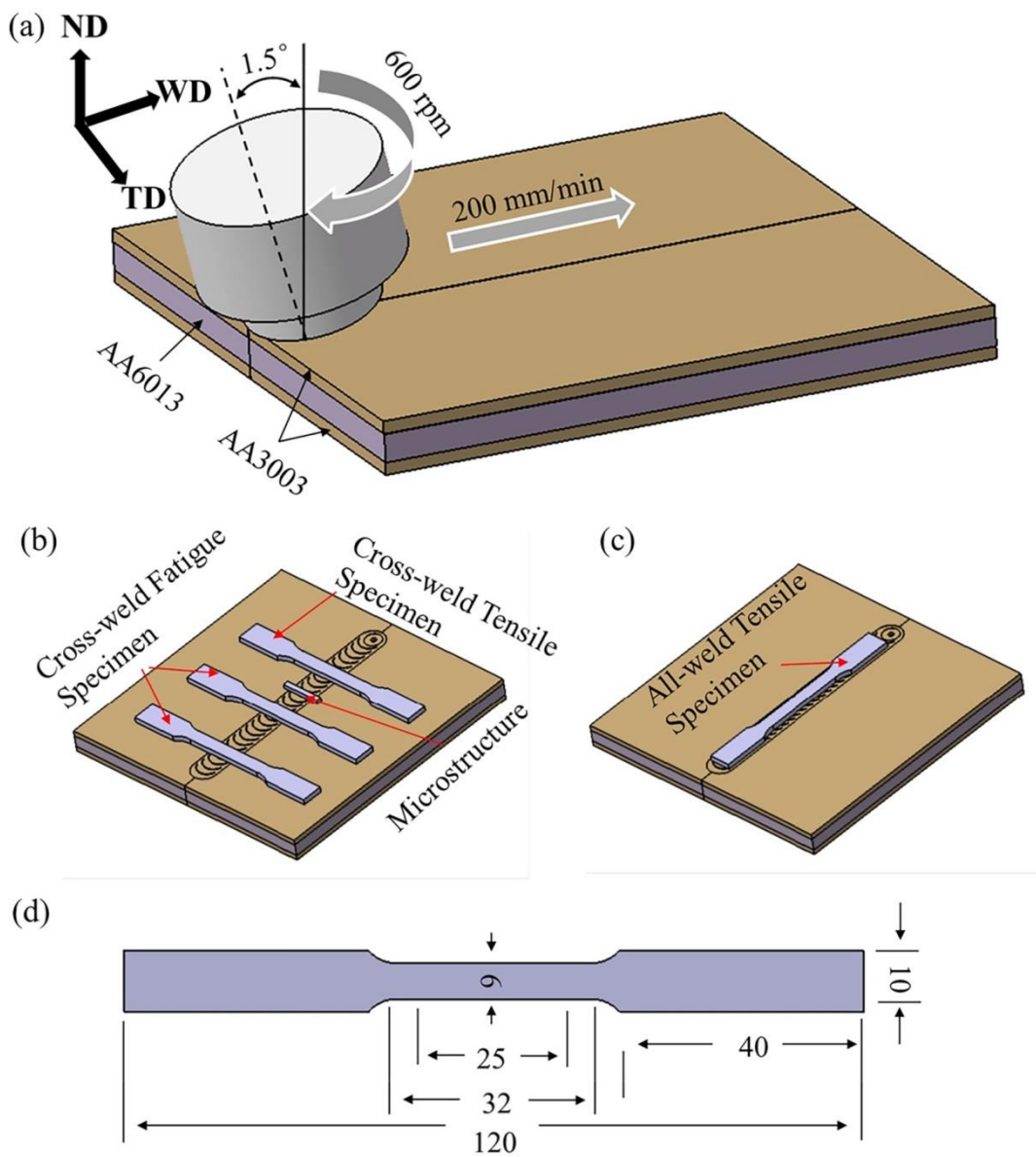
Figure 3.1 (a) The schematic of friction stir welding, (b) extraction of cross-weld sample, (c) extraction of all-weld tensile sample from the weld, (d) dimensions of all-weld, cross-weld, and BM samples

3.3 Results and discussion

The transverse cross section of the FSW of Al-clad Al sheets is shown in Figure 3.2(a). The FSW joint includes base metal (BM), thermo-mechanically affected zone (TMAZ), and SZ with a typical basin-shape. Due to the different microstructural characteristics depending on the SZ position, the SZ was divided into three zones: pin influenced zone (PIZ), and shoulder influenced zone at advancing and retreating sides (SIZ-AS, SIZ-RS). A faint zigzag line (Figure 3.2(c)) as a result of insufficient shattering of the oxide layer on the sheet surface was formed in the PIZ, which is a controversial feature in terms of its effect on the mechanical performance of the FSW joint [Zhang et al., 2019; Di et al., 2007]. Note that the zigzag line formed by the oxide layer on the butt surface of the workpiece is difficult to be completely eliminated (Zhou et al., 2006). Therefore, the effect of the zigzag line on the fatigue properties should be considered.

The determined boundary between SIZ-AS and TMAZ (Figure 3.2(b)) is more distinct compared to that between SIZ-RS and TMAZ (Figure 3.2(d)). This could be explained as the result of different material flow directions between AS and RS. The material flow pattern of FSW Al-clad Al sheets consisted of two parts: the mixing of the surface clad layer materials into the core; the flow of material from the AS to the RS. At the AS, the AA3003-clad layer under the shear force and downward pressure was stirred into the AA6013 core and flowed to RS, which deviated from the adjacent material. By contrast, the plasticized material at RS flowed to the rear side of the rotating tool (Zhao et al., 2019). Therefore, a more significant shear force gradient at AS resulted in forming a more distinct boundary between SIZ-AS and TMAZ compared with RS. Further, due to the asymmetric material flow, a larger amount of residual AA3003-clad layer was observed on the surface of SIZ-RS. It was found that some AA3003-clad layer fragments were extruded to the subsurface of SIZ-AS (Figure 3.2(b)) with the direction of material flow.
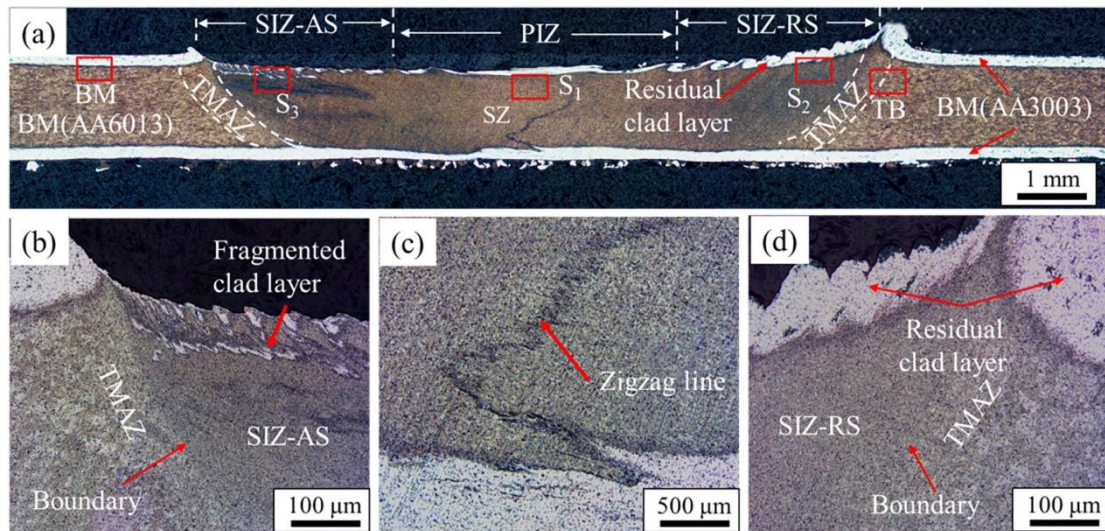
Figure 3.2 Microstructure of FSW joint: (a) overview of the transverse cross section; (b) junction of TMAZ and SIZ-AS; (c) PIZ (d) junction of TMAZ and SIZ-AS

The IPF maps obtained from the BM, junction of TMAZ and BM (TB), PIZ (S_1), SIZ-RS (S_2), and SIZ-AS (S_3) regions of the FSW joint cross section are shown in Figure 3.3. The blue, green, and red colors in the IPF maps (Figure 3.3) represent <111>, <101>, and <001> standard crystallographic directions for the FCC material, respectively. The IPF maps reveal that the grain orientations are different inside the SZ compared to BM. Grains are randomly orientated concerning the standard crystallographic directions in the BM (Figure 3.3(a)) and TMAZ (Figure 3.3(b)). The PIZ (S_1; Figure 3.3(c)) shows much preferred grain orientation in the <101> crystallographic direction compared to the BM. Most of the grains in SIZ-RS (S_2) and SIZ-AS (S_3) are orientated in the <111> and <001> crystallographic directions, respectively, as shown in Figures 3.3(d-e). The asymmetric nature of the strain-induced deformation during FSW played a significant role in the diverse crystallographic orientations of the grains between AS and RS (Mondal et al., 2021).

The IPF map of the BM (Figure 3.3(a)) shows a nearly indistinct interface between the clad layer and core grain. The clad layer and the core can be distinguished based on the

difference in the average grain sizes of 50.0 ± 3.2 μm and 32.5 ± 1.8 μm, respectively. As shown in the IPF map of the BM and TMAZ junction (Figure 3.3(b)), the TMAZ region mainly consist of partially recrystallized grains. This is due to the slight effect of plastic deformation experienced during the FSW process. Compared to the elongated and coarse grain structures of the BM, the SZ with an average size of 2.5 ± 0.6 μm (Figures. 3.3(c-e)) is characterized by the presence of ultra-fine equiaxed grain structures as a result of dynamic recrystallization (Hu et al., 2018).
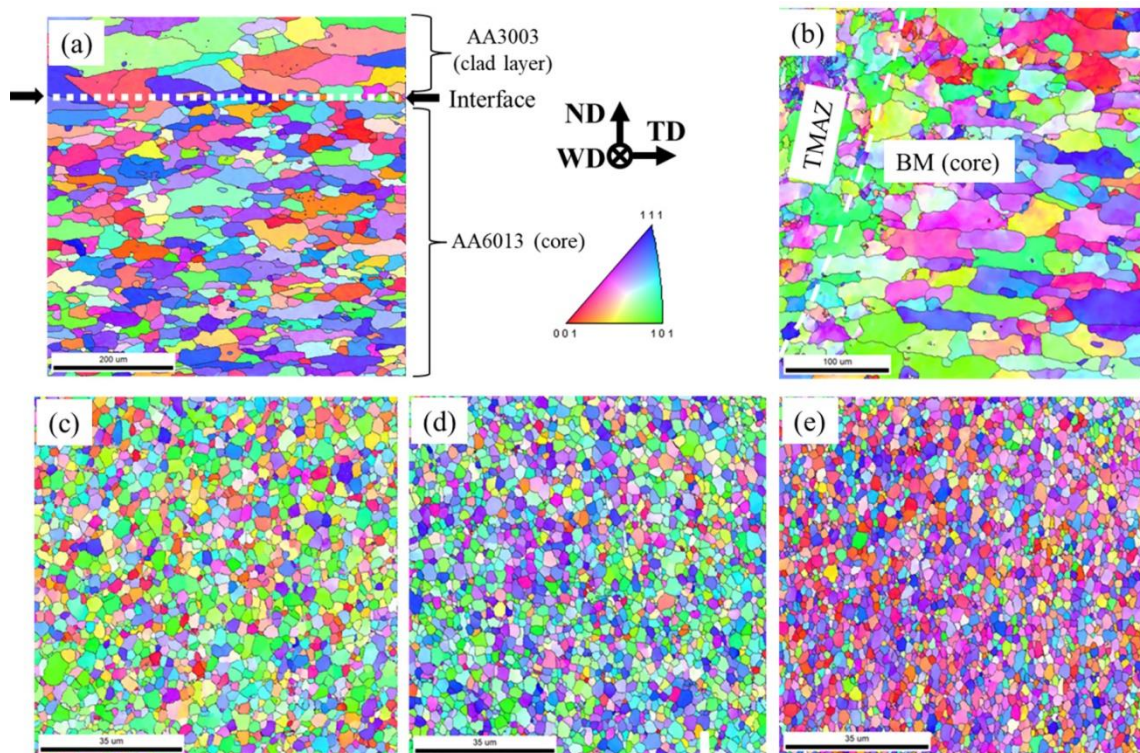
Figure 3.3 IPF maps for (a) BM, (b) junction of BM and TMAZ, (c) PIZ (S$_1$), (d) SIZ-RS (S$_2$), (e) SIZ-AS (S$_3$)

The KAM values of SZ (S_1, S_2, and S_3; Figures. 3.4(c-e)) are slightly higher than that of the AA6013 core of BM (Figure 4(a)), indicating possible intergranular grain misorientations related to the local strain concentration. It can be seen that the KAM value in SIZ-AS (S_3; 0.64) is the highest among all the SZ locations, even though the difference is not significant, as shown in Figures. 3.4(c-e). This can be attributed to the considerable amount of plastic deformation and material mixing at SIZ-AS. The presence of a fragmented clad layer (Figure 3.2(a)) can also be responsible for this observation. Note that the KAM value of TMAZ (0.78) is significantly higher due to the inconsistent deformation of materials between TMAZ and BM.
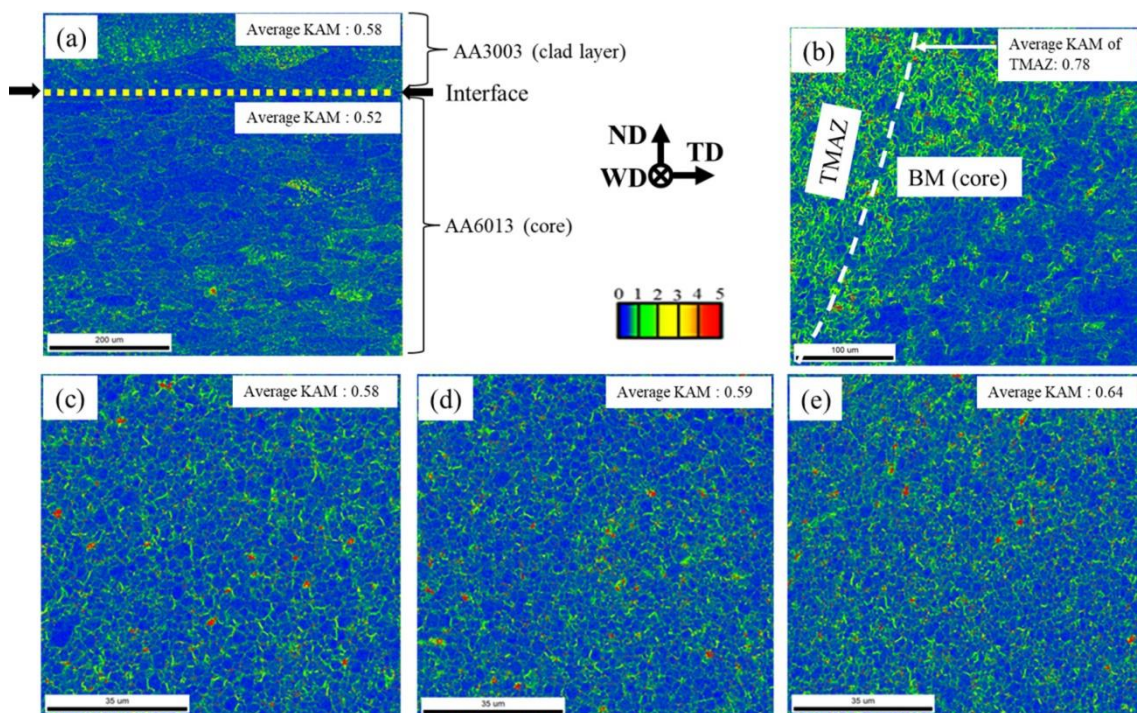
Figure 3.4 KAM maps for (a) BM, (b) junction of BM and TMAZ, (c) PIZ (S_1), (d) SIZ-RS (S_2), (e) SIZ-AS (S_3)

The material flow during FSW affects the distribution, amount, and size of precipitates in the SZ. The possible precipitates were deduced by identifying their chemical compositions through the EDS point scan, as shown in Figure 3.5 and Table 3.3. As summarized in Table 3.3, Al_6(Mn,Fe) precipitates (Tan et al., 2017) were observed in the AA3003-clad layer of the BM (Figure 3.5(a)), and α-(AlFeMnSi) and Q′(AlCuMgSi) precipitates (Barbosa1 et al., 2002) were observed in the AA6013 core of BM (Figure 3.5(c)). The possible Al_6(Mn,Fe) precipitates of the AA3003-clad layer were observed in the SZ (Figure 3.5(e)), indicating that the AA3003-clad layer was stirred into the AA6013 core due to the material mixing caused by the rotating tool. Based on the size distributions of precipitate particles (Figures. 3.5(b, d, and f)), it can be seen that the size of precipitate particles of the AA6013 core is well-distributed in the range of 2 to 5 μm; by contrast, the size distribution of precipitate particles in the SZ is significantly constrained in the range of 0 to 2 μm. Besides, the average size of SZ precipitate particles (1.47 ±0.38 μm) is significantly smaller than that of the AA3003-clad layer (2.23 ± 0.46 μm) and AA6013 core (3.67 ± 0.65 μm). The finer precipitate particles in the SZ can be simply explained as the result of the severe stirring action of the rotating tool.
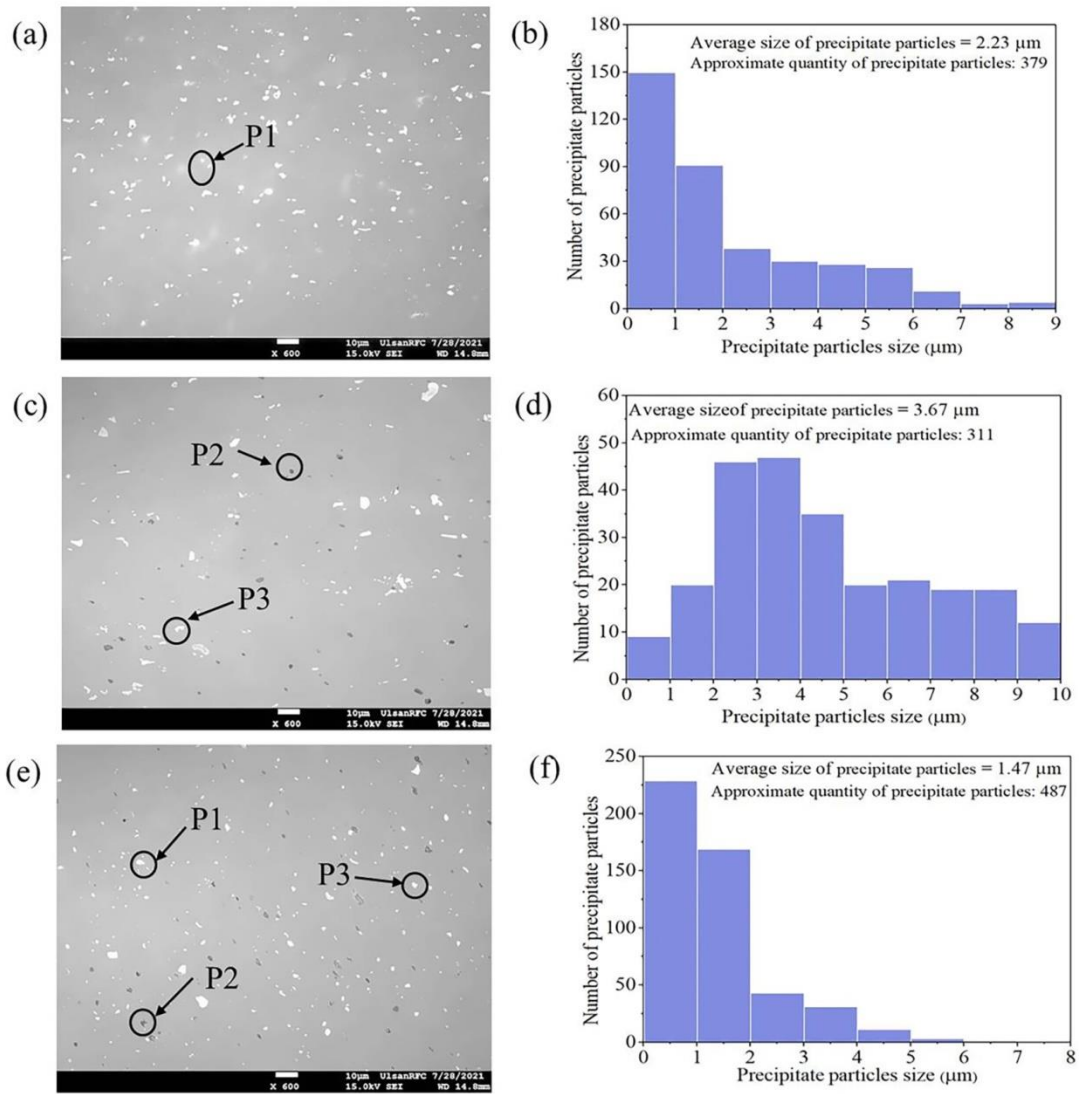
Figure 3.5 SEM images and histograms of size distributions of precipitates: (a-b) AA3003

clad layer of BM, (c-d) AA6013 core of BM, (e-f) SZ

Table 3.3 Chemical compositions of particles and possible precipitates in Figure 3.5

Materials	Location	Composition (at.%)					Possible precipitates
		Al	Fe	Mn	Si	Cu	
BM (Clad layer)	P1	92.18	3.14	4.68	-	-	Al_6(Mn,Fe)
BM (Core layer)	P2	79.96	7.85	4.63	7.56	-	α-(AlFeMnSi)
	P3	78.32	-	5.29	6.87	9.52	Q′(AlCuMgSi)
SZ	P1	90.04	5.63	4.33	-	-	Al_6(Mn,Fe)
	P2	81.28	8.45	3.98	6.29	-	α-(AlFeMnSi)
	P3	82.35	-	4.95	7.62	5.08	Q′(AlCuMgSi)

The hardness of the FSW joint was measured along the four lines: line 1, line 2, line 3, and line 4 in Figure 3.6(a). The hardness distributions (Figures. 3.6(b-e)) show that the joint exhibits fluctuation of hardness values within the SZ, especially from line 1 to line 3. This fluctuated nature of hardness in the SZ could be attributed to variation in microstructure caused by the inhomogeneous material mixing (Figure 3.2). Still, the average hardness of the SZ (68.2 ± 9.3 HV) is clearly higher than that of the AA6013 core (60.8 ± 5.2 HV). The improvement of hardness could be attributed to the grain refinement due to dynamic recrystallization and distribution of finer reinforcement precipitates resulting from the stirring action of the rotating tool (Kalaiselvan et al., 2014; Xie et al., 2021; Xie et al., 2021)
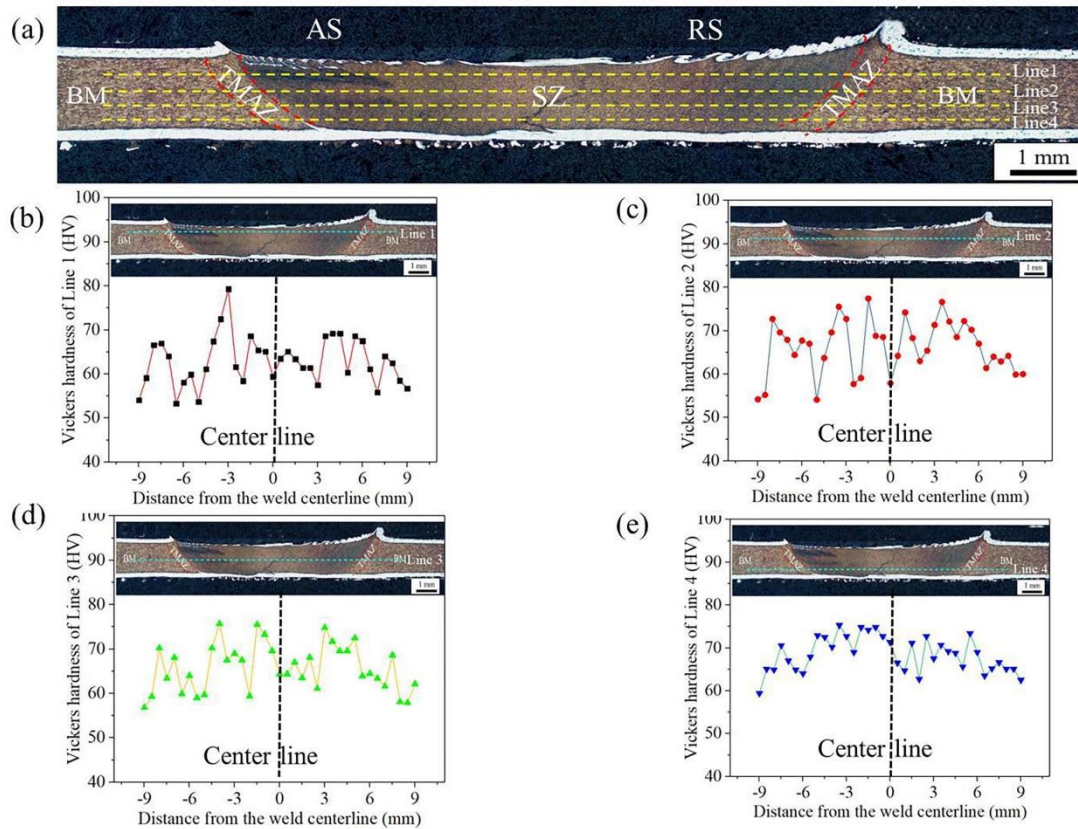
Figure 3.6 (a) Schematic diagram of hardness test locations, microhardness profiles in (b)

line 1, (c) line 2, (d) line 3, and (e) line 4, respectively

A tensile test result of cross-weld joint is shown in Figure 3.7. A ductile fracture with

necking in the BM (Figure 3.7), which typically confirms a successful joining, was observed

during the tensile test of the cross-weld specimen. As shown in the engineering strain-stress

curves of the all-weld specimen and BM (Figure 3.8), in the plastic range, both the

engineering stress-strain curves show a serration caused by unstable plastic flow of material

(Portevin-Le Chatelier effect) due to the presence of precipitates (Mannan et al., 1993). As

summarized in Table 3.4, the ultimate tensile strength (187.1 ± 2.3 MPa) and yield stress

(116.9 ± 1.9 MPa) of the all-weld joint are higher than those of BM (ultimate tensile strength:

152.9 ± 9.8 MPa; yield stress: 75.6 ± 5.2 MPa) in the rolling direction. It is also seen that the

all-weld joint has slightly lower elongation (25.6 ± 2.2%) compared to the BM (27.2 ± 1.3%).

The higher strength of the all-weld specimen compared to the BM can be simply understood as a result of a combination of grain size refinement (Figure 3.3) and precipitation hardening (Figure 3.5) [Zhao et al., 2019; Sabzi et al. 2018].

The tensile fracture surfaces of the BM and all-weld joint (Figure 3.9) are characterized by equiaxed dimples with variable sizes and depths, which reveal that the fracture mechanism was ductile fracture. During their tensile tests, the formation of pore at the beginning of necking grew gradually and finally combined into dimples, indicating that the elongation was related to dimples of fracture surface (Sabzi et al. 2018). The dimples on the fracture surface of BM are larger and deeper compared to that of the all-weld joint, thereby confirming that the BM has higher elongation than the all-weld joint. The cross-sectional image of tensile fractured BM shows (Figure 3.10(a)) a few obvious cracks perpendicular to the tensile load near the necking position of clad layers (AA3003) of BM (Figures 3.10(b)), since the difference in tensile behavior of AA3003-clad layer and AA6013 core is relatively large. In contrast, the tensile properties at different locations of SZ are approximately uniform as a result of the presence of similar refined grain structures (Figure 3.2) caused by dynamic recrystallization in the FSW, thus no significant defects (Figures 3.10(b)) were found from the cross sections of the all-weld joint after the tensile test.
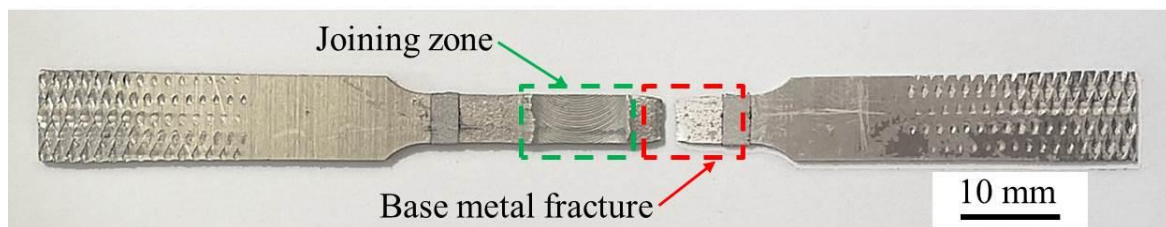
Figure 3.7 Fractured cross-weld FSW joint after tensile test
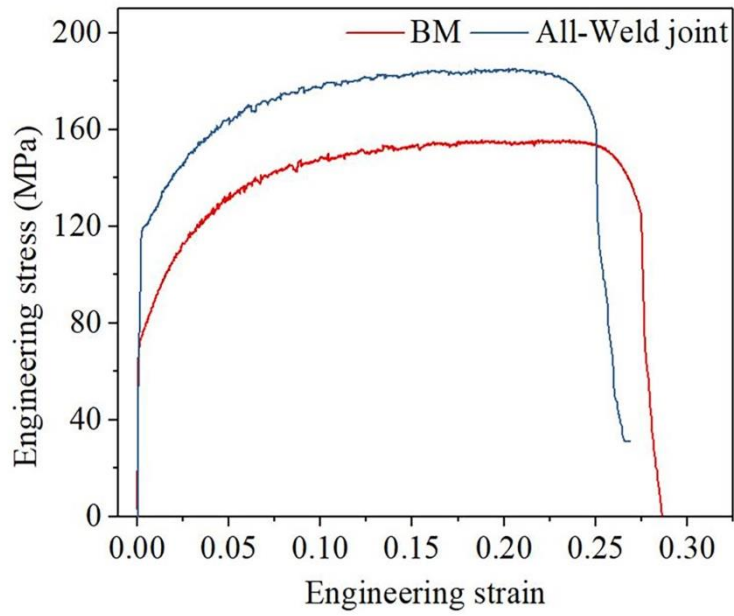
Figure 3.8 Engineering stress-strain curves of BM and all-weld joint

Table 3.4 Mechanical properties of the base metal and all-weld joint

Material	Yield stress (MPa)	UTS (MPa)	Elongation (%)
All-weld joint	116.9 ± 1.9	187.1 ± 2.3	25.6 ± 2.2
BM	75.6 ± 5.2	152.9 ± 9.8	27.2 ± 1.3
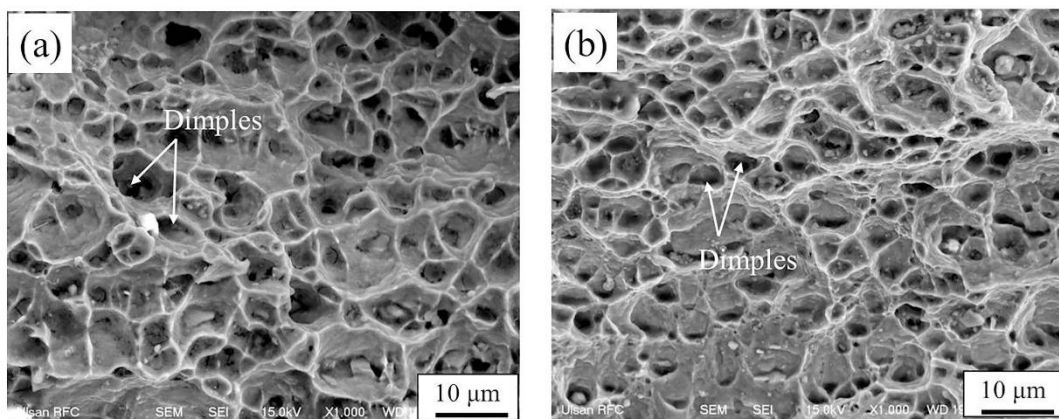
Figure 3.9 SEM image of tensile fracture surface: (a) BM, (b) all-weld joint
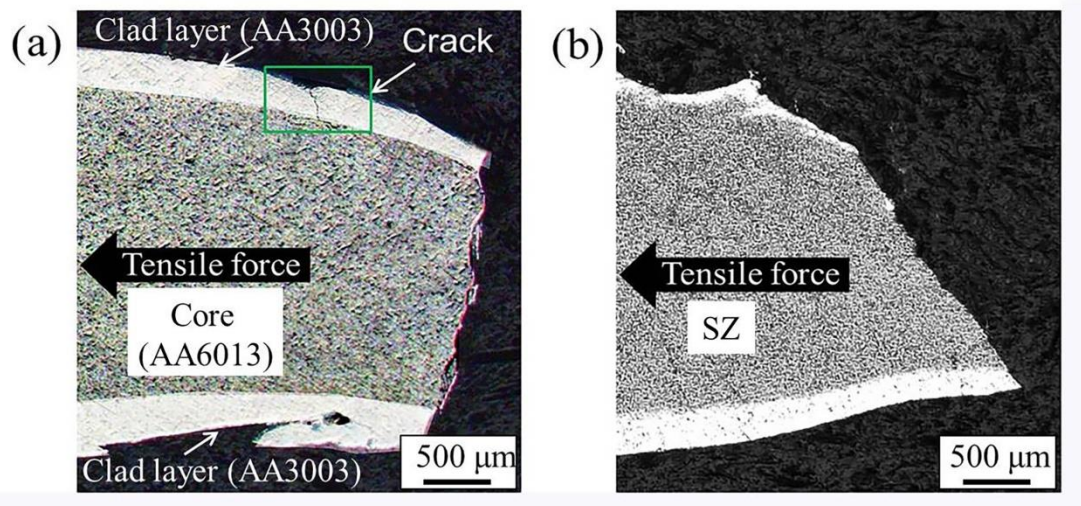
Figure 3.10 Cross-sectional images after tensile test: (a) BM, (b) all-weld joint

The S-N results with the stress ratio of R=0.1 of the cross-weld FSW joint in the interval from 10^5 to 5×10^6 are presented in Figure 3.11. The specimens without fatigue failure after 5×10^6 cycles were marked with a red arrow. Under the lowest fatigue stress (90 MPa) above the yield stress of the BM (75.6 $\pm$ 5.2 MPa), the FSW cross-weld joints did not fracture until 5×10^6 cycles; that is, the joints can fully meet the practical engineering requirements, since they will be clearly under the fatigue limit with the elastic loading condition placed on the BM.
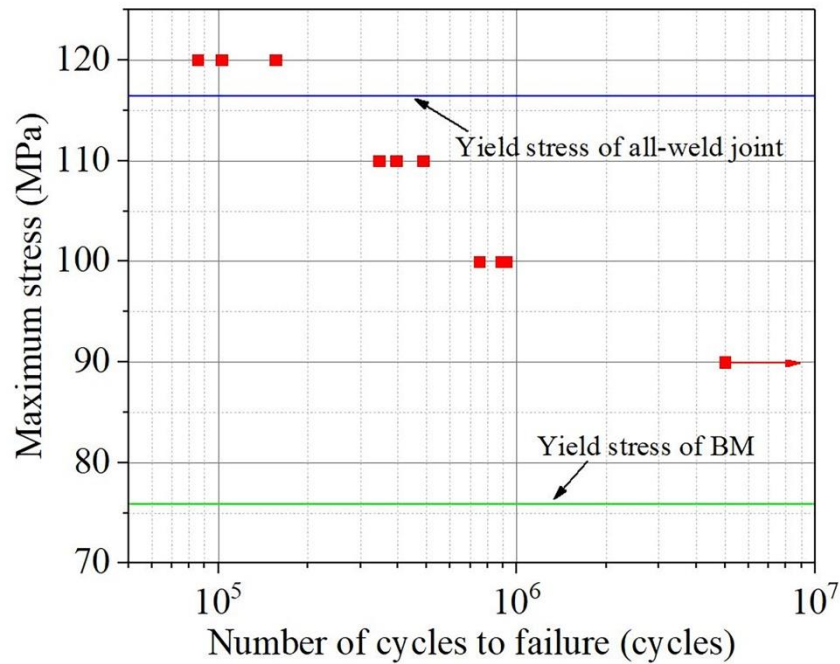
Figure 3.11 S-N results of FSW cross-weld joint

The fatigue life of the FSW cross-weld joint could be related to the surface state and microstructural characteristics. For the FSW cross-weld joint, the surface of SZ exhibits a significantly higher surface roughness value (Figure 3.12) than the BM sides due to the stirring marks. Also, on the surface of the SZ, the SIZ-AS exhibits a lower surface roughness than the PIZ and SIZ-RS. From the AS to RS on the SZ surface, the gradually increasing surface roughness can be understood as a result of the residual AA3003-clad layer by the material flow (Figure 3.2). The stirring marks can be simplified as side-by-side micro-notches resulting in stress concentration.
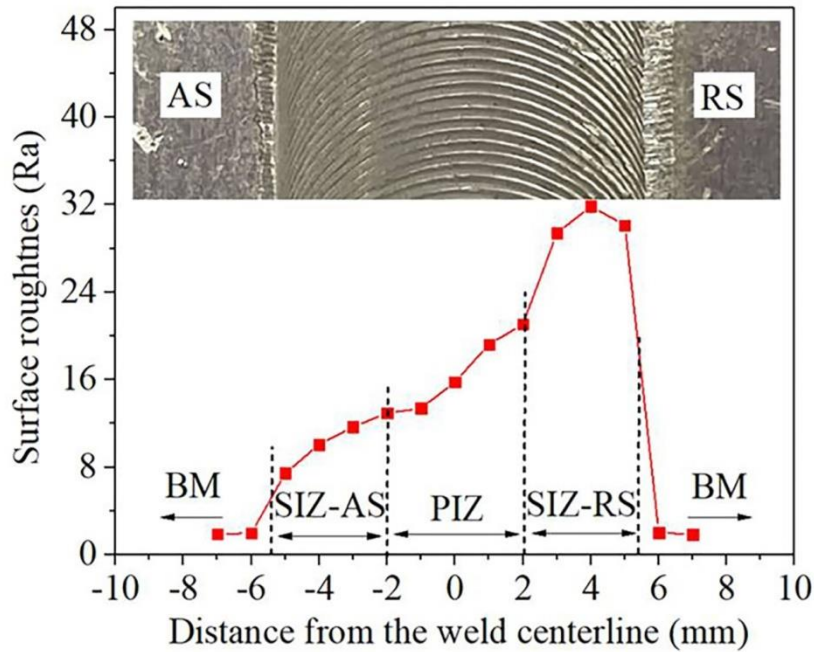
Figure 3.12 Surface roughness profile of FSW cross-weld joint

A few cracks (Figure 3.13(d)) were formed at SIZ-RS with the maximum roughness. However, they did not penetrate through the survived AA3003-clad layer on the surface of SZ after the fatigue failure of the FSW joints. This can be explained as a combined result of the smaller fatigue strain of the SZ with the relatively high tensile strength, as shown in the engineering stress-stain curve in Figure 3.8, and inhibition of crack propagation by the grain refinement caused by a rotating tool (IPF maps in Figure 3.3). More importantly, as shown in Figure 3.13(a), the fatigue fracture location of all the FSW joints occurred in the SIZ-AS, which is inconsistent with the position of the maximum surface roughness (SIZ-RS). As shown in Figure 3.13(c), after fatigue fracture of the FSW joints, no significant fatigue defects were observed in the vicinity of the zigzag line. Therefore, based on the results of the fatigue test and the cross section of the fractured FSW joint, it is confirmed that the surface roughness and zigzag line of the cross-weld joint are not responsible for the final fatigue fracture. Note that depending on the material combination and joint geometry, the Al clad

layer could provide a potential path for the initiation of cracks under the tensile loads (Zhang et al., 2020).
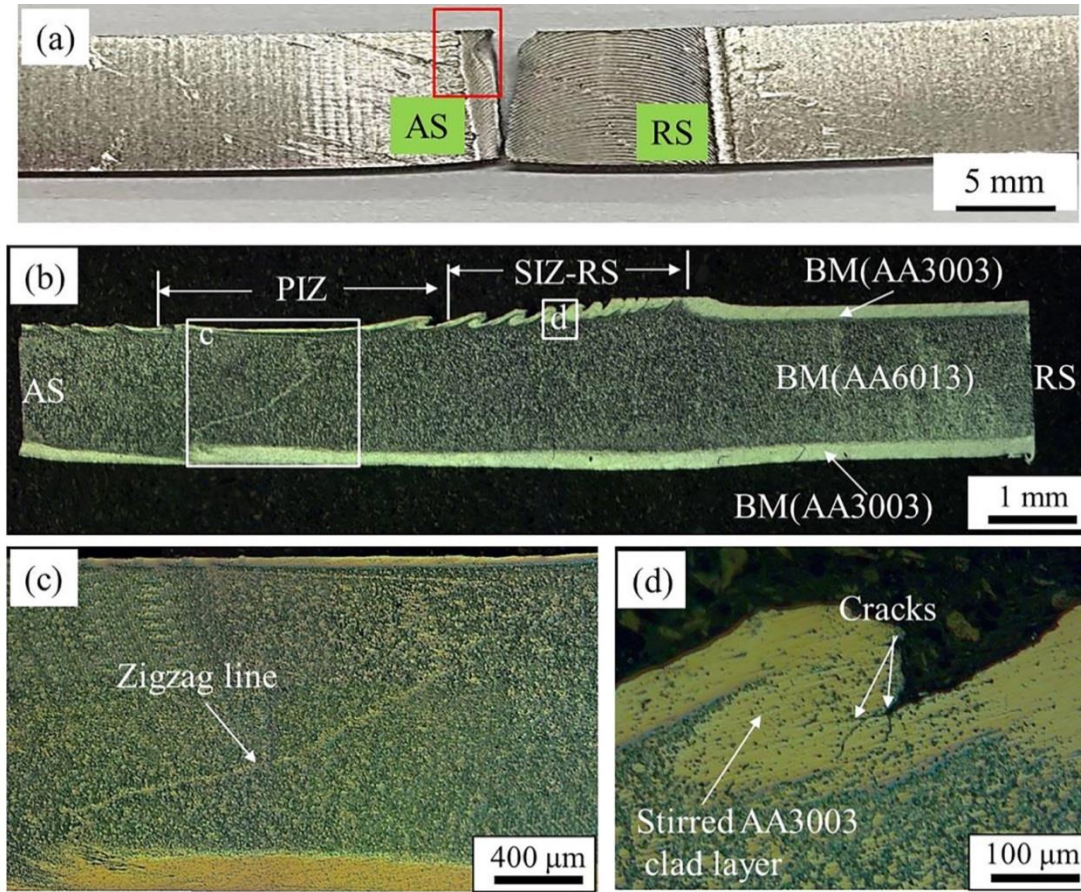
Figure 3.13 (a) A typical fractured cross-weld FSW joint after fatigue test (100 MPa), (b) cross section of fractured FSW joint, (c) magnified PIZ as marked in Figure 3.13 (b), (d) magnified SIZ-RS as marked in Figure 3.13 (b)

The fatigue fracture location and surfaces for the specimen tested at a stress amplitude of 100 MPa ($N=7.48 \times 10^5$ cycles) are shown in Figures. 3.13(a) and 3.14. The partial overview of the fatigue surface (Figure 3.14(a)) shows that the fatigue crack initiated in the subsurface of SIZ-AS. The initiation zone is relatively smooth and characterized by some particles with various sizes and shapes. The EDS area scan (Figures. 3.14(b1)-(b2)) shows

that the elemental composition of particles includes Al, Fe, Si, and Mn. Note that the Mg element included in the core of the BM was not found. These results indicate that particles at the initiation zone (Figure 3.14(b)) are possibly identified as clad layer particles formed by the material mixing. This corresponds well with the conclusion obtained in the discussion of material mixing (Figure 3.2). Furthermore, the cracks around and inside the clad layer particles were observed. Therefore, the clad layer particles located in the surface and sub-surface of top SIZ-AS can be considered as inclusions, which can induce fatigue cracks due to stress concentration (He et al., 2015). Most likely, stress concentration is attributed to the sharp corners of clad layer particles. Besides, the strain inconsistency between the matrix and clad layer particles during the fatigue test is a critical factor in the stress concentration. Also, as discussed in the KAM of SZ, the SIZ-AS (S_3) with the highest KAM value (Figure 3.4(e)) suggests the possible presence of high strain concentration due to plastic deformation and inducing the fatigue crack initiation. Therefore, the cracks, which were formed by a combination of the stress concentration during the fatigue test and higher strain concentration induced by FSW, separated the clad layer particles from the matrix. The crack propagation zone (Figure 3.14(c)) shows prominent striation marks with a river pattern and the fatigue initiation zone as the center (Figure 3.14(a)). The morphology of the crack propagation zone is characterized by the brittle cleavage. The final fracture zone is rough and characterized by a large number of dimples with various sizes (Figure 3.14(d)), which is similar to that on the tensile fractured surface (Figure 3.9(b)).
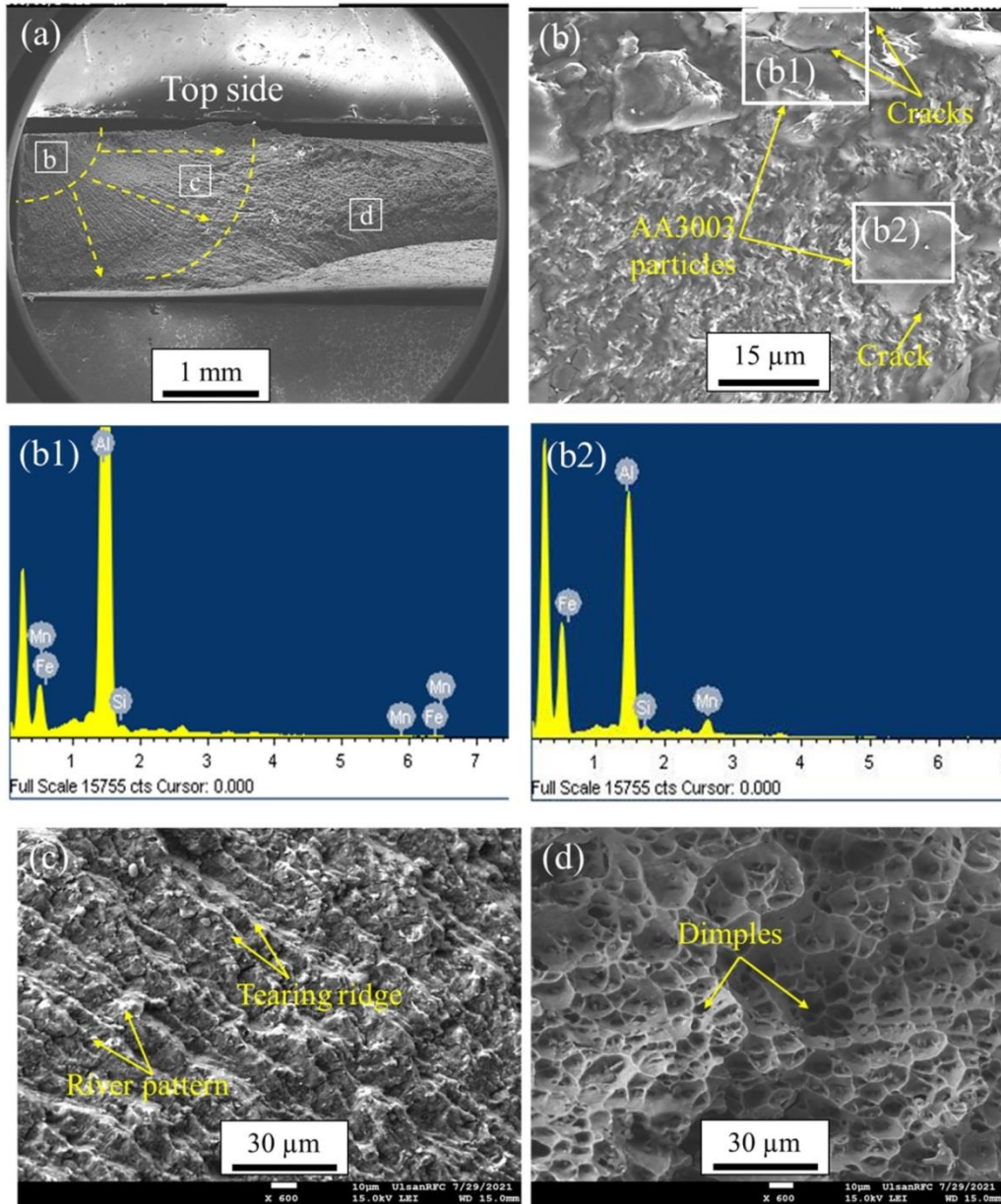
Figure 3.14 SEM images of FSW cross-weld joint fatigued at a stress of 100Mpa: (a) partial overall view as marked in Figure 3.13 by a red rectangle, (b) initiation zone, (b1) elemental area scan as marked in Figure 3.14(b), (b2) elemental area scan as marked in Figure 3.14(b), (c) fatigue crack propagation zone, (d) fast fracture zone

3.4 Conclusion

In this present study, the FSW of the multilayer Al-clad Al sheet was carried out. Combined with the microstructure, the tensile properties and fatigue behavior of FSW were evaluated. Microstructural analysis showed that the AA3003-clad layer was stirred into the AA6013 core by the constant rotation of the tool during FSW. The zigzag line and a small amount of AA3003 fragments were observed at PIZ and SIZ-AS, respectively. The SZ exhibited refined equiaxed grains due to the dynamic recrystallization and uniformly distributed precipitate refinement due to the stirring action of the FSW tool. The result of the tensile test showed that the strength of SZ was higher than that of BM, as result of grain refinement and precipitation hardening. Based on the analysis of surface roughness and observation of cross section of fatigue fractured joint, the surface roughness and the zigzag line did not significantly affect the final fatigue fracture. The presence of the AA3003-clad layer particles at the subsurface of SIZ-AS was primarily responsible for the crack initiation of the FSW joint, while the higher strain concentration in the SIZ-AS during FSW could enhance the fatigue failure in that region. Fatigue crack propagation and fast fracture zone were characterized by the fatigue striations and a large number of dimples, respectively.

Reference

Chen LC, Yang ZG, Jha B, Xia GG (2005) Stevenson JW, Clad metals, roll bonding and their applications for SOFC interconnects. Journal of Power Sources 152:40-45.

Basak S, Mondal M, Gao K, Hong S-T, Anaman SY, HH Cho (2022) Friction stir butt-welding of roll cladded aluminum thin sheets: effect of microstructural and texture changes on mechanical properties. Materials Science and Engineering: A 832:142490.

[3] Gao K, Zhang S, Mondal M, Basak S, Hong ST, Shim H (2021) Friction Stir Spot Butt Welding of Dissimilar S45C Steel and 6061-T6 Aluminum Alloy. Metals 11:1252.

AMucino M (2010) Energy generation during friction stir spot welding (FSSW) of Al 6061-T6 plates. Materials and Manufacturing Processes 25(1-3):167-174.

Marzoli LM, Strombeck AV, Dos Santos JF, Gambaro C, Volpone LM (2006) Friction stir welding of an AA6061/Al2O3/20p reinforced alloy. Composites science and technology 66(2):363-371.

Murugan SP, Cheepu M, Vijayan V, Ji C, Park YD (2018) The resistance spot weldability of a stainless steel/aluminium/low carbon steel 3-ply clad sheet. Journal of Welding and Joining, 36(1): 25-33.

Hasanniah A, Movahedi M, (2018) Welding of Al-Mg aluminium alloy to aluminium clad steel sheet using pulsed gas tungsten arc process. Journal of Manufacturing Processes 31:494-501.

Meng X, Huang Y, Cao J, Shen J, dos Santos JF (2021) Recent progress on control strategies for inherent issues in friction stir welding. Progress in Materials Science 115:100706.

Jabraeili R, Jafarian HR, Khajeh R, Park N, Kim Y, Heidarzadeh A, et al. (2021) Effect of FSW process parameters on microstructure and mechanical properties of the

dissimilar AA2024 Al alloy and 304 stainless steel joints. Materials Science and Engineering: A 814:140981.

Wang X, Wang K, Shen Y, Hu K (2008) Comparison of fatigue property between friction stir and TIG welds. Journal of University of Science and Technology Beijing, Mineral, Metallurgy, Material, 15(3):280-284.

Tan YB, Wang XM, Ma M, Zhang JX, Liu WC, Fu RD, et al. (2017) A study on microstructure and mechanical properties of AA 3003 aluminum alloy joints by underwater friction stir welding, Materials Characterization 127:41-52.

Khan NZ, Siddiquee AN, Khan ZA, Mukhopadhyay AK (2017) Mechanical and microstructural behavior of friction stir welded similar and dissimilar sheets of AA2219 and AA7475 aluminium alloys. Journal of Alloys and Compounds 695:2902-2908.

Fallu J, Izadi H, Gerlich AP (2014) Friction stir welding of co-cast aluminium clad sheet. Science and Technology of Welding and Joining 19(1):9-14.

Xiao BL, Wang D, Bi J, Zhang Z, Ma ZY (2010) Friction Stir Welding of SiCp/Al Composite and 2024 Al Alloy. Science and Technology of Welding and Joining 19(1):9-14.

Wert JA (2003) Microstructures of friction stir weld joints between an aluminium-base metal matrix composite and a monolithic aluminium alloy. Scripta Materialia 49(6):607-612.

Lee S, Pegues JW, Shamsaei N (2020) Fatigue behavior and modeling for additive manufactured 304L stainless steel: The effect of surface roughness. International Journal of Fatigue 141:105856.

As KS, Skallerud B, Tveiten BW (2008) Surface roughness characterization for fatigue life predictions using finite element analysis. International Journal of Fatigue 30(12):2200-2209.

Zhang H, Luo S, Xu W (2019) Influence of Welding Speed on Zigzag Line Feature and Tensile Property of a Friction-Stir-Welded Al-Zn-Mg Aluminum Alloy. Journal of Materials Engineering and Performance 28(3):1790-1800.

Di S, Yang X, Fang D, Luan G (2007) The influence of zigzag-curve defect on the fatigue properties of friction stir welds in 7075-T6 Al alloy. Materials chemistry and physics 104(2-3): 244-248.

Zhou CZ, Yang XQ, Luan GH (2006) Effect of oxide array on the fatigue property of friction stir welds. Scripta materialia 54(8):1515-1520.

Zhao YX, Yang ZY, Domblesky JP, Han JM, Li ZQ, Liu XL (2019) Investigation of through thickness microstructure and mechanical properties in friction stir welded 7N01 aluminum alloy plate. Materials Science and Engineering: A 760:316-327.

Mondal M, Basak S, Das H, Hong ST, Choi H, Park JW, et al. (2021) Manufacturing of magnesium/aluminum bimetallic ring components by friction stir assisted simultaneous forging and solid-state joining. International Journal of Precision Engineering and Manufacturing-Green Technology 8(5):1429-1438.

Hu YY, Liu HJ, Li S, Du S, Sekulic DP (2018) Improving mechanical properties of a joint through tilt probe penetrating friction stir welding. Materials Science and Engineering: A 731:107-118.

Barbosa1 C, Rebello1 JMA, Acselrad O, Dille J, Delplancke J-L (2002) Identification of precipitates in 6013 aluminum alloy (Al–Mg–Si–Cu). International Journal of Materials Research 93(3):208-211.

Kalaiselvan K, Dinaharan I, Murugan N (2014) Characterization of friction stir welded boron carbide particulate reinforced AA6061 aluminum alloy stir cast composite. Materials & Design 55:176-182.

Xie Y, Meng X, Li Y, Mao D, Wan L, Huang Y (2021) Insight into ultra-refined grains of aluminum matrix composites via deformation-driven metallurgy. Composites Communications 26:100776.

Xie Y, Meng X, Chang Y, Mao D, Yang Y, Xu Y, et al. (2021) Ameliorating strength-ductility efficiency of graphene nanoplatelet-reinforced aluminum composites via deformation-driven metallurgy. Composites Science and Technology 219:109225.

Mannan SL (1991) Role of dynamic strain aging on low cycle fatigue. Bulletin of Materials Science 16(6):561-582.

Sabzi M, Dezfuli SM, (2018) Post weld heat treatment of hypereutectoid hadfield steel: characterization and control of microstructure, phase equilibrium, mechanical properties and fracture mode of welding joint. Journal of Manufacturing Processes 34:313-328.

Sabzi M, Dezfuli SM (2018) Drastic improvement in mechanical properties and weldability of 316L stainless steel weld joints by using electromagnetic vibration during GTAW process. Journal of Manufacturing Processes 33:74-85.

Zhang Y, Huang Y, Meng X, Li J, Xie Y, Fan Q (2020) Friction stir lap welding of AA2024-T4 with drastically different thickness. The International Journal of Advanced Manufacturing Technology 106(9):3683-3691.

He C, Liu Y, Dong J, Wang Q, Wagner D, Bathias C (2015) Fatigue crack initiation behaviors throughout friction stir welded joints in AA7075-T6 in ultrasonic fatigue. International Journal of Fatigue 81:171-178.

CHAPTER Ⅳ

Effects of joining zone morphology and microstructure on the mechanical properties of friction stir lap welding of Al-clad Al and Al-clad steel sheets

Abstract

The microstructural characteristics and mechanical properties of friction stir lap welding (FSLW) of thin Al-clad Al (1.5 mm) and ultra-thin Al-clad mild steel (0.7 mm) sheets are experimentally investigated. Optical microscopic observation confirms that the FSLW joints are successfully fabricated without noticeable joining defects, including cracks and hooks. The material flow is correlated with silicon (Si) element distribution in the stir zone (SZ). The distribution of Si element indicates that material flow is asymmetrical between the advancing side (AS) and the retreating side (RS) of the SZ. The tensile test result shows that all the FSLW joints fracture from the Al-clad Al sheet side. The fatigue test result shows that two different crack propagation modes are observed as a combined result of the asymmetric geometry of the FSLW joint and different loading configurations. The fatigue life of the AS-loaded lap joint is lower than that of the RS-loaded lap joint. The tip of the non-bonding region on the AS, which is the fatigue failure initiation position of the AS-loaded lap joint, is located in the junction of the SZ and thermo-mechanically affected zone (TMAZ). The higher dislocation value and smaller grain misorientation angle on the junction of SZ and TMAZ accelerate the degradation of fatigue performance of AS-loaded joint.

Keywords: friction stir lap welding, AA4343-clad AA3003, AA1050-clad mild steel, Si distribution, fatigue failure mechanism

4.1 Introduction

Battery electric vehicles (BEVs) have gained considerable attention to be so called environment-friendly transportations. However, at the same time, the BEVs are facing a strong demand from the market to increase the driving distance. As an effort for a longer driving distance, advanced lightweight structural materials are being increasingly used in various structural components of BEVs. One typical example is the use of clad metal sheets in the battery case structure of BEVs (Hannan *et al*., 2014).

Clad metal sheets consisting of laminated layers of dissimilar metals are widely used in various industries since they have multi-functional properties, which cannot be obtained from conventional monolithic materials (Yilmaz *et al*., 2013; Rhee *et al*., 2004; Park *et al*., 1997). Roll cladding is preferred for the production of clad metal sheets due to the sizeable reduction in the thickness of materials without using any filler or adhesive (Ban *et al*., 2020). Among the lightweight clad metal sheets, the bi/multi-layer Al-clad sheets have already been recognized for energy drive systems of BEVs (Su *et al*., 2015; Chen *et al*., 2005). Depending on the classification of BEVs, sheet materials with high strength and good corrosion resistance become necessary for structural applications, including the battery case. With the concept of clad metal sheets, this type of material system can be produced by cladding the surface of high-strength alloy (mostly steel) with a layer of lightweight corrosion-resistant alloy (mostly Al alloy). This further helps this material system to gain corrosion protection and relatively high strength to weight ratio at the same time (Okui *et al*., 2014).

The conventional fusion lap joining of Al-clad sheets (including Al-clad Al and Al-clad steel) imposes complications as they are composed of different material layers with massive differences in their thermo-mechanical properties (Fallu *et al*., 2014). The lap joining of Al-clad sheet by fusion welding process leads to thermal distortion, delamination of the multi-layers, and solidification defects (Ericsson *et al*., 2007; Raturi *et al*., 2021). Oikawa *et*

66

al. (1996) studied the feasibility of RSW of Al and Al-clad steel. They reported that extensive heat input caused the formation of the thick intermetallic compound and thermal distortion of Al-clad steel. Rahimi *et al*. (2020) investigated the resistance spot welding (RSW) of AA5083 and AA1050-clad St-12 steel sheets. They reported that the AA5083 was thinned after welding, and a few porosities in the nugget zone were observed.

Frictions stir welding (FSW), a solid-state joining process (1991), establishes material flow to accomplish the joining using a rotating tool and overcomes various of fusing joining. Only a few research works on the FSLW of Al-clad sheets have been reported in the past. Movahedi *et al*. (2012) successfully examined the feasibility of FSLW of AA5083 and AA1100-clad St-12 sheets. They found that the joint strength was improved by decreasing the thickness of the AA1100-clad layer. Li *et al*. (2019) reported that the hook is associated with the plasticized metal flow while successfully joining the Al-clad Al sheet using refill friction stir spot welding. Liu *et al*. (2015) investigated the FSLW of 1.9 mm thick Al-clad sheet at different welding parameters. They observed that the redistributed clad layer in the stir zone (SZ) was more dispersed by increasing the rotating tool speed and decreasing the welding speed.

While a few investigations on the FSLW of Al and Al-clad steel have been reported, the effect of material flow and asymmetric microstructure on the mechanical properties is still unclear and needs further studies. The present study experimentally investigates the FSLW of the Al-clad Al thin sheet with ultra-thin Al-clad steel sheet. Firstly, the material flow and microstructural characteristics of the FSLW joint are studied. Combined with the microstructural characteristics of the FSLW joint, the changes of mechanical properties, including hardness, tensile strength, and the fatigue failure mechanism, are then determined.

4.2 Experimental setup

In the present study, the bi-layer AA4343-clad AA3003 (thickness of 1.5 mm) and AA1050-clad mild steel (thickness of 0.7 mm) were chosen as the base materials (BMs) to perform the FSLW. The detailed specification of the BMs and their chemical composition are listed in Table 4.1. The BM sheets were cut into a rectangular shape of 150 mm (length) × 100 mm (width) for FSLW.

Table 4.1 The nominal chemical compositions of base metals (alloying elements, wt.%).

Alloys	Al	Mg	Si	Cu	Mn	Fe	Zn	P	Cr	Ti	C
AA4343	Rem.	-	7.23			0.33	-	-	-	0.02	-
AA3003	Rem.	0.01	0.33	0.14	1.11	0.54	0.10	-	-	-	-
AA1050	Rem.	-	0.6	0.01	-	0.7	-	-	-	0.02	-
Mild steel	-	-	-	-	0.22	Rem.	-	0.006	-	-	0.002

Before joining, the faying surfaces of both BMs sheets were cleaned with acetone to remove oil contamination and dust. Due to the asymmetry in material mixing and microstructural characteristics between the advancing side (AS) and retreating side (RS), two different configurations of FSLW were conducted along the rolling direction of the sheet with an overlap area of 150 mm × 30 mm using a custom-made FSW machine (RM1A, Bond technologies, USA), namely, AS-loaded configuration (Figure 4.1(a)) and RS-loaded configuration (Figure 4.1(b)). The Al-clad Al thin sheet was placed on the ultra-thin Al-clad steel sheet so that both the clad layers met together in the middle surrounded by the AA3003 core (top) and the mild steel (bottom). The FSW tool used in the present study was composed of H-13 tool steel and a columnar threaded pin. The FSLW parameters and the detailed tool geometry are listed in Table 4.2.
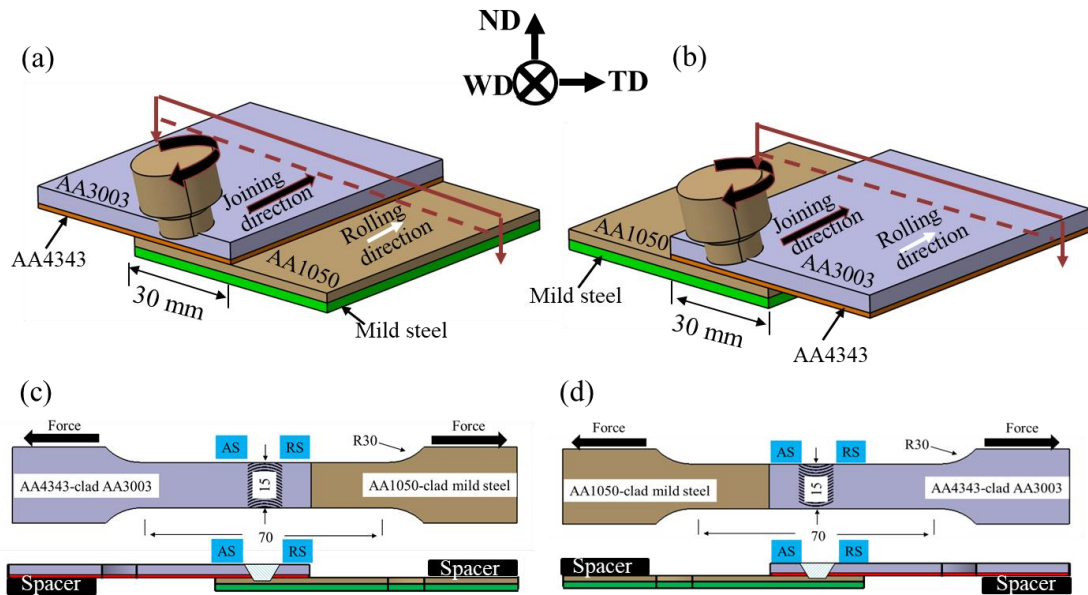
Figure 4.1 Diagram of the FSLW principle of (a) AS-loaded configuration and (b) RS-loaded configuration; specimen dimension of (c) AS-loaded joint and (d) RS-loaded joint

Table 4.2 Dimensions of the FSW tool and process parameters.

FSW Tool	Shoulder Diameter	Shoulder type	Probe length	Pin diameter
	10 mm	Concave	1.7 mm	3 mm
Parameters	Rotating Speed	Transverse Speed	Penetration Depth	Tilt Angle
	800 rpm	100 mm/min	1.75 mm	1.7°

To analyze the microstructures of the FSLW joints, the specimens were cut perpendicular to the joining direction, ground and polished with emery papers followed by 1.0 μm diamond suspension. The macrostructure of the FSW joint was first observed by optical microscopy (OM) (GX41, Olympus Corp., Tokyo, Japan) after etching with Kellers' agent to identify macroscopic defects of the joint. Microstructural analysis of the FSLW joint including a chemical analysis was then conducted using a field emission scanning electron microscope (FE-SEM: JSM7600F, JEOL Ltd., Tokyo, Japan) equipped with an energy dispersive spectrometer (EDS: X-Max50, Horiba, Japan). Next, the electron backscatter diffraction (EBSD) analysis was conducted on the cross-section of the joint. For the EBSD

analysis, the cross section of the joint was polished with 0.25 µm diamond suspension, followed by electrolytic polishing using a solution of 60% ethanol and 40% perchloric acid at 10 °C under a potential of 20 V for 50 sec. The FE-SEM (SU5000, Hitachi High-Technologies Corp., Tokyo, Japan) equipped with an electron backscatter diffractometer (TSL Hikari Super, TSL, USA) was used for the EBSD analysis. The inverse pole figure (IPF), grain boundary character distribution (GBCD), kernel average misorientation (KAM) maps, and pole figures (PF) were obtained to understand the microstructural changes in the SZ.

The mechanical properties of the FLSW joint were evaluated in terms of hardness measurement, tensile test, and fatigue tests. Hardness mapping was carried out on the cross section of the FSLW joint using an automatic Vickers microhardness tester (HM-100, Mitutoyo Corp., Kanagawa, Japan). The microhardness was measured with a load of 0.49 N for a dwell time of 10 sec. The microhardness profiles through the core of the Al-clad mild steel and middle region of the weld cross section (excluding mild steel) were also evaluated separately using the Vickers HM-100 indenter and were plotted in reference to the surface microhardness mapping.

The tensile and fatigue specimens were fabricated perpendicular to the joining direction from the AS-loading (AS-loaded lap joint) and RS-loading (RS-loaded lap joint) configurations of the FSLW joints. The tensile and fatigue test specimen dimensions are shown in Figures 4.1(c-d). Also, the tensile samples of BMs (AA4343-clad AA3003, AA1050-clad mild steel) with dimensions identical to those of the lap joint tensile specimens were prepared along the rolling direction of the sheets. A set of spacers was located at the right and left ends of the specimens to align the faying surface of FSLW joints along the loading axis for both tensile and fatigue tests. The uniaxial tensile tests were carried out at room temperature with a 1 mm/min constant displacement speed using a universal testing machine (DTU900-MH, Daekyung Co., Ltd., Busan, South Korea). Servo hydraulic fatigue

test machine (MTS 809, MTS, USA) was used to analyze the fatigue property of the FSLW joints under a sinusoidal waveform loading at room temperature. The stress ratio of 0.1 and the frequency of 20 Hz were applied to the specimens for fatigue testing. At least three specimens were tested for the fatigue test at each stress level to confirm the data accuracy. After the fatigue test, the cross sections of fatigue fractured specimens were analyzed by OM to understand the failure mechanism of the FSLW joint. Besides, the fatigue fracture surfaces were also observed by SEM.

4.3 Results and discussion

4.3.1 Optical microscopy

The FSLW joint cross section (Figure 4.2(a)) can be divided into three major regions: SZ, thermo-mechanically affected zone (TMAZ), and BMs. No significant hook defects on the AS and RS leading to sheet thinning were observed inside the joint cross section. The formation of hooks due to the vertical flow of plasticized material is restrained by using a small diameter of the tool pin with a properly selected penetration depth into the bottom Al-clad steel sheet (Kumar *et al*., 2008). The non-bonding regions were spotted at the bottom of TMAZ for both AS (Figure 4.2(b)) and RS (Figure 4.2(c)) of the SZ. This is due to the insufficient heat input and plastic deformation during processing (Cederqvist *et al*., 2001; Xu *et al*., 2012). Therefore, the effective joining length equals to the horizontal distance between both tips of non-bonding regions.

At the bottom of the SZ, the mild steel core (Figure 4.2(d)) was slightly deformed by the compressive loading of the tool pin during its plunging towards the desired penetration depth (1.75 mm). The deformed mild steel also found in the middle of SZ. Even though it seems that the tool pin did not cause the significant stirring inside the mild steel core during FSLW, the present study revealed the presence of fragmented steel particles in the SZ (Figure 4.2(d)), which were probably sheared during the severe stirring motion of the tool pin with its high plunging force (Zandsalimi *et al*., 2019).

The bottom of the SZ shows asymmetric material mixing features due to the asymmetric nature of the FSLW forces between the AS and RS. The material mixing is more evident at the AS of SZ, indicating that the Si elements flowed from AA4343 to AA1050. However, the residual AA1050-clad layer is still cladded on the surface of the mild steel core at the edge of the AS of SZ. This could be explained by the fact that the plasticized material flow in the SZ presented an arc pattern under the combined action of compressive loading

and the centrifugal force of the rotating tool (Cederqvist *et al*., 2001; Xu *et al*., 2012; Zandsalimi *et al*., 2019). Compared with the AS of SZ, a visible layered structure was observed at the faying surface of the RS of SZ due to the lack of adequate stirring of the three different Al alloys.
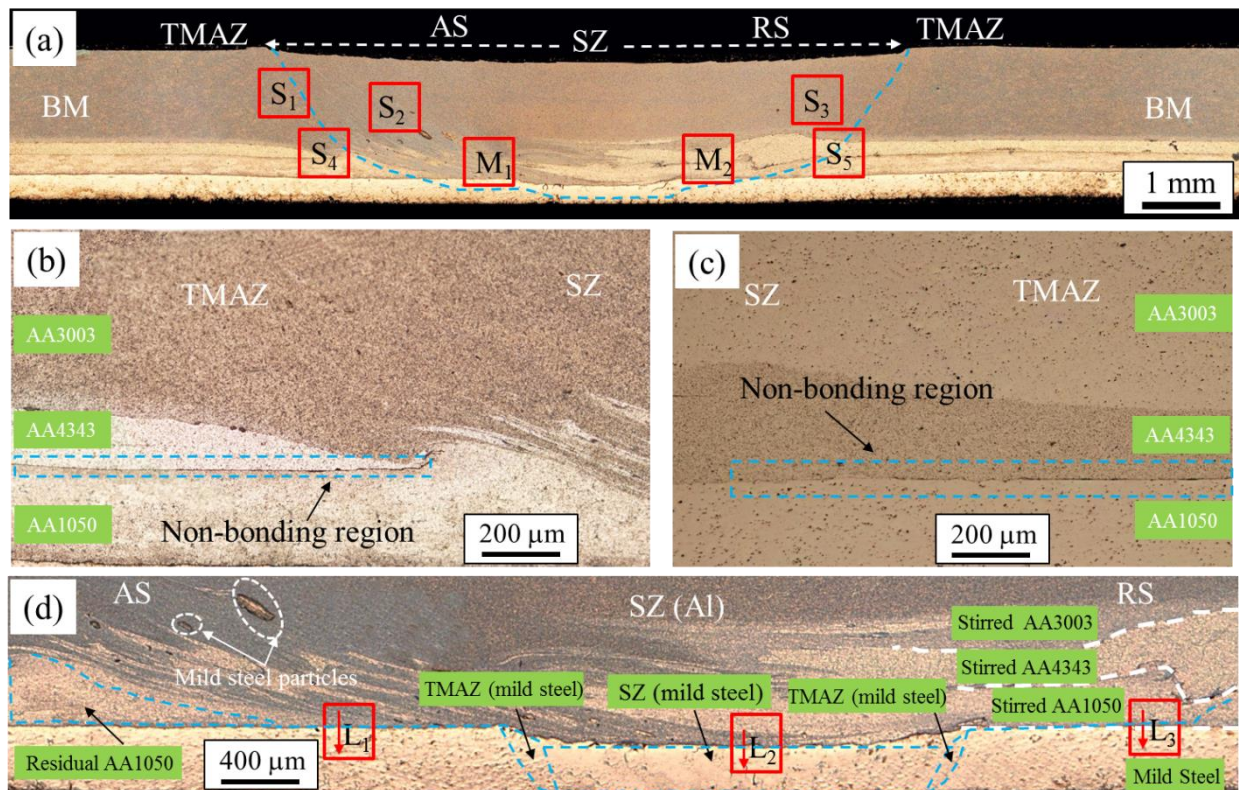
Figure 4.2 Microstructure of FSLW joint: (a) overview of the transverse cross section, (b) non-bonding region on the AS, (c) non-bonding region on the RS, (d) bottom region of SZ.

4.3.2 SEM analysis

The result of SEM and EDS line scan at the interface of BM Al-clad Al sheet (Figure 4.3(a_{1-2})) shows that the concentration of the Si element in the AA4343-clad layer is significantly higher than that in the AA3003 core. Therefore, the mixing of the faying surface materials could be evaluated by the distribution of Si elements in the AS (M_1) and RS (M_2) of the SZ. The EDS line scan results in Figures 3(b_1) and (b_2) show that the Si element displays a relatively uniform distribution, indicating homogenous material mixing at the AS of SZ.

Contrarily, the distribution of Si element at the RS of SZ (Figures 3(c_1) and (c_2)) is restricted in a specific range of area (stirred AA4343-clad layer). This phenomenon in the RS of SZ suggests that the intermixing of the faying surface materials is limited. The asymmetric nature of the FSLW forces is responsible for the different Si element distributions at the AS and RS of SZ (Chen *et al*., 2012).
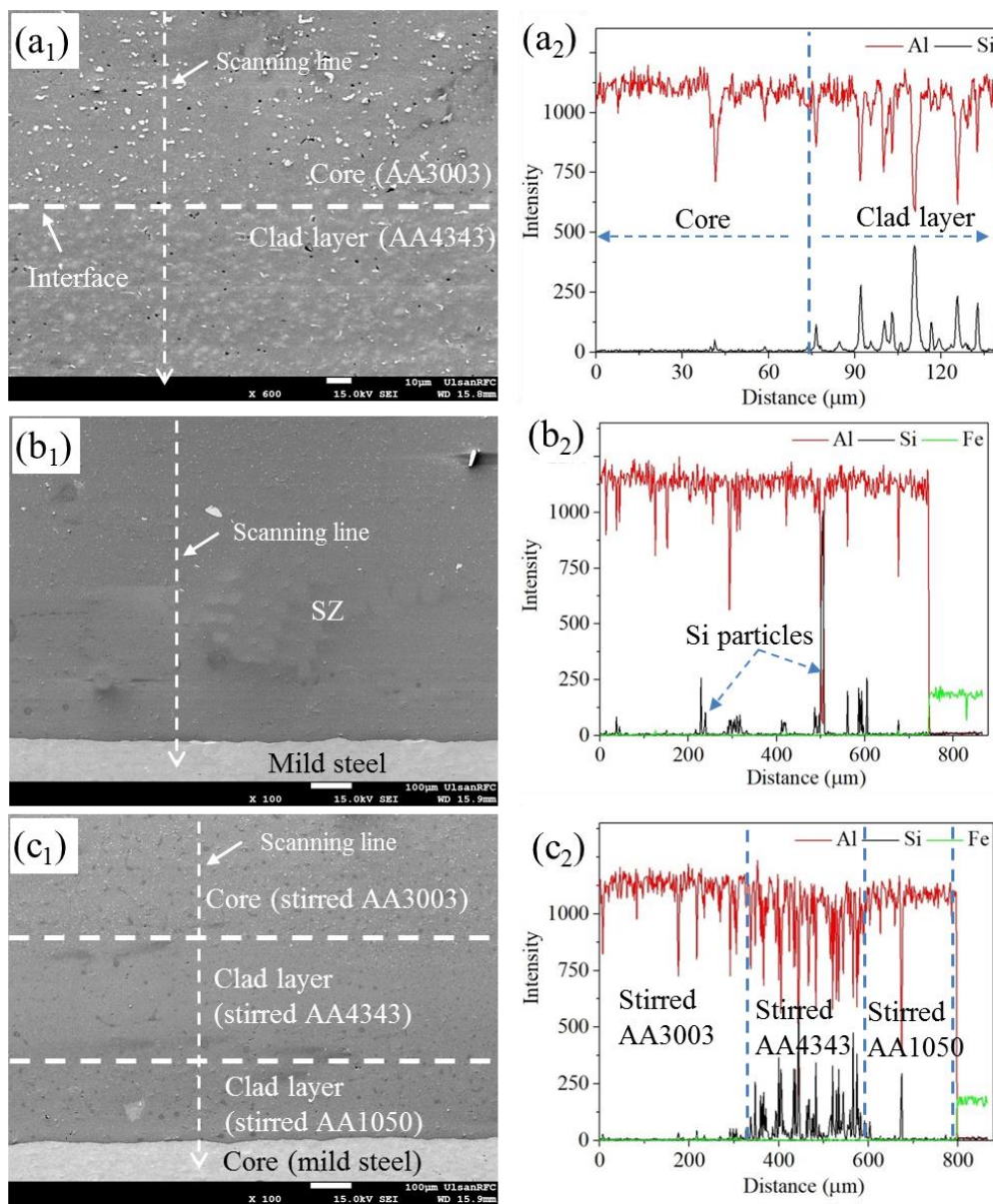

Figure 4.3 SEM images and EDS line scans for (a) BM (AA4343-clad AA3003), (b) SZ on the AS (M_1), (c) SZ on the RS (M_2).

The EDS point scan identifies the possible precipitations inside the AA3003 core and the AS (S_2) and RS (S_3) of the SZ. As summarized in Table 4.3, Al_6(Mn, Fe) and Al(Mn, Fe)Si precipitates (Basak *et al*., 2022) are uniformly distributed in the AA3003 core (Figure 4.1(a_1)) and the AS ((Figure 4.1(b_1)) and RS ((Figure 4.1(c_1)) of SZ. The average precipitate sizes of AA3003 core, AS and RS of SZ were measured as 2.39 $\pm$0.3 μm, 1.34 $\pm$0.3 μm, and 1.52 $\pm$ 0.3 μm, respectively. Compared with the AA3003 core, the average size of precipitates inside the SZ is relatively smaller due to the stirring action of the tool (Gao *et al*., 2022).

Table 4.3 Chemical compositions of particles and possible precipitates in Figure 4.4.

Materials	Location	Composition (at.%)				Possible precipitates
		Al	Fe	Mn	Si	
BM (AA3003 core)	P_1	91.28	2.14	6.68	-	Al_6(Mn,Fe)
	P_2	81.46	7.86	5.45	5.23	Al(Mn,Fe)Si
SZ at AS (S_2)	P_1	92.81	2.51	4.68	-	Al_6(Mn,Fe)
	P_2	80.85	3.56	6.98	8.61	Al(Mn,Fe)Si
SZ at RS (S_3)	P_1	89.34	6.63	4.03	-	Al_6(Mn,Fe)
	P_2	82.34	5.26	6.23	6.17	Al(Mn,Fe)Si
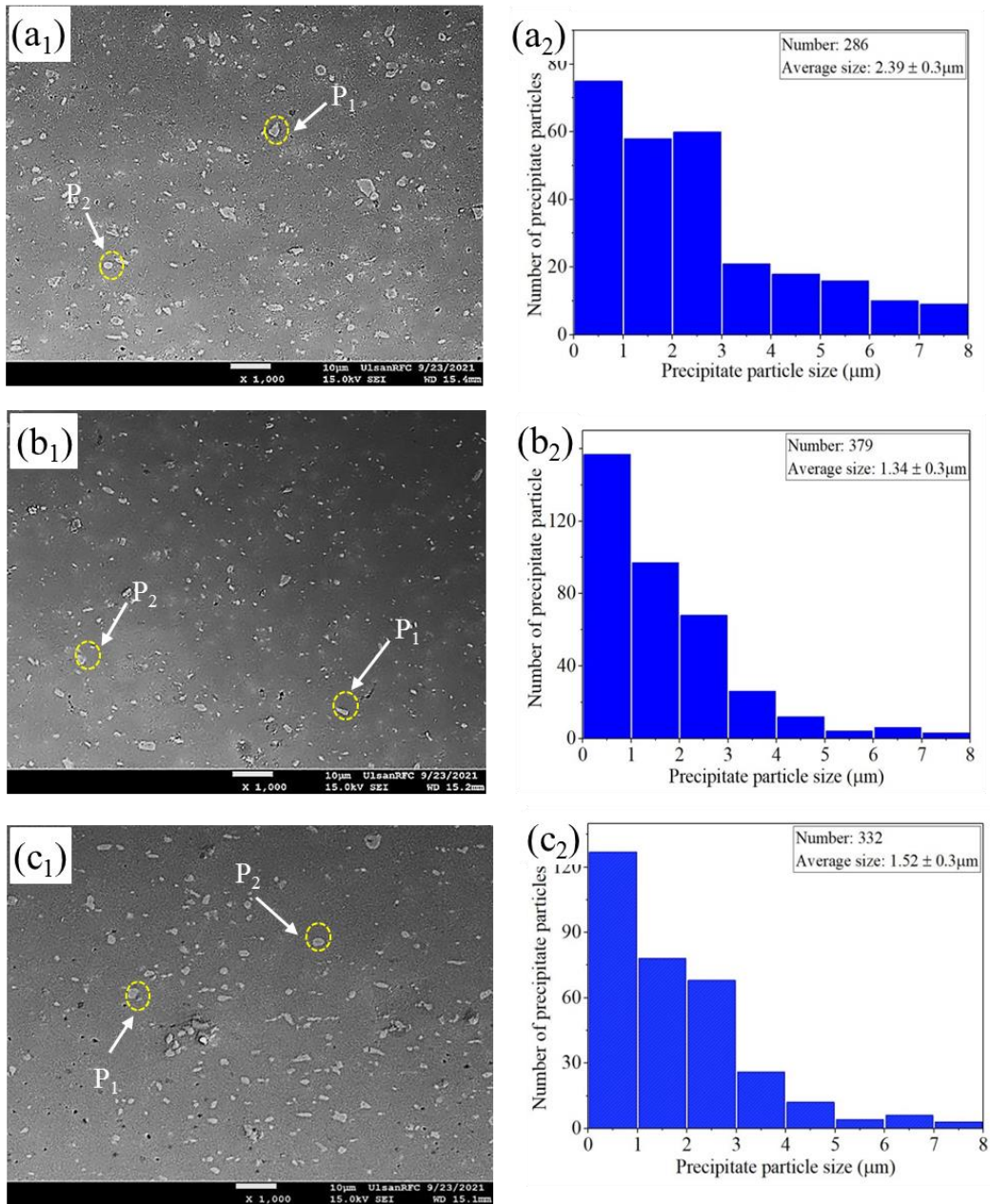
Figure 4.4 SEM images and histograms of size distributions of precipitates: (a_{1-2}) AA3003

clad layer of BM, (b_{1-2}) SZ on the AS (S_2), (c_{1-2}) SZ on the RS (S_3).

The SEM images and their corresponding EDS line scans of AS (L_1), RS (L_2), and

middle (L_3) of the SZ near AA1050-clad mild steel (as marked in Figure 4.2(d)) are shown in

Figure 4.5. The SEM images (Figures 4.5(a_1, b_1, c_1, and d_1)) show that no significant defect

was observed at the interface of Al and steel on all the positions. The EDS line scan results of

BM (Figure 4.5(a_2)) and SZ (Figures 4.5(b_2, c_2, and d_2)) confirmed the presence of atomic diffusion across the interface of Al and steel, indicating the formation of Al/Fe IMCs (Gao *et al.*, 2021). Based on the elemental distribution (Al and Fe) of the EDS line scan across the interface, the thickness of the IMC layers in the BM and SZ was approximately determined. The thickness of the IMCs layer in the SZ (especially at the middle of the SZ, approximately 1.44 μm) is significantly larger than that in the BM AA1050-clad mild steel (approximately 0.66 μm) as a combined result of the compressive load and the heat input caused by the rotating tool.

Based on the Al-Fe phase diagram (Sina *et al.*, 2015) and analysis of the EDS elemental compositions (Table 4.4), the possible IMCs at four different positions (AA1050-clad mild steel (BM), L_1, L_2, and L_3) can be determined. As summarized in Table 4.4, the Al-rich IMCs, including $FeAl_3$ and Fe_2Al_5, were identified at the Al/steel interface of BM (AA1050-clad mild steel). In contrast, the Al/steel interface in the SZ (L_1, L_2, and L_3) comprises of the Al-rich IMCs ($FeAl_3$, Fe_2Al_5) and Fe-rich IMCs (FeAl). Due to the elemental diffusion induced by the heat input and compressive load during the FSLW, a part of Al-rich IMCs were transformed into Fe-rich IMCs (Gao *et al.*, 2021).

Table 4.4 Chemical compositions of IMC and possible phases in Figure 4.5.

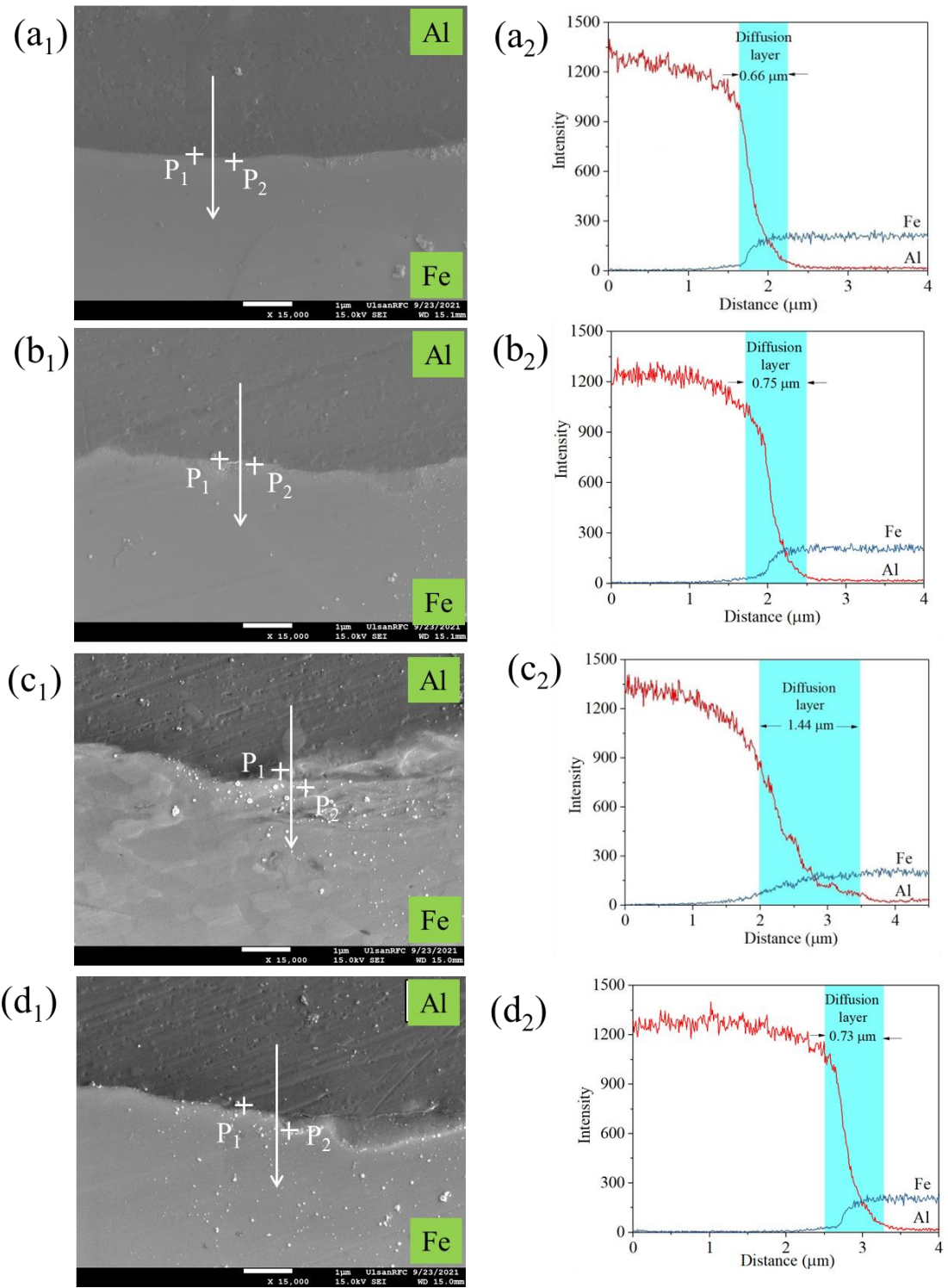| Location		Composition (at.%)		Possible phases	IMC layer (µm)
		Al	Fe		
BM	P_1	73.85	26.15	$FeAl_3$	0.65 ($\pm$0.1)
	P_2	67.65	32.35	Fe_2Al_5	
SZ at AS	P_1	72.13	27.87	$FeAl_3$	0.75 ($\pm$0.12)
(L_1)	P_2	49.18	50.82	$FeAl$	
SZ in the	P_1	66.68	33.32	Fe_2Al_5	1.45 ($\pm$0.21)
middle (L_2)	P_2	49.75	50.25	$FeAl$	
SZ at RS	P_1	72.90	27.10	$FeAl_3$	0.73 ($\pm$0.10)
(L_3)	P_2	46.57	53.43	$FeAl$	

Figure 4.5 SEM images and EDS line scans of interface of Al/Fe: (a$_{1-2}$) BM (AA1050-clad mild steel), (b$_{1-2}$) SZ at AS (L$_1$), (c$_{1-2}$) SZ in the middle (L$_2$), (d$_{1-2}$) SZ at RS (L$_3$).

4.3.3 EBSD analysis

The IPF maps of BMs, junction of TMAZ/SZ (S_1), and AS (S_2) and RS (S_3) of the SZ are illustrated in Fig. 6. The average grain sizes of AA3003, AA4343, and AA1050 were measured to be 41.7 ± 2.7 μm, 14.8 ± 1.5 μm, and 51.2 ± 4.6 μm respectively. The AA4343 has a refined grains structure compared to AA3003 and AA1050 with coarse grains. The IPF map of TMAZ (Figure 6(c)) shows a mix of directional, elongated, and equiaxed grains with an average grain size of 12.9 ± 1.2 μm. In contrast, the SZ with an average size of 4.8 ± 0.39 μm (Figures 6(d-e)) demonstrates homogeneous equiaxed grains due to the dynamic recrystallization during FSLW (Hu *et al*., 2018).
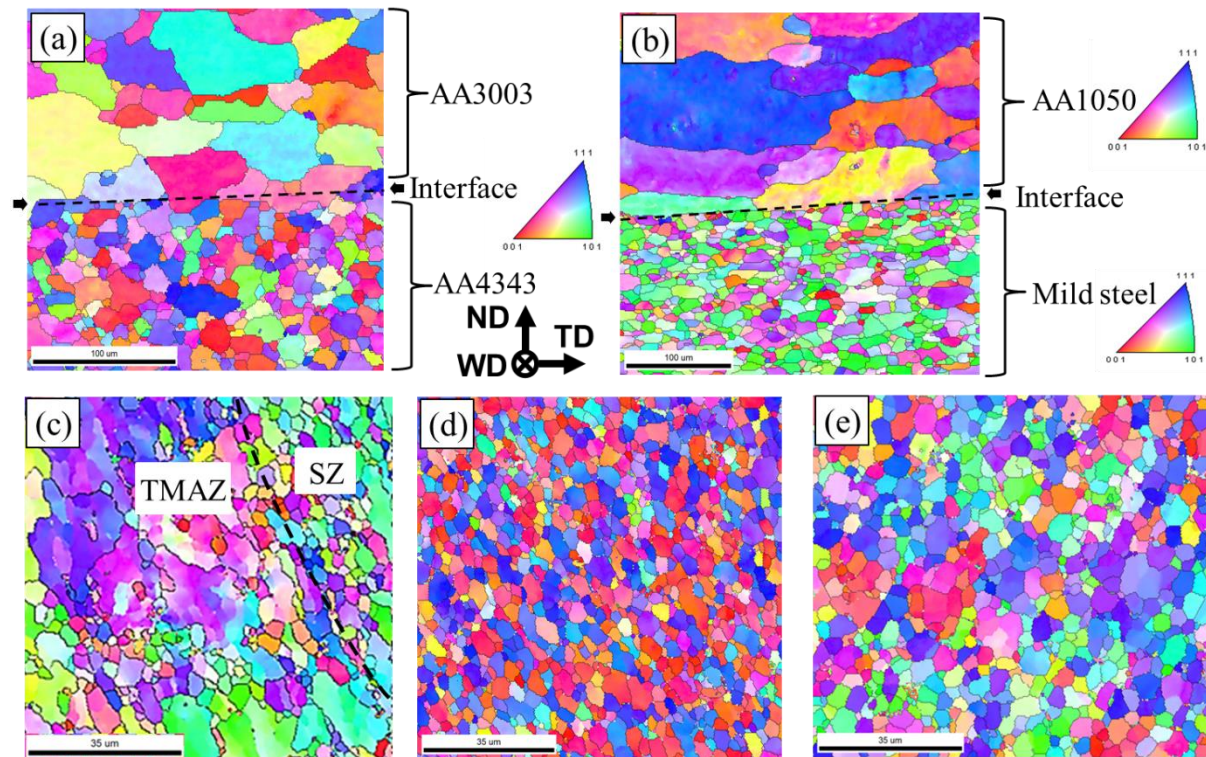

Figure 4.6 IPF maps for (a) BM (AA4343-clad AA3003), (b) BM (AA1050-clad mild steel), (c) junction of AS of SZ and TMAZ (S_1), (d) SZ-RS (S_2), (e) SZ-AS (S_3).

Microstructural appearances of the junction of TMAZ/SZ (S_1), and AS (S_2) and RS (S_3) of the SZ were examined, as shown in Figure 4.7. The intergranular grain

misorientations could represent the local strain concentration resulting from the materials flow during FSLW. The KAM value at the AS (S_2: 0.68) is similar to that at the TMAZ/SZ junction (S_1), but higher than that at the RS (S_3: 0.53), as shown in Figures 4.7(a_1, b_1, and c_1). The higher KAM values at the AS of SZ and junction of TMAZ/SZ can be attributed to the severe material flow and the inconsistent deformation of materials.

The GBCD maps of the AS (Figure 7(b_2)) and RS (Figure 4.7(c_2) of SZ represent the dominance of the HAGBs over the LAGBs. However, the region in the junction of TMAZ/SZ has higher LAGBs (S_1: 52.6%), as shown in Figure 4.7(a_2). Based on the misorientation-angle distributions (Figures 4.7(a_3, b_3, and c_3)), the weighted-average grain boundary misorientation angles for S_1, S_2, and S_3 were calculated as 22.45°, 32.94°, and 30.68°, respectively. Partial recrystallization is primarily responsible for the smaller intergranular grain misorientation angle in the junction of TMAZ/SZ.
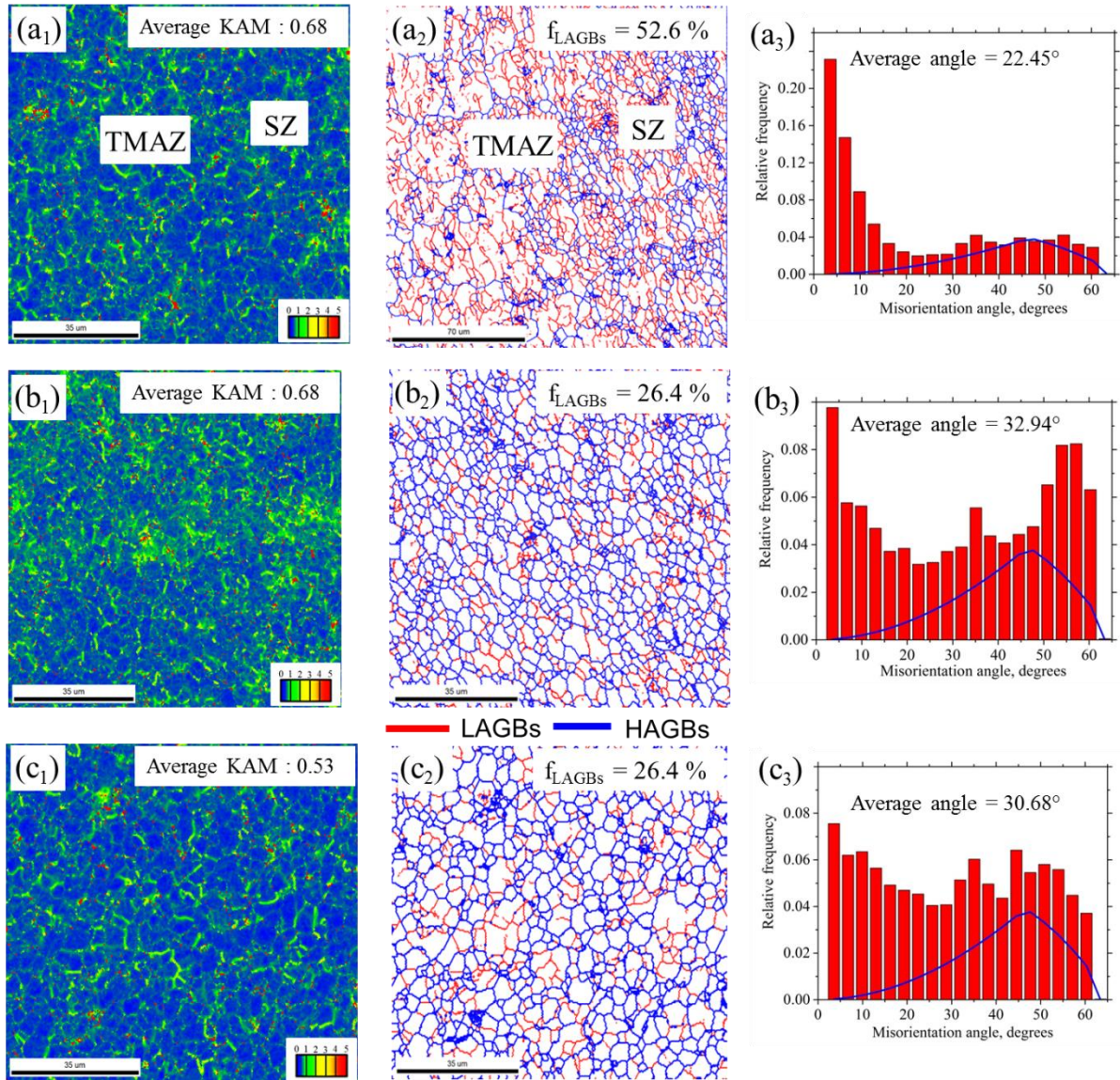
Figure 4.7 KAM maps, GBCD maps, and boundary misorientation angle distribution for (a_{1-3}) junction of AS of SZ and TMAZ (S_1), (b_{1-3}) SZ-RS (S_2), (c_{1-3}) SZ-AS (S_3).

The IPF map of the mild steel BM exhibits typical coarse ferrite grains with an average grain size of 12.6 ± 0.9 μm. Compared with the grain structure of the mild steel BM, more refined grains were observed in the case of the TMAZ and SZ of deformed mild steel in the FSLW joint. As shown in the IFP maps for the regions marked in Figure 4.2(d), the average grain sizes of TMAZ and SZ in the region of deformed mild steel (Figures 4.8(b) and (c)) were measured to be 0.88 ± 0.04 μm and 0.79 ± 0.03 μm, respectively. The refined

equiaxed grains in the TMAZ and SZ of deformed mild steel were generated by recrystallization during FSLW (Li *et al*., 2019).
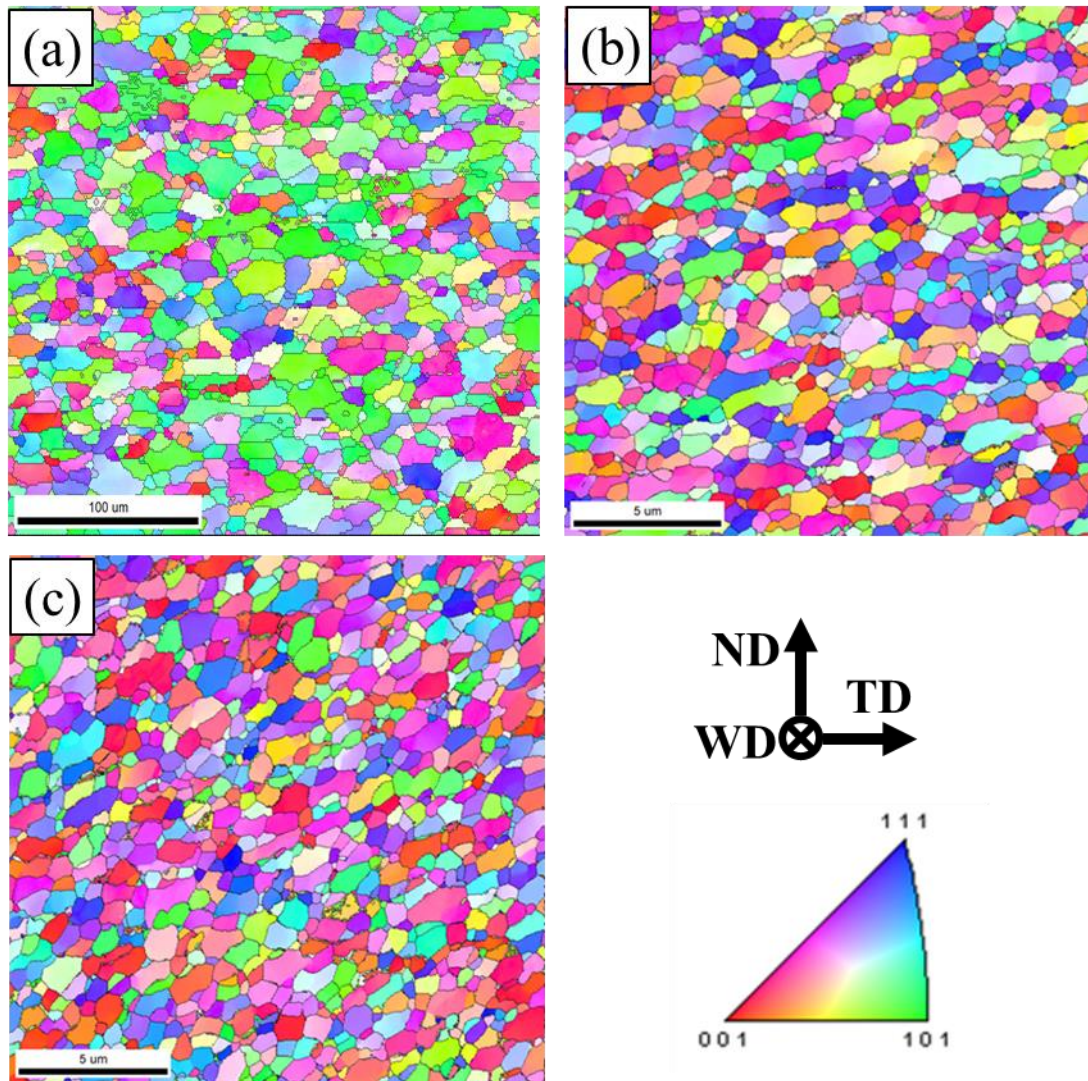
Figure 4.8 IPF maps for (a) mild steel, (b) TMAZ and (c) SZ of the deformed mild steel.

4.3.4 Hardness analysis and tensile test

The 2D surface microhardness contour on the FSLWed cross section (excluding steel) is shown in Figure 4.9. The hardness mapping shows an asymmetric distribution with respect to the centerline of the SZ. The asymmetric distribution of the surface microhardness is primarily attributed to the inhomogeneous material mixing between the AS and RS. The RS

of SZ (red region in Figure 4.9(a)) has the maximum hardness (42.4 HV) due to the presence of stirred AA4343-clad layer with a large amount of Si particles (Figures 4.2(d) and 4.3(c$_2$)). The microhardness inside the SZ (41.1 ± 1.9 HV) is significantly higher than that of the AA3003 core (38.5 ± 1.6 HV) as a combined result of the grain refinement (IPF maps in Figures 4.6(d-e)) caused by dynamic recrystallization and distribution of refined strengthening precipitations resulting from the stirring action of the rotating tool (Figures 4.4(a$_{1-2}$ and b$_{1-2}$)) (Kalaiselvan *et al*., 2014). This is in accordance with the hardness distribution (Figure 4.9(b)) plotted throughout the mid-thickness of the FSLW cross section (excluding mild steel). The hardness distribution through the mild steel core is given in Figure 4.9(c). The surface microhardness of the TMAZ (211 ± 2.6 HV) and SZ (244 ± 8.6 HV) of deformed mild steel were enormously improved compared with the mild steel core BM (152 ± 2.3 HV). The hardness improvement attributed to the grain refinement (IPF maps; Figure 4.9(b-c)) due to the dynamic recrystallization (Li *et al*., 2019).
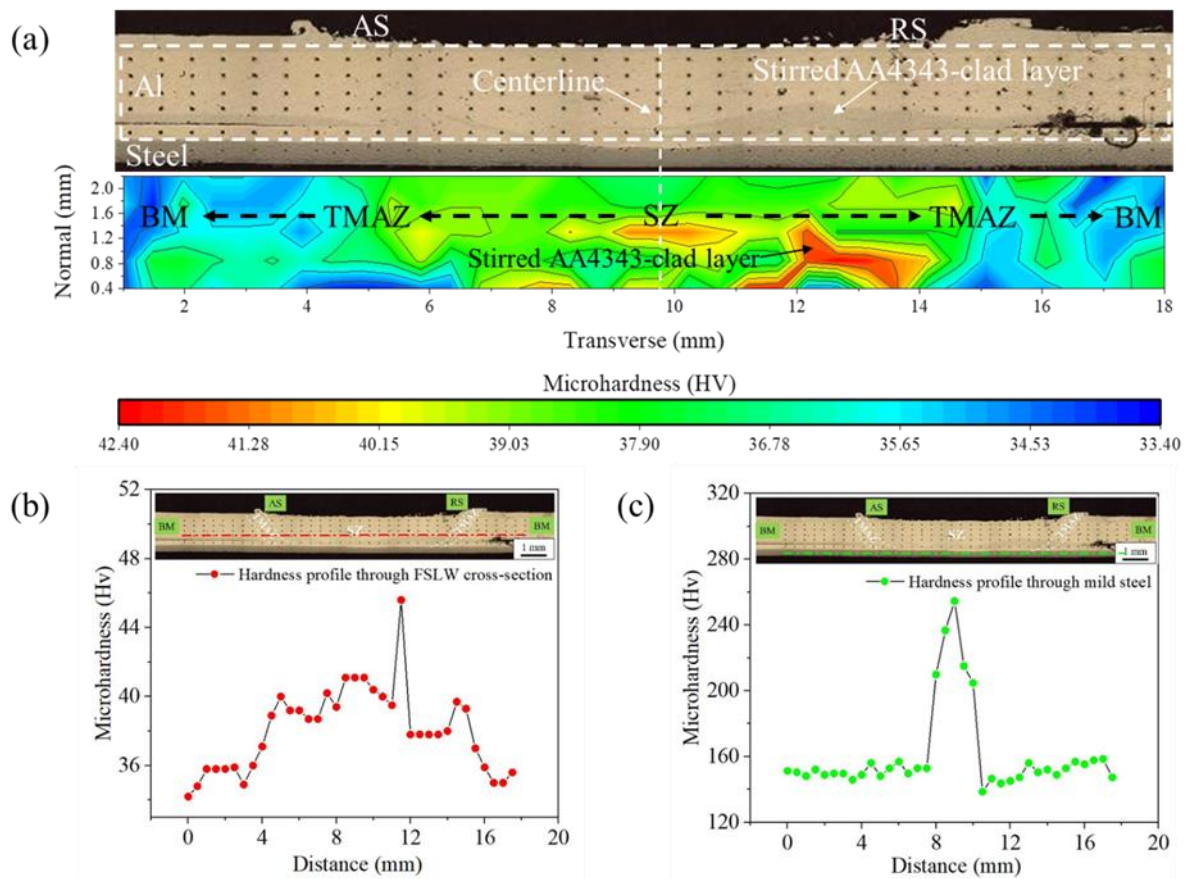
Figure 4.9 Hardness distribution of the joint: (a) hardness contour of Al, (b) hardness profile through the center of Al, (c) hardness profile through the mild steel.

The engineering stress-strain curves from tensile tests of the BMs (AA4343-clad AA3003, AA1050-clad mild steel) are shown in Figure 4.10(a) and the obtained mechanical properties are summarized in Table 4.5. Naturally, the ultimate tensile strength and yield stress of the AA1050-clad mild steel are significantly higher than those of AA4343-clad AA3003. It is also seen that the elongation (12.2 ± 1.1%) of AA1050-clad mild steel is considerably lower than that of AA4343-clad AA3003 (32.6 ± 2.0%). Typical ductile fracture (Figure 4.10(b)) occurred on the AA4343-clad AA3003 BM sheet side for both AS-loaded and RS-loaded lap joints, even though the lap joint has an obvious asymmetric nature in the microstructure. The BM fracture in tensile tests generally confirms that the FSLW joining was successfully conducted.

Table 4.5 Mechanical properties of AA4343-clad AA3003 and AA1050-clad mild steel.

Material	Yield stress (MPa)	UTS (MPa)	Elongation (%)
AA4343-clad AA3003	60.2 ± 1.4	119.4 ± 3.1	32.6 ± 2.0
AA1050-clad mild steel	241.6 ± 4.6	268.9 ± 8.8	12.2 ± 1.1

Figure 4.10 (a) Engineering stress-strain curves of BMs, (b) fractured AS-loaded joint and RS-loaded joint after tensile shear test.

4.3.6 Fatigue analysis

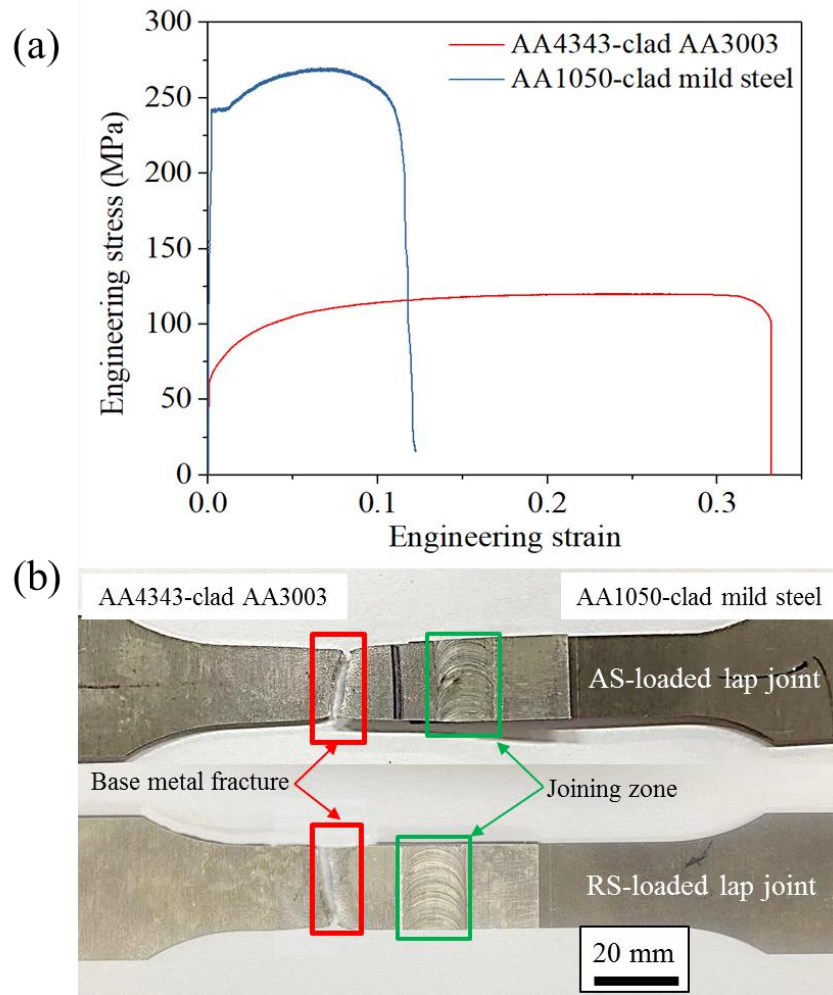As shown in the S-N curves of AS-loaded lap joints and RS-loaded lap joints (Figure 4.11), the fatigue data of the AS-loaded lap joint is located behind that of the RS-loaded lap

joint. This result indicates that the RS-loaded lap joint demonstrates a higher fatigue performance than the AS-loaded lap joint. With decreasing the applied fatigue stress of the FSLW joint from 70 MPa to 30 MPa, a significantly different increase in the fatigue life between the AS-loaded lap joint and the RS-loaded lap joint was observed. The fatigue life of the RS-loaded lap joint was $(1.14 \pm 0.15) \times 10^6$ cycles under the fatigue stress of 30 MPa, which can meet the design requirements of the battery case.
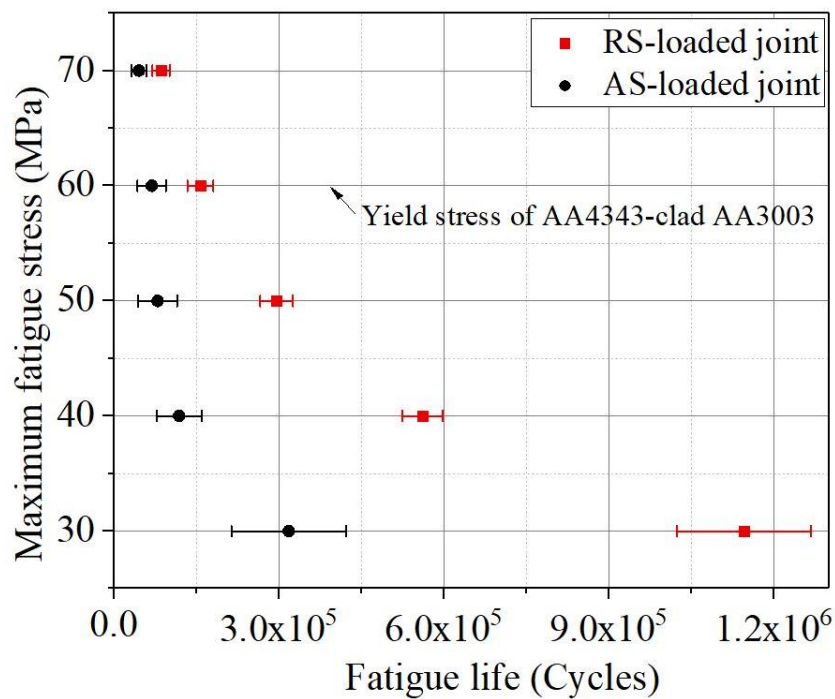
Figure 4.11 S-N results of AS-loaded joint and RS-loaded joint.

The cross sections of typical fatigue fractured AS-loaded lap joint (applied fatigue stress: 50 MPa) and the RS-loaded lap joint (applied fatigue stress: 50 MPa) are shown in Figures 4.12 and 4.13, respectively. All fatigue cracks were initiated from the tips of non-bonding regions (Figures 4.2(b-c)) due to the presence of a significant stress concentration (Costa et al., 2017). As a result of the asymmetric geometry of the FSLW joint and different loading configurations, two different crack propagation modes occurred in fatigue tests, as

shown in Figures. 4.12 and 4.13. At the AA4343-clad AA3003 loading side, the fatigue cracks propagated upward roughly in the direction perpendicular to the applied fatigue load. At the AA1050-clad mild steel loading side, the fatigue crack propagated upward approximately along the direction of the applied fatigue load.

When the AA4343-clad AA3003 loading side corresponds to the AS of SZ (i.e., the AS-loaded joint, Figure 4.12), the vertical crack leaded to the final fatigue fracture of the joint, which occurred in the junction of TMAZ/SZ (S_1). However, when the AA4343-clad AA3003 loading side corresponds to the RS of SZ (i.e., the RS-loaded joint, Figure 4.13), the vertical crack propagated upward in SZ (S_3), but did not cause the final fracture of the joint.

Based on the S-N results (Figure 4.11), the fatigue life of RS-loaded joint is significantly longer than that of AS-loaded joint, which indicates that vertical crack propagation has been retarded in the RS-loaded joint. The vertical fatigue crack in the AS-loaded joint has a higher propagation rate than that in RS-loaded joint due to the asymmetrical microstructural characteristics of joint. As discussed in Figure 4.7, much higher KAM value (Figure 4.7(a_1)) were observed in the KAM maps of the junction of TMAZ and SZ (AS) compared with the SZ-AS (Figure 4.7(c_1)), which suggested that the possible presence of the strain concentration leads to the degradation of fatigue performance. Previous research suggested that the grain boundary with a higher intergranular grain misorientation angle is a significant barrier that restrains fatigue crack propagation (Zhou *et al*., 2016; Liu *et al*., 2018; Ma *et al*., 2020; Zhai *et al*., 2005). The junction of TMAZ/AS of SZ (Figure 4.7(a_{2-3})) has a smaller intergranular grain misorientation angle than RS of SZ (Figure 4.7(c_{2-3})), accelerating fatigue crack propagation rate. Besides, the RS of SZ with the higher hardness (Figure 4.9(a)) inhibited the upward propagation of cracks.

When the AA1050-clad mild steel loading side corresponds to the RS of SZ (i.e., the AS-loaded joint, Figure 4.12) and the AS of SZ (i.e., the RS-loaded joint, Figure 4.13), it can

be seen that the fatigue cracks deflected downward and penetrated the AA1050-clad layer, since the mild steel has higher resistance to fatigue crack growth than AA1050 clad layer. However, note that when the AA1050-clad mild steel loading side corresponds to the RS of SZ (i.e., the AS-loaded joint, Figure 4.12), fatigue crack propagated along the junction of the mild steel and the TMAZ (deformed mild steel). The sharpest hardness gradient (Figure 4.9(b)) in the junction of mild steel (BM) and TMAZ of deformed mild steel is a leading reason for the fatigue failure at this position (Sorger *et al.*, 2018).
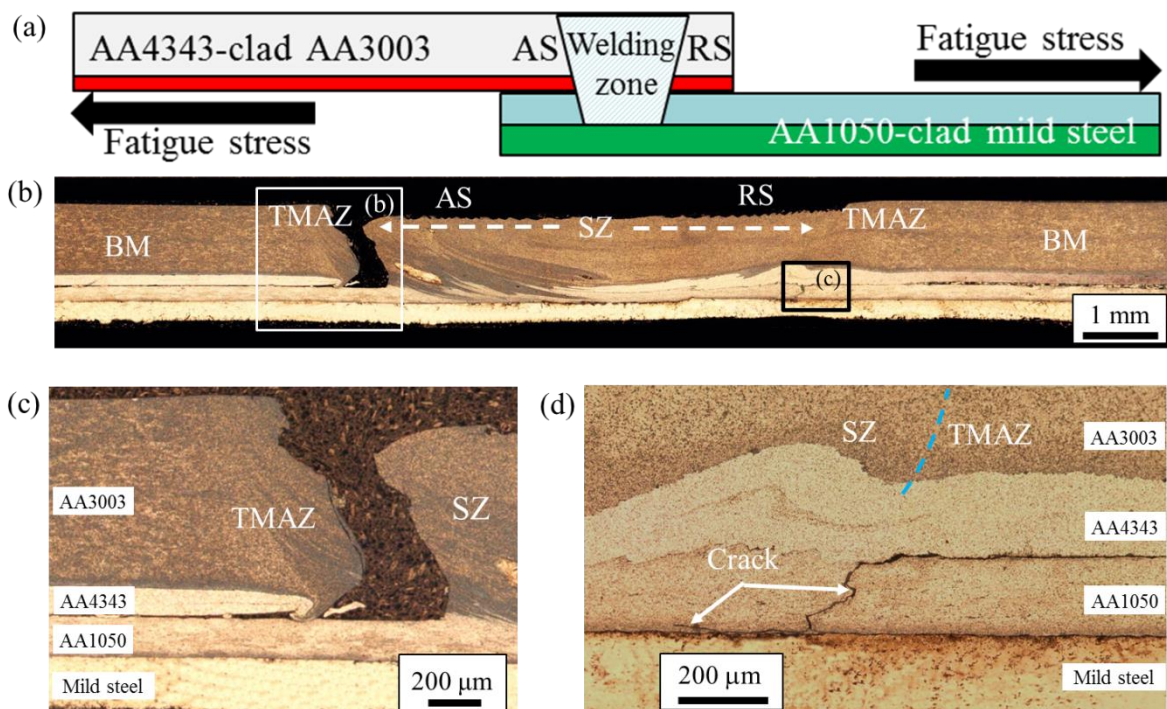
Figure 4.12 (a) Schematic of loading mode, (b) cross section of the fatigue fractured of AS-loaded joint (50 MPa), (c) fatigue fractured crack in the junction of TMAZ and SZ (AS), (d) fatigue crack on the RS.
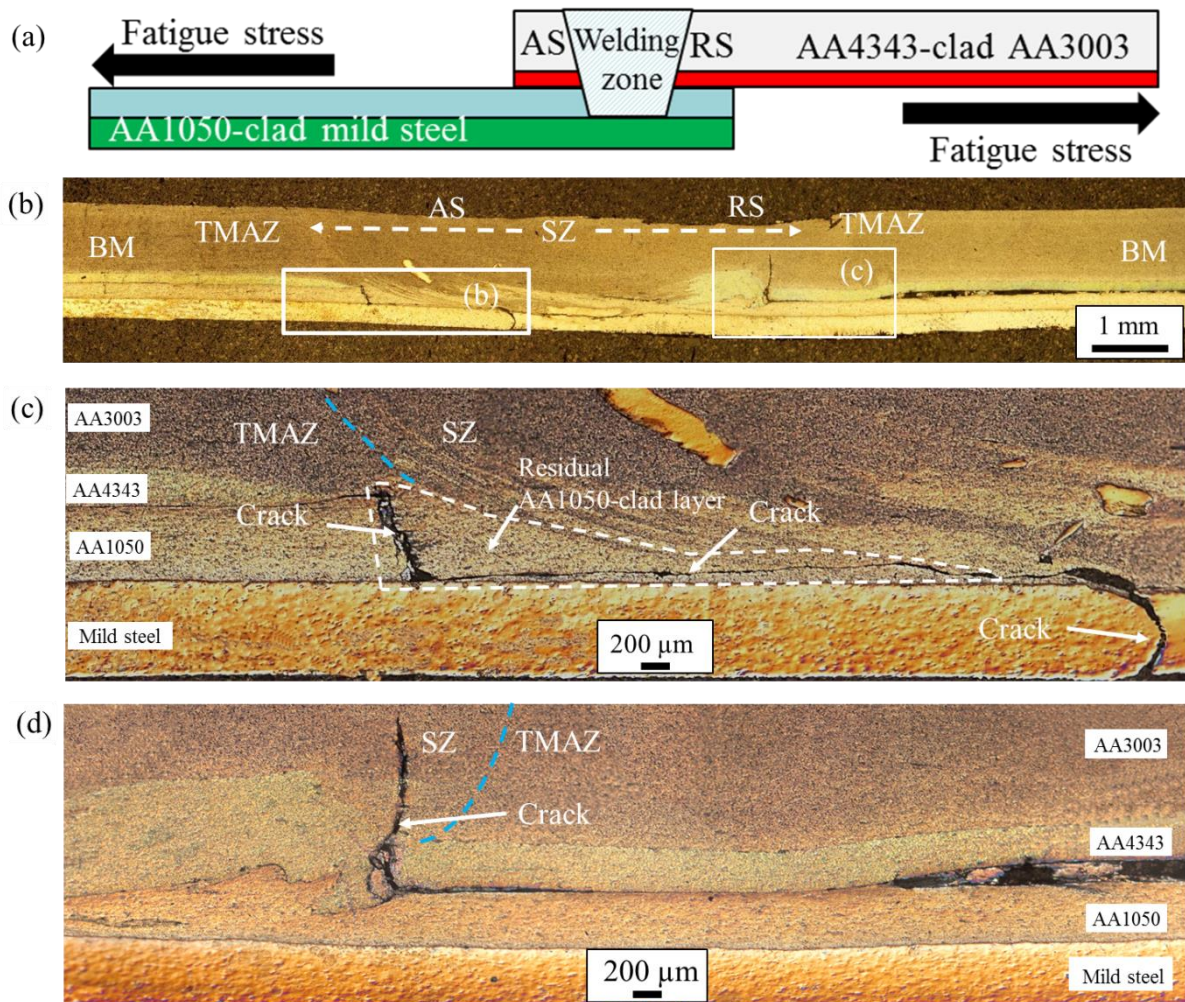
Figure 13 (a) Schematic of loading mode, (b) cross section of the fatigue fractured of RS-loaded joint (50 MPa), (c) fatigue fractured crack on the AS, (d) fatigue crack on the RS.

SEM micrographs of the fatigue fracture surface of the AS-loaded lap joint (fatigue stress: 50 MPa) and the RS-loaded lap joint (fatigue stress: 70 MPa) are represented in Figure 4.14. The fracture surfaces of both lap joints are smooth with a large number of fatigue striations in the fatigue crack propagation zones, as shown in Figures 14(a_1 and b_1). The final fracture area (Figures 4.14(a_2 and b_2)) presents a ductile dimpled with various sizes.
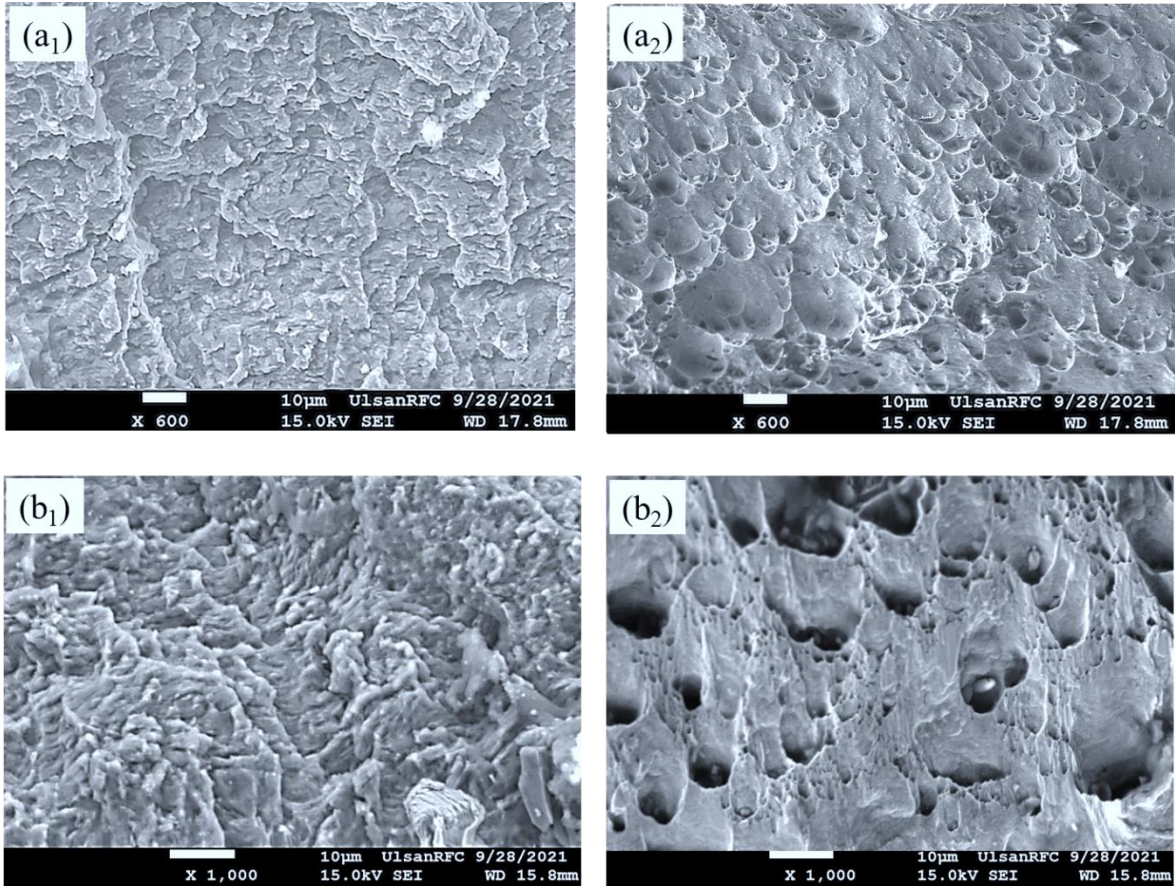
Figure 4.14 Fatigue crack propagation zone and fast fracture zone for (a_{1-2}) AS-loaded joint

and (b_{1-2}) RS-loaded joint.

4.4 Conclusion

In this present study, the FSLW of Al-clad Al and Al-clad mild steel was executed successfully. The complicated joining zone morphology and microstructure caused by material mixing at the lap interface have a vital influence on mechanical properties. The cross section of the FSLW joint shows that material mixing is asymmetric concerning the centerline of the SZ. After FSLW, the AA1050-clad layer was still survived on the surface of the mild steel core. As a combined result of the tool compression and heat input, the thickness of the IMC layer was increased, and the Fe-rich IMCs were found at the interface of Al and steel in the SZ. The SZ of the FSLW joint was characterized by grain refinement caused by dynamic recrystallization and high-density precipitations. As a result, the AS-loaded FSLW joint has poorer fatigue performance than the RS-loaded FSLW joint. The fatigue cracks of the AS-loaded joint were initiated from the tips of non-bonding regions due to the presence of higher stress concentration. Then, the fatigue fracture of the AS-loaded joint occurred in the junction of TMAZ and AS of SZ. The microstructure analysis on the fatigue fractured position reveals that the significant difference in grain size and grain orientation between TMAZ and AS of SZ are responsible for the poor fatigue performance of the AS-loaded joint. Besides, the higher strain concentration and lower intergranular grain misorientation angles in the junction of TMAZ and AS of SZ cause the degradation of fatigue properties.

References

Hannan MA, Azidin FA, Mohamed A (2014) Hybrid electric vehicles and their challenges: a review. Renewable and Sustainable Energy Reviews. 29:135-150.

Yilmaz M, Krein PT (2013) Review of battery charger topologies, charging power levels, and infrastructure for plug-in electric and hybrid vehicles. IEEE transactions on Power Electronics. 28(5):2151-2169.

Rhee KY, Han WY, Park HJ, Kim SS (2004) Fabrication of aluminum/copper clad composite using hot hydrostatic extrusion process and its material characteristics. Materials Science and Engineering: A. 384(1-2):70-76.

Park HJ, Na KH, Cho NS, Lee YS, Kim SW (1997) A study of the hydrostatic extrusion of copper-clad aluminium tube. Journal of Materials Processing Technology. 67(1-3):24-28.

Ban H, Bai R, Chung K-F, Bai Y (2020) Post-fire material properties of stainless-clad bimetallic steel. Fire Safety Journal. 112:102964.

Su H, Luo XB, Chai F, Shen JC, Lu F (2015) Manufacturing technology and application trends of titanium clad steel plate. Journal of Iron and Steel Research International, 22(11):977-982.

Chen LC, Yang ZG, Jha B, Xia GG, Stevenson JW (2005) Clad metals, roll bonding and their applications for SOFC interconnects. Journal of Power Sources. 152:40-45.

Okui T, Yoshida K, Yonemitsu Y (2014) Development of Metal Clad Sheets and Strips. Nippon Steel and Sumitomo Metal Technical Report. 106:103-107.

Fallu J, Izadi H, Gerlich AP (2014) Friction stir welding of co-cast aluminium clad sheet, Science and Technology of Welding and Joining. 19(1):9-14.

Ericsson M, Jin LZ, SandstrÖm R (2007) Fatigue properties of friction stir overlap welds International journal of fatigue. 29(1):57-68.

Raturi M, Bhattacharya A (2021) Microstructure and texture correlation of secondary heating assisted dissimilar friction stir welds of aluminum alloys. Materials Science and Engineering: A. 825:141891.

Oikawa H, Saito T, Yoshimura T, Nagase T, Kiriyama T (1996) Spot welding of aluminium clad steel to steel or aluminium: Joining steel to aluminium with an intermediate layer (1st Report). Welding International. 10(7).

Rahimi S, Movahedi M (2020) Resistance Spot Welding of Aluminum to Aluminum Clad Steel Sheet: Experimental and Theoretical Analysis. Journal of Manufacturing Processes. 58:429-435.

Thomas WM, Nicholas ED, Needham JC, Murch MG, Temple-Smith P, Dawes CJ (1991) GB Patent application no.9125978.8[J]. International patent application no. PCT/GB92/02203.

Movahedi M, Kokabi AH, Seyed Reihani SM (2012) Investigation on friction stir lap welding of aluminum to aluminum clad steel sheets. Science and Technology of Welding and Joining. 17(3):231-236.

Li G, Zhou L, Luo L, Wu X, Guo N (2019) Microstructural evolution and mechanical properties of refill friction stir spot welded alclad 2A12-T4 aluminum alloy. Journal of Materials Research and Technology. 8(5):4115-4129.

Liu H, Zhao Y, Hu Y, et al. (2015) Microstructural characteristics and mechanical properties of friction stir lap welding joint of Alclad 7B04-T74 aluminum alloy. The International Journal of Advanced Manufacturing Technology. 78(9):1415-1425.

Kumar K, Kailas SV (2008) The Role of Friction Stir Welding Tool on Material Flow and Weld Formation. Materials Science and Engineering: A. 485(1-2):367-374.

Cederqvist L, Reynolds AP (2001) Factors affected the properties of friction stir welded aluminum overlap joints. WELDING JOURNAL-NEW YORK-. 80(12):281-s.

Xu X, Yang X, Zhou G, et al. (2012) Microstructures and fatigue properties of friction stir lap welds in aluminum alloy AA6061-T6. Materials & Design. 35:175-183.

Zandsalimi S, Heidarzadeh A, Saeid T (2019) Dissimilar friction-stir welding of 430 stainless steel and 6061 aluminum alloy: Microstructure and mechanical properties of the joints. Proceedings of the Institution of Mechanical Engineers, Part L: Journal of Materials: Design and Applications. 233(9):1791-1801.

Chen ZW, Yazdanian S (2012) Friction Stir Lap Welding: material flow, joint structure and strength. Journal of Achievements in Materials and Manufacturing Engineering. 55(2):629-637.

Basak S, Mondal M, Gao K, et al. (2022) Friction stir butt-welding of roll cladded aluminum thin sheets: Effect of microstructural and texture changes on mechanical properties. Materials Science and Engineering: A. 832:142490.

Gao K, Basak S, Mondal M, Zhang S, Hong S-T, Boakye S-Y, Cho H-H (2022) Friction stir welding of AA3003-clad AA6013 thin sheets: Microstructural changes related to tensile properties and fatigue failure mechanism, Journal of Materials Research and Technology, 17: 3221-3233.

Gao K, Zhang S, Mondal M, Basak S, Hong S-T, Shim H (2021) Friction Stir Spot Butt Welding of Dissimilar S45C Steel and 6061-T6 Aluminum Alloy. Metals. 11:1252.

Sina H, Corneliusson J, Turba K, Iyengar S (2015) A study on the formation of iron aluminide (FeAl) from elemental powders. Journal of Alloys and Compounds. 636:261-269.

Hu YY, Liu HJ, Li S, Du S, Sekulic DP (2018) Improving mechanical properties of a joint through tilt probe penetrating friction stir welding. Materials Science and Engineering: A. 731:107-118.

Li YF, Hong S-T, Choi H, Han H-N (2019) Solid-state dissimilar joining of stainless steel 316L and Inconel 718 alloys by electrically assisted pressure joining. Materials Characterization, 154, 161-168.

Kalaiselvan K, Dinaharan I, Murugan N (2014) Characterization of friction stir welded boroncarbide particulate reinforced AA6061 aluminum alloy stir cast composite, Materials & Design. 55:176–182.

Costa MI, Leitao C, Rodrigues DM (2017) Influence of post-welding heat-treatment on the monotonic and fatigue strength of 6082-T6 friction stir lap welds. Journal of Materials Processing Technology. 250:289–296.

Zhou P, Zhou J, Ye Z, Hong X, Huang H, Xu W (2016) Effect of grain size and misorientation angle on fatigue crack growth of nanocrystalline materials. Materials Science and Engineering: A. 663:1–7.

Liu Z, Guo X, Cui H, Li F, Lu F (2018) Role of misorientation in fatigue crack growth behavior for NG-TIG welded joint of Ni-based alloy. Materials Science and Engineering: A. 710:151–163.

Ma M, Wang B, Liu H, Yi D, Shen F, Zhai T (2020) Investigation of fatigue crack propagation behavior of 5083 aluminum alloy under various stress ratios: Role of grain boundary and Schmid factor. Materials Science and Engineering: A. 773:138871.

Zhai T, Jiang XP, Li JX, Garratt MD, Bray GH (2005) The grain boundary geometry for optimum resistance to growth of short fatigue cracks in high strength Al-alloys. International Journal of Fatigue. 27:1202–1209.

Sorger G, Lehtimäki E, Hurme S, Remes H, Vilaça P, Molter L (2018) Microstructure and fatigue properties of friction stir welded high-strength steel plates. Science and Technology of Welding and Joining. 23(5):380-386.

CHAPTER V

CONCLUSIONS

FSW/FSSW is process of solid state joining two similar or dissimilar metal by the rotating tool in which heat generated by the rotating tool is utilized for welding process. The FSW process takes place in the solid-phase, at temperatures below the melting point of the material, and as a result does not experience problems related to resolidification, such as the formation of second phases, porosity, embrittlement, and cracking. In addition, the lower temperature of the process enables joining with lower distortion and lower residual stresses. FSW is also an energy efficient process that requires no filler material and, in most cases, does not require the use of a shielding gas. Furthermore, the process lacks the fumes, arc flash, spatter, and pollution associated with most fusion welding techniques. For these and many other reasons, this joining technique is energy efficient, environment friendly, and versatile. In particular, it can be employed to join high-strength aerospace aluminum alloys and other metallic alloys that are difficult to weld by conventional fusion welding. The dissertation demonstrates the joining feasibility of SM45C and AA6061-T6 by FSSW, the joining of AA3003-clad AA6013 thin sheets by FSW, and the lap joining of AA4343-clad AA3003 and AA1050-clad mild steel. The major achievements/findings of this dissertation can be summarized as follow:

FSSW of dissimilar SM45C steel and 6061-T6 aluminum alloy were attempted by a convex scrolled tool at different rotational speeds and tool offsetting. Butt spot welds were successfully joined by offsetting tool to steel side. The results of OM and SEM analysis confirmed that a sound solid-state joint was successfully fabricated without significant

defects. The presence of intermetallic compounds (IMCs) in the interface between SM45C steel and 6061-T6 aluminum alloy is identified. In addition, the thickness of the IMC layer increases with increasing the rotational speed. The IMCs with a certain thickness can improve the mechanical property of welded joints by tensile test.

The FSW of AA3003-claded AA6013 was carried out at the tool rotating speed of 800 rpm and the welding speed of 200 mm/min. The microstructural analysis showed that the AA3003 clad layer was stirred into the AA6013 core layer by the rotating tool. The zigzag line and a small amount of AA3003 fragments were observed at PIZ and SIZ-AS respectively. Combined with the BM, the SZ exhibited fine equiaxed grains due to the grain recrystallization and uniformly distributed precipitate refinement due to the stirring action of the FSW tool. The results of the tensile test showed that the FSW cross-weld joint fractured in the BM. Base on the Hall-Petch equation, grain and precipitate refinement in the SZ can enhance the yield stress of all-weld joints. The analysis of the fatigue failure mechanism suggested that the reason of fatigue failure was attributed to AA3003 clad layer particles of the subsurface of SIZ-AS. After the fatigue test, some cracks were found on the top surface of SIZ-AS (higher surface roughness) due to the stress concentration; by contrast, no defect was observed around the zigzag line. Therefore, the surface roughness and the zigzag line did not play a significant role in the final fatigue fracture.

The FSLW of Al-clad Al and Al-clad mild steel was executed successfully. The complicated joining zone morphology and microstructure caused by material mixing at the lap interface have a vital influence on mechanical properties. The cross section of the FSLW joint shows that material mixing is asymmetric concerning the centerline of the SZ. After FSLW, the AA1050-clad layer was still survived on the surface of the mild steel core. As a combined result of the tool compression and heat input, the thickness of the IMC layer was increased, and the Fe-rich IMCs were found at the interface of Al and steel in the SZ. The SZ

of the FSLW joint was characterized by grain refinement caused by dynamic recrystallization and high-density precipitations. As a result, the AS-loaded FSLW joint has poorer fatigue performance than the RS-loaded FSLW joint. The fatigue cracks of the AS-loaded joint were initiated from the tips of weakly-bonded regions due to the presence of higher stress concentration. Then, the fatigue fracture of the AS-loaded joint occurred in the junction of TMAZ and AS of SZ. The microstructure analysis on the fatigue fractured position reveals that the significant difference in grain size and grain orientation between TMAZ and AS of SZ are responsible for the poor fatigue performance of the AS-loaded joint. Besides, the higher strain concentration and lower intergranular grain misorientation angles in the junction of TMAZ and AS of SZ cause the degradation of fatigue properties.